Ph.D. thesis in Fluid Mechanics and Applied Mathematics

Analytical and numerical vortex methods to model separated flows

Federico Gallizio

Tutor
prof. Luca Zannetti
Politecnico di Torino

Cotutela
prof. Angelo Iollo
Université de Bordeaux 1 - INRIA

Contents

Acknowledgements

After four years of Ph.D. experience, I would like to take this opportunity to thank the many people who supported me. Among the others, special go thanks to

Luca Zannetti and Angelo Iollo, my tutors in Turin and in Bordeaux, for the suggestions, the wide discussions and the attention devoted to this work

Haysam Telib, my persevering colleague in Turin, for the discussions

and

Giulio Avanzini, Marcelo Buffoni, Simone Camarri, Georges-Henri Cottet, Bernardo Galletti, Irene Gned, Ester Nkatha Gorfer, Edoardo Lombardi, Adrien Magni, Edmondo Minisci, Iraj Mortazavi, Gabriele Maria Ottino, Bartek Protas, Mario Ricchiuto.

This work was funded and sponsored by a Progetto Lagrange Fondazione CRT grant, INRIA Bordeaux sud-ouest team MC2, the VortexCell2050 project within the FP6 Programme of the European Commission and COMMA project led by Université Joseph Fourier - Grenoble.

Summary

The problem of the separated flows dynamics past obstacles at rest or moving bodies is addressed by means of the study of two topics

- investigation on the existence of some steady solutions of the Euler equations and of the Navier-Stokes equations at large Reynolds number, past bodies characterized by a cusp;
- analysis of the unsteady wake behind a Vertical Axis Turbine (VAT).

The survey of such different flow regimes related to the separation phenomenon past bluff bodies or bodies at incidence allowed to devise several numerical and analytical techniques based on the evaluation of the vorticity field.

This work is divided into two parts, corresponding to the study of a steady and an unsteady problem. In the first chapter the 2D incompressible steady flow past a certain class of obstacles is taken into consideration. These obstacles consist in symmetrical or unsymmetrical bodies which protrude from a wall and present a sharp edge, where the non-singularity condition of the velocity (Kutta condition) is enforced. A flat plate and a curved plate are the geometries taken into account for the study of the flow field bounded in a channel, while a class of 'snow cornices' is considered for the unbounded stream problem. The existence of a steady vortex wake past past such bodies is analytically investigated by means of the potential flow theory where the vorticity is modelled as point singularities. If a geometry admits a point vortex solution in equilibrium and satisfies the Kutta condition, then this solution is desingularized through some various numerical procedures converging on the grid. The suggestion that the point vortex is interesting as it is the seed of a family of distributed vortex patches is widely discussed and examined by means of a continuation method.

In the second chapter, the unsteady flow field generated around a VAT is addressed through both an inviscid and a viscous analysis. The inviscid analysis is carried out by means of a numerical-analytical procedure based on the conformal mappings and the potential flow theory. Some simulations are performed on a single-blade architecture, where an innovative blade section based on the vortex trapping technology is tested. A theory to study the doubly-connected domain problem is

devised and applied in the case of an impulsively started airfoil equipped with a flap. In addition, a low-order model of the vortex wake is proposed for a two-blade architecture of the turbine. The problem of evaluating the dynamical actions exerted by the fluid on a system of moving bodies is solved by means of the theory of the hydro-dynamical impulse of a vortex. Finally a method to compute the performances of the turbine without knowing the pressure field is devised and analytically verified.

A vortex-in-cell method is developed in order to solve the 2D viscous flow field past the turbine. The bodies' geometry is implicitly defined by means of a distance function, and the no-slip condition on the moving solid boundaries is enforced through a penalization technique. Such numerical method is tested on the classical 2D circular cylinder benchmark for different Reynolds numbers. The forces exerted on the bodies are evaluated by an impulse-based formulation of the Navier-Stokes equation, which needs only the velocity field and its derivatives.

The conformal mappings used in this work and some remarks, examples, mathematical derivations are collected in the appendix.

Chapter 1

Introduction

This work has not the ambition of treating in-depth the physics of the flow separation nor of providing a phenomenology of flow control techniques. The problem of the flow detachment past bluff bodies or surfaces at incidence is here studied with the aim of devising a set of numerical and analytical methods which analyse with accuracy the flow field around certain geometries and evaluate efficiently some integral quantities, such as circulation, forces and moments.

The study and the stabilization of the vortex wakes and flows in a separated regime for aeronautical, automotive, nautical and civil applications represent an ambitious research field in fluid mechanics. Within this scenario, the unsteady or massively separated flows are interesting since they are involved in several phenomena which can provide some beneficial or harmful effects.

The high drag generated when a bluff body is immersed within a stream, for instance a truck or the rear-view mirrors, is due to the unsteadiness of the separated flow which produces a wake characterized by shedding of vortex structures and unbalancing loads. Practically, the unsteady separation dissipates the available energy through the kinetic energy exploited by the wake. The Vortex-Induced-Vibrations (VIV) represents another field of interest for such flows. For instance, the uncontrolled separations from civil buildings, aerodynamic surfaces in stall conditions, offshore constructions, stacks and transmission lines generate vibrations that could form noxious interactions with the structure or noise. For such problems, several passive and active control techniques are devised and widely discussed in the state of the art of applied fluid mechanics, such as blowing/suction devices, trapping cavities, synthetic jets, shape optimization and others.

On the other hand, the unsteadiness could be exploited with the aim of extracting efficiently energy from the wind, even for low intensity streams and for high variability of the operating conditions. In the last years the research concerning the increase of the aerodynamic performances of the horizontal axis wind turbines has

reached its top, whereas the major efforts have been devoted to improve the structural behaviour of the blades as compared the aeroelastic and fatigue loads [74]. On the contrary the design of an efficient blade shape for a vertical axis wind turbine is still an actual challenging task, where the turbine efficiency represents the most sensible factor that makes advantageous the installation, for low wind speed regimes above all.

These subjects show recurring features of the applied research combined with the study of complex phenomena, such as unsteadiness, stability of a solution, nonlinearity and sensitivity to the initial conditions. With the aim of providing some instruments which practically treat such problems, a careful modelling is needed regarding the computational cost and the accuracy of the simulation. The development of techniques which combine numerical schemes on Cartesian grid with analytical solutions based on the classical flow potential theory, can represent a good solution to the problem of the simulation time requirements and the ordinary computational resources.

Although the scenario of practical applications of the incompressible separated flows is diversified, the vortex dynamics represents a common background where such problems could be addressed. In particular the vorticity-based formulation of the incompressible Euler and Navier-Stokes equations is an efficient tool for investigating with accuracy some flow fields characterized by moving solid boundaries, multiply-connected regions and geometrical singularities.

In this sense the present work is aimed to devise and collect a set of techniques that allow to solve some examples of steady and unsteady separated flows.

Chapter 2

Steady vortex patches past bodies

In this section we considered some flow models that can be of interest in the field of separated flows past bluff bodies and passive control strategies. The inviscid and incompressible flow assumption is based on the existence of steady unstable solutions with closed streamlines at large Reynolds numbers (Batchelor (1956) [6], [7]). The 2D Euler equations represent a simplified model that describes a rich variety of phenomena in vortex-dominated flows, including equilibrium of the steady solutions. These peculiarities make the Euler equations a suitable tool for devising flow control techniques (Protas (2008) [54]).

In the 2D inviscid incompressible flows, the vorticity ω is constant on a $\psi = const$ streamline, that is $\omega = \omega(\psi)$. The Euler model for an incompressible steady flow is defined by the non linear Poisson equation

$$\nabla^2 \psi = -\omega(\psi). \tag{2.1}$$

The value of the vorticity on closed streamlines is not defined by far field boundary conditions, so, for finite area wakes, this equation provides multiple solutions to the separated flows past bluff bodies. The multiplicity of solutions is relevant to different distributions of vorticity $\omega(\psi)$ which can be assumed for a region with closed streamlines. In [7] Batchelor demonstrated that the limit solution of the viscous flow for the Reynolds numbers tending to infinity is characterized by $\omega(\psi) = const$ in the recirculating regions, i.e. the finite area wake reduces to a vortex patch. Batchelor showed that the value of vorticity in this region is not arbitrary and can be found by a boundary layer analysis. Moreover, the constant distribution of vorticity in the recirculating region can be justified as the result of a large time diffusion of vorticity from the shear layer until the steady solution.

Vortex patch solutions form a three parameter family, where the parameters are the value of the vorticity ω, the vortex patch area A and the Bernoulli constant jump ΔH along the vortex layer that separates the rotational region and the external flow. The circulation of the vortex is represented by $\gamma = \omega A$.

In the Prandtl-Batchelor flows these three parameters depend each other and can be determined by taking into account of the body's geometry. The area A of the vortex patch corresponds to the whole recirculating region (for instance see Saffman & Tanveer (1984) [64]). When the body presents a sharp corner, if the separation is enforced at the edge (Kutta condition), the circulation γ, i.e. the vorticity ω, is prescribed and the problem reduces its degrees of freedom to one. Finally Chernyshenko (1993) [11] has shown that the cyclic boundary layer is a constraint that removes the last degree of freedom, that is the Bernoulli constant jump ΔH.

Wide literature is pertinent to this topic. Several examples and references can be found in Sadovskii (1971) [61], Deem & Zabusky (1978) [21], Pierrehumbert (1980) [51], Saffman & Szeto (1980) [63] and Saffman & Tanveer (1984) [64].

The present study concerns inviscid solutions that in a broad sense belong to the Batchelor flow model. For the sake of simplicity we reduced the problem to two parameters by neglecting the cyclic boundary layer. The vortex regions are modeled as patches with $\Delta H = 0$. The entire steady flow field past a bluff body is then defined by the coupling of two inviscid regions: a rotational $\omega(\psi) = const$ core and an external potential flow. Let us consider the figure 2.1 where Ω is the flow domain, Ω_v is a rotational region and ψ_s is the value of the streamfunction on the boundary of the vortex $\partial\Omega_v$. The mathematical formulation of the model is represented by the equation

$$\nabla^2\psi = -\omega H\left(\psi_s - \psi\right) \tag{2.2}$$

where $H(\cdot)$ is a two level piecewise-constant distribution, ω is the constant vorticity and ψ_s is the value of the streamfunction on the vortex boundary. According to this model, the wake is a region with closed streamlines bounded by the body, the solid wall and the interface with the external flow.

A lower order model of the 2D inviscid vortex dynamics past bodies is provided by a point vortex system: the flow is described by an irrotational field with some vortex singularities immersed within. Most solutions of flow control problems are related to this model (Zannetti & Iollo (2003) [83] and Protas (2008) [54]). The relationship between the point vortex model and the vortex patch model was investigated by several authors. Examples and references can be found in Elcrat *et al.* (2000) [22], Crowdy & Marshall (2004) [19], Zannetti & Chernyshenko (2005) [78] and Zannetti (2006) [77]. Elcrat *et al.* consider the Föppl curve pertinent to the flow past a semicircular bump, which is the locus of the point vortex in equilibrium. For this simple geometry, they present some evidences that for each point vortex there is a related family of vortex patches with increasing area A and the same circulation

γ. They show that the point vortex solution is interesting as it is the seed of a family of finite area vortex regions. If A is the parameter that defines a member of the family, the point vortex corresponds to first element with $A = 0$ and the Batchelor-like patch corresponds to the last one. In [77] the Föppl curve has been

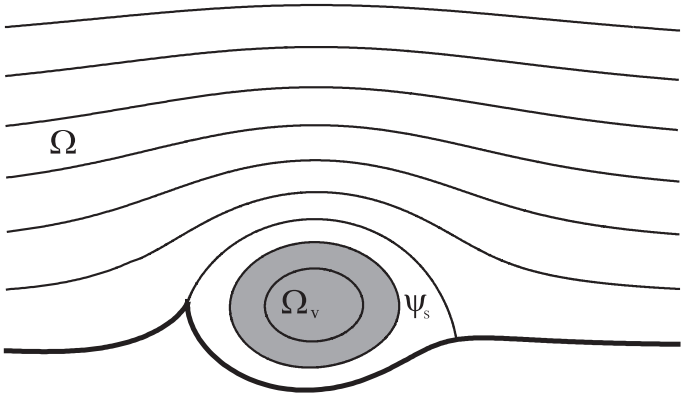

Figure 2.1. Flow domain and vortex patch

generalized to any locally deformed wall, that is the locus of point vortices that stand in equilibrium is defined for any arbitrary obstacle. There it is argued that, as well as for the semicircular bump, a family of growing vortex patches can be associated with each standing point vortex. It is also shown that when the obstacle presents a sharp edge, then there is a finite number of standing point vortices that satisfy the Kutta condition.

Our main conjecture is that if there is not one standing point vortex that satisfies the Kutta condition, then the associated family of growing patches, including the Batchelor-like patch, does not exist either. This supposition implies that cusped obstacles without standing point vortices and respecting Kutta do not admit a finite area wake at high Reynolds numbers.

The main purpose of this study is to verify this conjecture and, also, to show the existence of vortex patch families located past certain cusped bodies. This chapter is organized as follows: in section 2.1 the existence of standing vortex past wall-mounted plates bounded in a channel is discussed with numerical and analytical evidences; in section 2.2 we detected some complete vortex families past cusped obstacles placed in an unbounded stream.

2.1 Prandtl-Batchelor channel flows past plates

In this section we treat the flow past plates at normal incidence inside a parallel wall channel. Some general references of the matter here presented can be found in [27] and [29]. This problem is characterized by symmetry and the flow can be studied in an half-plane, by replacing the symmetry line with a wall. In figure 2.2 the geometrical setting is presented: we considered a flat plate and a cambered plate that protrude from the wall.

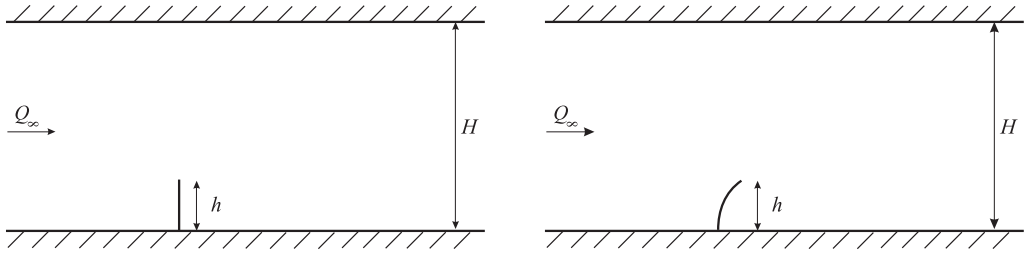

Figure 2.2. Geometries considered in the channel flow: Q_∞ is the free stream velocity, h is the reference length, H is the blockage. The Reynolds number is defined as $Re = Q_\infty h/\nu$.

Existence, *uniqueness* and *stability* of the solution at large Reynolds numbers past the flat plate are recurrent and controversial concepts in the literature. It started off with the Kirchoff's free streamline model, where the wake past the plate is modelled by a stagnation region. Later on, Batchelor introduced his model and this subject has since been widely examined. Smith & Clark (1986) [67] showed that past a flat plate there is not a standing point vortex satisfying the Kutta condition. Chernyshenko & Castro (1993) [12] verified that for enough large values of Reynolds number the steady eddy behind an isolated plate grows indefinitely with Re, that is $L \propto \mathrm{Re}$ where L is the closed wake length.

For a channel flow, Turfus (1993) [71] numerically detected a finite area vortex patch by explicitly computing the shape of the recirculating region. The existence of a closed solution was further investigated by Turfus & Castro (2000) [72], who checked the compatibility of a cyclic boundary layer with the Batchelor-like solution found by Turfus. In relation to this closed wake solution they proposed the existence of a bifurcation branch in the graph representing the wake length versus the Reynolds number. This conjecture would suppose that in the limit of the Reynolds number tending to infinity there is a finite vortex patch past the flat plate.

In figure 2.3 we reported the schematic diagram in the (L,Re)-space proposed by Turfus & Castro showing the bifurcation structure. The solid line represents the eddy length for an isolated plate, as in Fornberg (1991) [25] and Chernyshenko &

Castro (1993). The dotted line represents the solutions set for a channel flow: the 'upper' branch indicates the open wake scenario at large Reynolds numbers, whereas the 'lower' branch points out the scenario of a closed wake Prandtl-Batchelor solution. Recently Castro (2002) [10] obtained other computational results in accordance with the secondary branch, but reported some difficulties in reaching a good convergence on the grid beyond a certain Reynolds number.

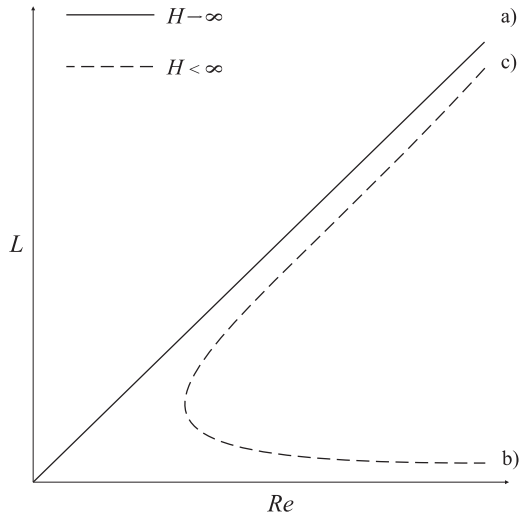

Figure 2.3. Bifurcation branch graph. a) growing wake unbounded solution, Chernyshenko & Castro (1993); b) closed wake bounded solution, Turfus & Castro (2000); c) continued branch, growing wake bounded solution.

Known that for such flow no equilibrium exists for a point vortex, then we argue that the respective standing vortex patch family does not exist either. In our opinion the controversial results found in the literature arise from the short convergence of numerical results. On the other hand, it can be shown that, for a curved plate, there is a stationary point vortex respecting the Kutta condition, and some vortices of finite area can be detected by means of a continuation procedure. In the following section we present some analytical and numerical techniques in order to investigate this problem.

2.1.1 Point vortex solutions

Let us consider the channel flow past a flat plate. The non-existence of a point vortex standing in equilibrium was demonstrated in Zannetti (2006) [77] by means of the generalized Föppl curve for any arbitrary body protruding from a wall. In this case the equilibrium manifold and the manifold of the point vortices satisfying

the Kutta condition do not intersect. It is demonstrated that a flat plate does not admit a standing vortex that respects the Kutta condition at the plate tip. Some examples of stabilization of this vortex wake are studied in [83].

Now we investigate the point vortex equilibrium for a cambered plate. The geometry of the plate and the flow region are determined by the conformal mapping illustrated in appendix A.1.1. Following [77], on the mapped ζ-plane the complex potential w characterized by the uniform stream q and a point vortex with strength γ and position ζ_0, is introduced

$$w = q\ \zeta + \frac{\gamma}{2\pi i}\log\left\{\frac{\sinh[(\zeta-\zeta_0)/2]}{\sinh[(\zeta-\zeta_0^*)/2]}\right\}$$

As in [77] we determined the equilibrium manifold and the vortex strength at the equilibrium points by imposing the vortex velocity to zero. On the physical z-plane, where $z = z(\zeta)$, the Hamiltonian H_z is defined by following the approach adopted in Zannetti & Franzese (1994) [79]. The locus of point vortices that respect the Kutta condition is found by imposing at the edge the separation point, i.e. the velocity is not singular. At the edge the mapping derivative is null $(\mathrm{d}z/\mathrm{d}\zeta)_{\zeta=0} = 0$, then, since the complex velocity is defined by $(\mathrm{d}w/\mathrm{d}z)_{z(0)}$, the condition to enforce on the mapped plane is $(\mathrm{d}w/\mathrm{d}\zeta)_{\zeta=0}$. Therefore the intersections between the 'equilibrium manifold' and the 'Kutta manifold' represent the positions of a standing point vortex that satisfy the Kutta condition.

Figure 2.4 shows the vortex equilibrium locus, the Hamilton function contour lines and the Kutta manifold. At the bottom of figure 2.4, the Hamiltonian field shows two elliptic equilibrium points and an hyperbolic equilibrium point close to the plate edge. The Kutta manifold crosses the right-hand-side elliptic fixed point, where it is placed a standing point vortex. If the stream at infinity is taken unit, the vortex circulation is $\gamma = -14.153$ and the position in the z-plane is $z_0 = 1.575 + \mathrm{i}\ 0.844$.

An alternative numerical technique was devised in order to evaluate the equilibrium position of a vortex behind a bluff body in a channel. Let us consider a rectangular flow domain Ω inside the channel, where Γ_n, Γ_s, Γ_e, Γ_w are the upper, lower, right and left boundaries. The flow field generated by a vortex singularity of circulation γ and position (x_v,y_v), immersed in a stream of undisturbed velocity Q_∞, is defined by the following PDE non-linear problem

$$\nabla^2\psi = \gamma\delta\left(x - x_v,\, y - y_v\right) \quad \text{in } \Omega \tag{2.3}$$

where ψ is the stream function, $\delta(\cdot)$ is the Dirac delta function. We define the conditions for a channel flow on the boundaries

$$\psi = 0,\ \ \psi \in \Gamma_s;\quad \psi = Q_\infty H,\ \ \psi \in \Gamma_n \tag{2.4}$$

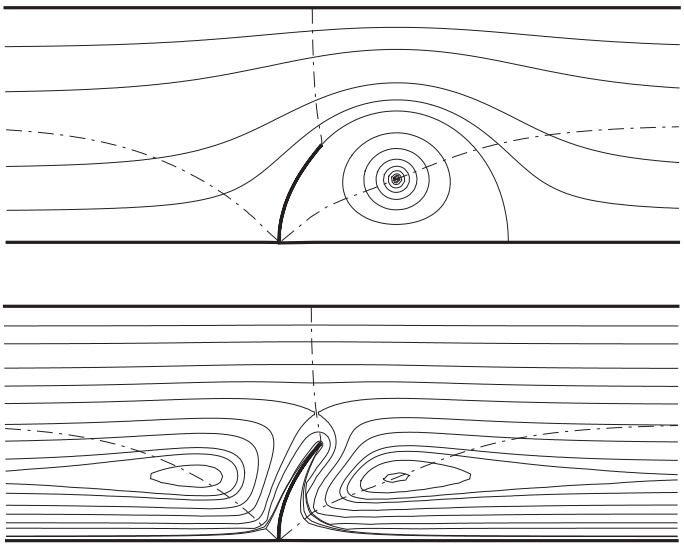

Figure 2.4. Curved plate in a channel flow. At top the streamlines pattern is traced and at bottom the Hamiltonian contour lines are shown. The dotted line represents the equilibrium manifold.

$$\frac{\partial \psi}{\partial n} = 0, \;\; \psi \in \Gamma_w; \;\; \frac{\partial \psi}{\partial n} = 0, \;\; \psi \in \Gamma_e \tag{2.5}$$

. The equilibrium condition is expressed by the ODEs

$$\dot{x}_v = 0, \;\; \dot{y}_v = 0 \tag{2.6}$$

By means of the Green function, the flow field is described by

$$\psi = \psi^0 + \frac{\gamma}{2\pi}\left(\psi' + \log\sqrt{(x-x_v)^2 + (y-y_v)^2}\right) \tag{2.7}$$

where ψ^0 is an auxiliary function that solves once and for all the Laplace problem, with the physical boundary conditions 2.4 and 2.5. ψ' is the preliminary Green function (see [40]). Therefore ψ' satisfies

$$\nabla^2 \psi' = 0, \;\; \text{in } \Omega \tag{2.8}$$

$$\psi' = -\log\sqrt{(x-x_v)^2 + (y-y_v)^2}, \;\; \psi' \in \Gamma_n \cup \Gamma_s \tag{2.9}$$

$$\frac{\partial \psi'}{\partial n} = -\frac{\partial}{\partial n}(\log\sqrt{(x-x_v)^2 + (y-y_v)^2}), \;\; \psi' \in \Gamma_w \cup \Gamma_e \tag{2.10}$$

The Green function of the operator ∇^2 with the boundary conditions 2.4, 2.5 is then $\psi' + \log\sqrt{(x-x_v)^2+(y-y_v)^2}$.

The equilibrium position and the intensity of the point vortex are now investigated. The finite velocity constraint at the edge of the plate is enforced in order to compute the strength γ: the equation 2.7 is linear, then by fixing the location of the vortex the flow field is uniquely determined. A model of the Kutta condition has to be taken into account so that the separation point is at the plate tip, i.e. the tangential velocities on the sides close to the edge have to be the same. The tangential velocity can be defined by $(\partial\psi/\partial n)^{\pm}$ where $\pm$ indicates the side of the plate at the cusp. The Kutta condition is then imposed through the equation

$$\left(\frac{\partial\psi}{\partial n}\right)^{+} = -\left(\frac{\partial\psi}{\partial n}\right)^{-} \tag{2.11}$$

The equilibrium condition is found when $(\dot{x}_v,\dot{y}_v) = 0$. The vortex velocity in a Cartesian frame of reference is

$$\dot{x}_v = \frac{\partial}{\partial y}(\psi^0 + \gamma\psi')|_{(x_v,y_v)} \quad \dot{y}_v = -\frac{\partial}{\partial x}(\psi^0 + \gamma\psi')|_{(x_v,y_v)} \tag{2.12}$$

The PDE problem 2.3 with the boundary conditions 2.4, 2.5, the Kutta condition 2.11 and the equilibrium condition 2.12, represent a non-linear problem that can be solved iteratively.

Our computations were performed by a FreeFem++ [52] script over an unstructured grid of 27247 triangles and $P2$ continuous finite element, that is $P2_h = \{v \in H^1(\Omega)/\forall K \in T_h, v|_K \in P2\}$. The number of the degrees of freedom is 55186 and the number of the elements at the boundaries is 691. The vortex circulation computed is γ =-14.190 and the position in the physical plane is z_0 =1.578+i 0.845, this result shows an appreciable agreement with the above analytical solution as well.

2.1.2 Distributed vortex solutions

The mathematical statement for the vortex patch problem is directly derived from the equation 2.2 and is set as follows

$$\nabla^2\psi = -\omega H\left(\psi_0 - \psi\right), \text{ in } \Omega \tag{2.13}$$

$$\psi = 0, \ \psi \in \Gamma_s; \quad \psi = Q_\infty, \ \psi \in \Gamma_n \tag{2.14}$$

$$\psi = Q_\infty y, \ \psi \in \Gamma_w; \quad \frac{\partial\psi}{\partial n} = 0 \ \text{ or } \ \psi = Q_\infty y, \ \psi \in \Gamma_e \tag{2.15}$$

This problem is strongly non-linear and the numerical survey of the existence of steady distributed vortices seemed sensitive to the initial conditions and was grid dependent. It was usually solved by explicitly determining the geometry of the separatrix ψ_0 ([64], [71], [5]), but some difficulties were reported when the patch tended to the Batchelor-like solution for $\psi_0 \to 0$. On the other hand, the numerical techniques presented in this work are based on approximating 2.13 on a grid, where the separatrix is detected implicitly as a jump of vorticity. In the following paragraphs we directly solved such a problem for the considered geometries by means of two different numerical strategies.

The first technique, discussed in [26], was originally devised for the flat plate case. In this work the non-existence of a Prandtl-Batchelor (ψ_s=0) solution was suggested by various preliminary numerical results. These results are provided by a Newton-based finite difference code, where a Schwarz domain-decomposition method [39] was applied to overcome the memory requirement. The computations were performed on two 833MHz Alpha 64-bit processors. A survey of the convergence on the grid was performed until a maximum grid refinement of 44590 points. Starting from these issues, we improved the Newton-Schwarz code by adopting a GMRES iterative solver with an ILUT preconditioner [60]. The results here presented are computed with a grid resolution of $\approx$ 500000 points, in the case of the maximum aspect-ratio flow domain. Two controversial behaviours are found for such a problem. By imposing

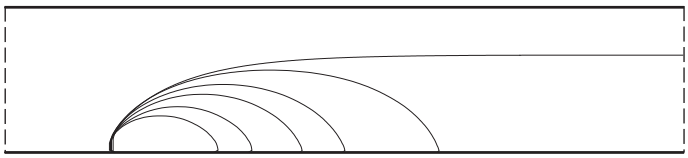

Figure 2.5. Solution grid dependence. The solutions are computed on a more and more fine grid and the wake tends to be open as the grid is refined.

a Neumann condition at downstream the vortical region opens from the plate tip; in figure 2.5 the grid dependence of the solution is reported. In figure 2.6 we compared the solutions obtained by imposing a Dirichlet condition at downstream, with three different lengths of the computational domain. In this example the vortex region is closed but grows when the domain size is increased, that is, the closing point of the separatrix is not invariant with the domain size. Thus, the numerical simulations on fine grids do not show any finite wake solution for a flat plate at normal incidence.

The second numerical technique is devised for the curved plate case and is subsequently described. We discussed, in 2.1.1, about the standing point vortex solution

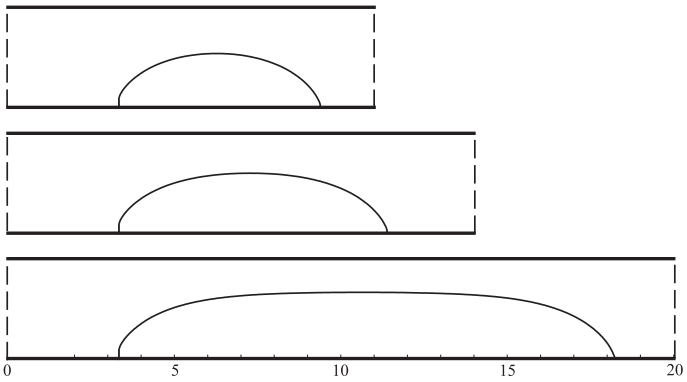

Figure 2.6. Dirichlet condition at downstream: the wake length depends on the longitudinal domain size.

past a curved plate. By means of the following numerical method we continued on ψ_s the point vortex solution in order to detect a finite vortex patch family. The new solution method is based on the Schauder fixed point theorem (see, for instance, [30]). Let us consider the notation in figure 2.1. The flow field can be solved as $\psi = \psi^0 + \omega\psi'$, that is the superposition of the potential solution ψ^0, as in the point vortex case, and a function ψ'. In particular ψ' has to satisfy

$$\nabla^2\psi' = 0, \ \text{ in } \ \Omega - \Omega_v \tag{2.16}$$

$$\nabla^2\psi' = 1, \ \text{ in } \ \Omega_v \tag{2.17}$$

$$\psi' = 0, \ \ \psi \in \Gamma_s \cup \Gamma_n \tag{2.18}$$

$$\frac{\partial\psi'}{\partial n} = 0 \ \text{ or } \ \psi' = 0, \ \ \psi' \in \Gamma_w \tag{2.19}$$

$$\frac{\partial\psi'}{\partial n} = 0, \ \ \psi' \in \Gamma_e \tag{2.20}$$

where Ω_v is the support of $H(\psi_s - \psi)$. The vorticity ω is solved by imposing the Kutta condition 2.11. The algorithm consists on iterating the equation

$$\nabla^2\psi^{n+1} = -\omega^n H(\psi_s - \psi^n) \ \text{ in } \ \Omega \tag{2.21}$$

and this procedure has fixed points. The continuation parameter ψ_s is fixed *a priori*. ψ^0 is determined once and for all at the iteration 1, whereas ψ'^n and ω^n

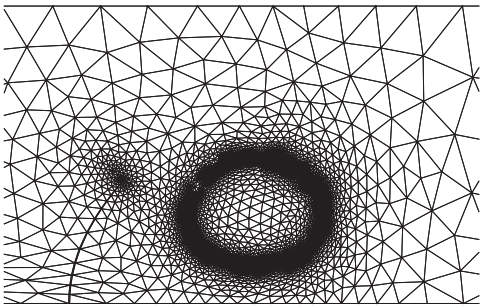

Figure 2.7. Adaptative mesh refinement based on the vorticity and streamfunction gradients.

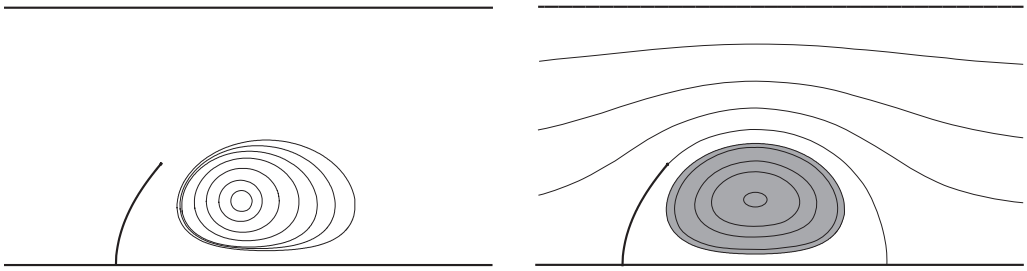

Figure 2.8. Partial finite area vortex family obtained by desingularization of the standing point vortex (left). Streamlines for the patch $\psi_s = -0.8$ (right).

can be determined when Ω_v is given. At the n+1 iteration, the flow field defines a new shape of the support Ω_v until the convergence is gained. The numerical results are obtained by a FreeFem++ code that works on the same unstructured grid adopted for the point vortex case. The convergence on the grid is achieved by an auto-adaptative mesh refinement (figure 2.7).

The numerical solution of the PDE 2.3 is introduced as initial guess and, by varying ψ_s, we continued the finite vortex patch obtaining several elements with increasing area. This procedure could not be completed for the whole vortices family. For larger area vortex patches, the number of triangles generated by the auto-adaptative mesh algorithm, in order to detect the vortex boundary, exceeded the constraint of the computational resources, and the respective solutions could not be computed. In other terms, an excessive memory requirement during the adaptative mesh-generation step did not allow to complete the whole patches family. On the left-hand side of figure 2.8 the 'partial' vortex family is shown and on the right-hand side the flow field for the vortex with ψ_s=-0.8 is reported. The vorticity and the circulation computed for this case are ω =-7.069 and γ =-17.193.

2.2 Unbounded vortex patches past cusped bodies

In section 2 a survey of the multiplicity of the closed-streamline equilibrium Euler solutions was presented. By considering the Bernoulli constant jump as vanishing, the space of the parameters that defines a standing vortex is relevant to two degrees of freedom: circulation γ and area A, otherwise the value of the separatrix stream-function ψ_s. When a cusped obstacle protrudes in the flow domain, if the solution respects the Kutta condition, the space of the parameters reduces to one $\gamma = \gamma(A)$.

In present section we investigate on the continuation of a given vortex patch through the (γ,ψ_s) parameter space. In addition, we gave further numerical consistency to the main conjecture about the non existence of finite wake when there is not one standing point vortex respecting the Kutta condition.

In [28], an analytical proof is argued demonstrating that a finite vortical region can be locally continued with respect to both vorticity and the separatrix streamline ψ_s. In the following section, some examples that verify the existence of the entire family from the point vortex to the Batchelor-like solution past certain cusped bodies are illustrated. These results are obtained by a mixed analytical-numerical method that allows to attain high accuracy with standard computational resources. A first discussion on this procedure was presented in [80].

2.2.1 A family of cusped bodies

The sharp edge is a typical device that enforces the Kutta condition, thus avoiding the uncontrolled separation phenomena. In the above section we discussed how the breaking of symmetry of the flat plate allows to trap a point vortex and the related vortex patch family. If we consider other symmetric cusped bodies, such as a semi-circular bump (see Föppl (1913) [24], Elcrat *et al.* (2000) [22]) or a symmetric Ringleb snow cornice (see Ringleb (1961) [58]), it is demonstrated that do not exist standing point vortices with the starting separation point on the symmetry line. In Zannetti (2006) [77] it is shown that even though such symmetric bodies do not admit vortices in equilibrium, there are other symmetric cusped obstacles that supply one or more standing vortices satisfying the Kutta condition.

Let us consider a generalization of the Ringleb snow cornice, which is represented by the conformal mapping

$$z = \zeta + \frac{(-\zeta_1)^{N+1}}{N(\zeta - \zeta_1)^N} \tag{2.22}$$

that maps the upper ζ-half-plane onto a wall extending to infinity with a protruding cusped body. The camber and the symmetry are determined by the index N and ζ_1.

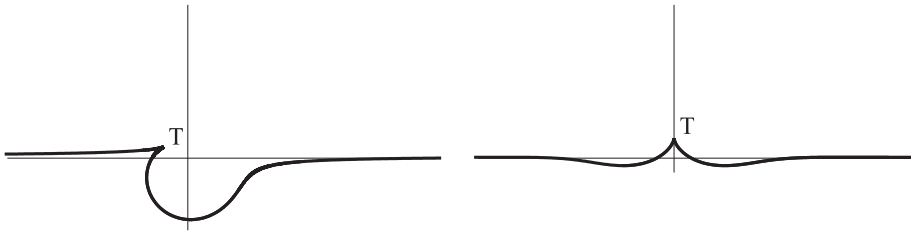

Figure 2.9. Non-symmetrical and symmetrical snow cornices. T identifies the cusp.

If $\mathrm{Re}(\zeta_1)$=0, the cornice is symmetric. The complex potential for the undisturbed stream q_∞ on the upper-half of the z-plane extending to infinity, having a point vortex with a strength γ and location z_0 immersed within, is defined by

$$w(z) = q_\infty z + \frac{\gamma}{2\pi \mathrm{i}} \log \frac{(z - z_0)}{(z - 1/z_0^*)}. \tag{2.23}$$

where $(\cdot)^*$ indicates the complex conjugate. In [77] it is verified by means of the Föppl generalized curve that for the symmetric Ringleb cornice $N = 1$ the 'equilibrium manifold' and the 'Kutta manifold' do not intersect. By increasing N, the number of equilibrium loci crossing the 'Kutta manifold' increases, therefore more standing point vortices are found.

Two geometries are considered in following examples. In figure 2.9 the flow domains obtained from the variation of the Ringleb's cornice mapping are shown. The body on the left-hand side is obtained by setting $\zeta_1 = 0.2 - \mathrm{i}\ 0.075$, $N = 1$ while that on the right-hand side is obtained by fixing $\zeta_1 = -\mathrm{i}$ and $N = 5$. For the first geometry, a single standing point vortex respecting Kutta was found ($z_1 = 0.045 - \mathrm{i}\ 0.199$, $\gamma_1 = -2.469$). On the other hand the symmetric case presents two intersections between the manifolds, corresponding to a 'low-energy' solution $z_L = 0.612 + \mathrm{i}\ 0.310$, γ_L=-4.810 and an 'high-energy' solution $z_H = 4.544 + \mathrm{i}\ 2.623$, $\gamma_H = -32.964$.

2.2.2 Numerical method

An accurate method to solve the non linear Poisson equation 2.13 in unbounded and simply connected domains is here presented. We discussed in section 2.1.2 on the high grid resolution that is required in order to detect accurately the vortex shape. Since the physical domain extends to infinity, the computational domain should be large in comparison to the rotational region, but, nevertheless, it should be finite. Furthermore a direct numerical solution by finite differences or finite elements on a limited computational domain would need some suitable artful boundary conditions.

Let us consider the figure 2.1 where it is shown how the rotational core, defined by the streamline ψ_s, is embedded in the potential flow. Our approach is based on a domain decomposition strategy that allows to solve the flow domain Ω separating a small internal sub-domain (i), pertinent to the sharp edge and the rotational core Ω_v, and the external flow field (e) extending to infinity. The internal region is solved by an adaptation of the fixed-point algorithm described in section 2.1.2, while the external flow is analytically solved by means of the potential flow theory.

An iterative procedure based on the Steklov Poincaré iteration (see [57]) matches the solution between the two subdomains. If ∂_c is the common line bounding two computational regions, the inner subdomain is solved by imposing a Dirichlet boundary condition $\psi_i|_{\partial_c} = \psi_e|_{\partial_c}$, and the outer subdomain is solved by fixing the Neumann boundary condition $(\partial\psi_e/\partial n)_{\partial_c} = (\partial\psi_i/\partial n)_{\partial_c}$.

The method devised is based on conformally mapping the physical domain into some transformed planes where both the numerical solution of the inner subdomain and the analytical solution of the outer subdomain are straightforward. In figure 2.10a the z-plane is represented where a wall extending to infinity with a non-symmetrical cusped obstacle is shown. The internal region (i) is bounded by ∂_c and the portion of wall between the points A,B. The external domain (e) is located above the ∂_c and the rest of the wall and extends to infinity. This cusped body is obtained by applying the conformal mapping previously discussed on the upper half-λplane

$$z = \lambda + \frac{(\mathrm{i})^2}{(\lambda + \mathrm{i})} \tag{2.24}$$

As shown in figure 2.10b, the boundary line ∂_c on the physical z-plane is the result of mapping a semi-circle on the λ-plane. A successive simple mapping transforms the inner semi-circular region onto a unit semi-circle (figure 2.10c)

$$\lambda = \frac{\mu}{a} + b \tag{2.25}$$

where the parameters a,b are such that $\lambda_A = \lambda(-1)$ and $\lambda_B = \lambda(1)$. By means of a transformation based on the Jacobi elliptic sine-amplitude function sn (see [70]), the upper half-μ-plane can be mapped onto the rectangle of the ζ-plane, as presented in figure 2.10d. The rectangle is constituted by two half-ractangle, the upper corresponding to the external region and the lower to the internal region. Then the mapping function is

$$\mu = \frac{\mathrm{sn}[\zeta,m]}{d} \tag{2.26}$$

with m elliptic modulus and d a scaling parameter. The elliptic modulus m is the complete elliptic integral of the first kind and $K'(m) = K(1-m)$. The scaling

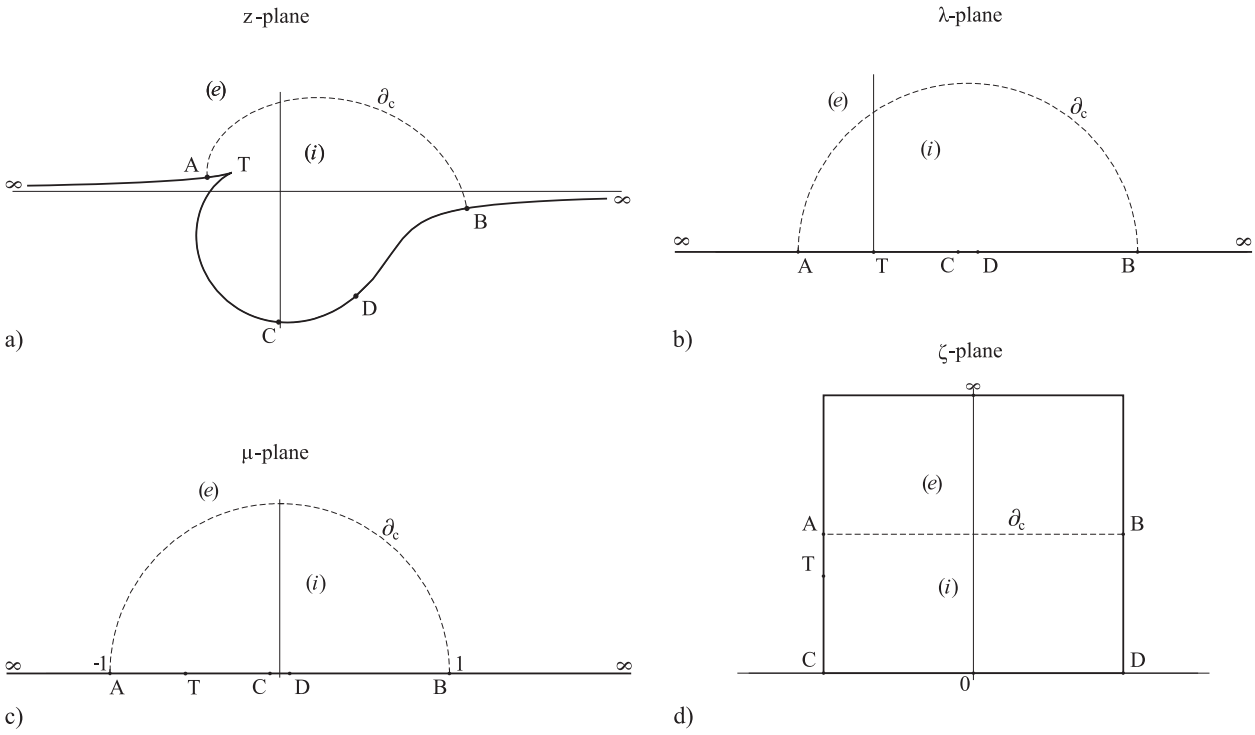

Figure 2.10. Mapping sequence.

factor d is a free parameter and defines the positions z_C,z_D of the points C,D on the physical plane; in our computations it is determined by imposing $\mu_B = \mathrm{sn}[\zeta_B,m]/d$.

A numerical grid-based method is applied to solve the inner region. The lower half rectangle of the ζ-plane can be appropriatly traced on an evenly-spaced Cartesian grid. For an accurate enforcement of the Kutta condition, the value of m has to be chosen such that ζ_T coincides with a node. By letting the side CA of the half-rectangle be divided into p elements and placing T onto the n-th node, it is found that

$$\zeta_T = -K(m) + \mathrm{i}(n/p)K'(m)/2, \tag{2.27}$$

thus the equation

$$\mu_T = \frac{\mathrm{sn}[-K(m) + \mathrm{i}(n/p)K'(m)/2,m]}{\mathrm{sn}[-K(m) + \mathrm{i}K'(m)/2,m]} \tag{2.28}$$

is thus defined, which, by means of an iterative procedure, allows to compute the proper value of the elliptic module m. On the left-hand side of figure 2.11 an

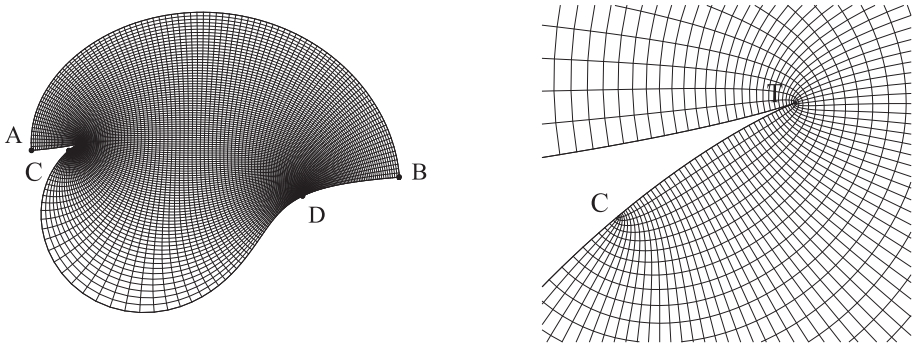

Figure 2.11. Grid topology generated by the mapping (left). The cusp coincides with a grid node (right).

example of the computational grid is shown. On the right-hand side a detail on the connection between the edge and a grid node is reported.

The numerical procedure adopted to solve the inner region, discussed in section 2.1.2, is hence modified. The equation 2.13 can be adjusted such that it can be solved on the transformed ζ-plane. If we define $\zeta = \xi + \mathrm{i}\ \eta$ as the independent variables and $\nabla^2_\zeta = \partial^2_\xi + \partial^2_\eta$, it is easily demonstrated that the equation valid on the ζ-plane is

$$\nabla^2_\zeta \psi = \left[-\omega H(\psi_s - \psi)\right]/J \ \text{ in } \ \Omega_i, \tag{2.29}$$

where $J = |\mathrm{d}z/\mathrm{d}\zeta|^2$ is the Jacobian of the transformation and Ω_i is the ABCD internal subdomain. Now we indicate as Γ_{AB}, Γ_{CD}, Γ_{AC}, Γ_{BD} respectively the upper, the lower, left and right boundaries of the ζ-plane. On the boundaries we have the following Dirichlet conditions

$$\psi = 0, \ \ \psi \in \Gamma_{AC} \cup \Gamma_{CD} \cup \Gamma_{BD} \tag{2.30}$$

$$\psi = \psi_e, \ \ \psi \in \Gamma_{AB}, \tag{2.31}$$

where ψ_e comes from the external subdomain. As discussed in 2.1.2, the flow field ψ is obtained by $\psi = \psi^0 + \omega\psi'$ for $\psi \in \Omega_i$, where ψ^0 solves the Laplace problem with proper boundary conditions and ψ' satisfies the non linear problem deduced by the equations 2.16, 2.17 and the homogeneous Dirichlet boundary conditions:

$$\nabla^2_\zeta \psi' = 0, \ \text{ in } \ \Omega_i - \Omega_v \tag{2.32}$$

$$\nabla^2_\zeta \psi' = \frac{1}{J}, \ \text{ in } \ \Omega_v \tag{2.33}$$

$$\psi' = 0, \ \ \psi' \in \Gamma_{AC} \cup \Gamma_{CD} \cup \Gamma_{DB} \cup \Gamma_{AB} \tag{2.34}$$

The Kutta condition is imposed on the transformed ζ-plane by setting as null the tangential velocity

$$\frac{\partial \psi}{\partial \xi}\Big|_{\zeta_T} = 0 \tag{2.35}$$

The fixed-point iterations are performed on the equation

$$\nabla^2_\zeta \psi^{n+1} = \frac{1}{J}\left[-\omega^n H\left(\psi_s - \psi^n\right)\right] \tag{2.36}$$

that is the equation 2.21 transformed on the ζ-plane. A linear under-relaxation factor f_r is introduced, so that we have the following update $\psi^{n+1} = f_r\psi^n + (\psi^0 + \omega^{n+1}\psi'^{n+1})\,(1 - f_r)$.

The potential flow in the external region Ω_e is analytically solved on the μ-plane. The complex potential w_e is defined as

$$w_e(\mu) = Q_\infty \mu + \sum_{j=1}^{\infty} a_j \mu^{-j}, \tag{2.37}$$

where $a_j \in \mathbb{R}^1$. If q_∞ is the undisturbed velocity at infinity on the z-plane, Q_∞ can be defined as

$$Q_\infty = q_\infty \lim_{\mu\to\infty}\left(\frac{dz}{d\mu}\right) = \frac{q_\infty}{a}. \tag{2.38}$$

On the μ-plane, the subdomain Ω_e corresponds for $\mathrm{Im}[\mu] > 0$ to the complement of the unit semi-circle ∂_c and the set $-\infty < \mu \leq -1$, $1 \leq \mu < \infty$ for $\mathrm{Im}[\mu] = 0$ is the image of the wall in the external subdomain. The complex potential 2.37, where a_j is a real coefficient, is defined such that the impermeability condition is satisfied on the solid boundary, i.e. $\psi|_{\mathrm{Im}[\mu]=0} = const.$

Let us take $\mu = \rho\exp(\mathrm{i}\phi)$; the boundary condition on the common line ∂_c is then imposed by deducing ψ_i from the inner region and by enforcing the Neumann boundary condition

$$\left(\frac{\partial \psi_e}{\partial \rho}\right) = \left(\frac{\partial \psi_i}{\partial \rho}\right). \tag{2.39}$$

Since the normal to ∂_c derivative on the μ-plane can be mapped to the normal derivative on the ζ-plane by

$$\left(\frac{\partial \psi_e}{\partial \rho}\right) = \left(\frac{\partial \psi_i}{\partial \eta}\right) / \left|\frac{d\mu}{d\zeta}\right| \tag{2.40}$$

and by setting

$$g(\phi) = \left(\frac{\partial \psi_e}{\partial \rho}\right)_{\rho=1} \tag{2.41}$$

the inner solution $\psi_i|_{\partial_c}$ provides $g(\phi)$ in the interval $0 \leq \phi \leq \pi$. The wall impermeability gets $g(0) = g(\pi) = 0$, thus $g(\phi)$ can be continued in the interval $\pi < \phi < 2\pi$ by imposing a symmetry referred to the real axis. Since

$$\mathrm{Im}\left[\frac{dw_e}{d\mu}\exp(\mathrm{i}\phi)\right] = \left(\frac{\partial \psi_e}{\partial \rho}\right)_{\rho=1} \tag{2.42}$$

the equation 2.37 one the common boundary Γ_{AB} becomes

$$g(\phi) = Q_\infty \sin\phi - \sum_{j=1}^{\infty} j a_j \sin(j\phi). \tag{2.43}$$

When this series is suitably truncated, the equation provides the coefficients a_j, that are tuned with the boundary conditions. The Steklov-Poincaré-like algorithm is performed solving iteratively the inner and the outer region until ψ_i and ψ_e converge on ∂_c. Here, the same under-relaxation factor f_r adopted for the fixed-point solver in the internal region is introduced, such that the updating formula becomes $\psi_e^{n+1} = (1 - f_r)\tilde{\psi}_e^{n+1} + f_r \psi_e^n$, where $\tilde{\psi}_e^{n+1} = \mathrm{Im}[w_e^{n+1}(\phi)]$.

The main computational cost of the present approach can be attributed to the solution of the Poisson problem on the grid at each fixed-point iteration. The fast Poisson solver is adopted here (Fishpack90 library [3]) and it allows to attain high grid refinement with a standard performance PC. All our computations have been done on AMD Athlon 64 3000+ 1.81 GHz CPU with 1 Gb RAM. Examples of the CPU time required to solve the Batchelor problem starting from the point vortex as initialization are shown in table 2.1.

Let $\mathrm{Err}_2^{\%}(\psi|_{\partial_c})$ be the error per cent in l^2-norm, computed with ψ_e and ψ_i along the common boundary ∂_c. In figure 2.12 $\mathrm{Err}_2^{\%}(\psi|_{\partial_c})$ is reported versus the number of Steklov-Poincaré iterations. The convergence threshold is set at 10^{-7}.

Let us consider the non-symmetrical cusped body defined above in section 2.2.1. For this case, we determined the standing point vortex satisfying Kutta ($z_1 = x_1 + \mathrm{i}y_1 = 0.045 - \mathrm{i}\ 0.199$, $\gamma_1 = -2.469$). We verified the accuracy of this numerical

f_r	iterations	CPU time $[s]$
0.25	37	630
0.40	10	300
0.50	7	250
0.60	10	570
0.75	19	1270

Table 2.1. Steklov-Poincaré iterations and CPU time by varying the under-relaxation factor.

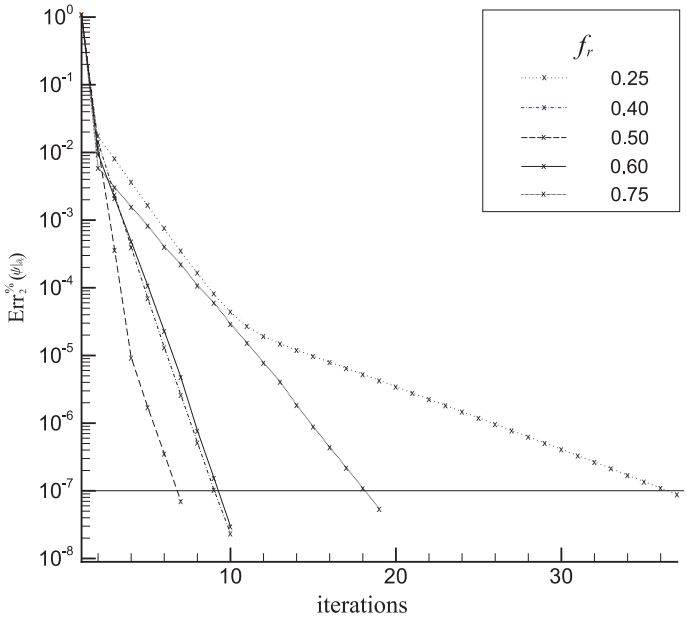

Figure 2.12. Rate of convergence of the Steklov-Poincaré algorithm by varying the under-relaxation factor f_r. On the diagram, the $\psi|_{\partial_c}$ error per cent in l^2-norm *versus* the iteration number is reported.

method comparing this analytical solution and the analogous numerical solution obtained coupling the new far-field boundary conditions with the PDE 2.3 as discussed in section 2.1.1. The boundary conditions 2.4-2.5 are modified into

$$\psi^0 = 0, \;\; \psi' \in \Gamma_{AC} \cup \Gamma_{CD} \cup \Gamma_{BD} \tag{2.44}$$

$$\psi^0 = \psi_e, \;\; \psi' \in \Gamma_{AB} \tag{2.45}$$

and the boundary conditions for the preliminary Green function 2.9-2.10 are altered in

$$\psi' = -\log\sqrt{(x-x_1)^2+(y-y_1)^2},\ \ \psi^0 \in \Gamma_{AC}\cup\Gamma_{CD}\cup\Gamma_{BD} \tag{2.46}$$

$$\psi' = \psi_e - \log\sqrt{(x-x_1)^2+(y-y_1)^2},\ \ \psi^0 \in \Gamma_{AB}. \tag{2.47}$$

On the left-hand side of figure 2.13, the streamline pattern of the point vortex solution is shown. According to the l^2-norm, the error of the stream function along the common boundary ∂_c is $O\left(10^{-6}\right)$ and the error on the value of the vortex circulation is $O\left(10^{-6}\right)$ for a 1000×1000 grid. On the right-hand side of figure 2.13 the respective Batchelor-like solution is illustrated.

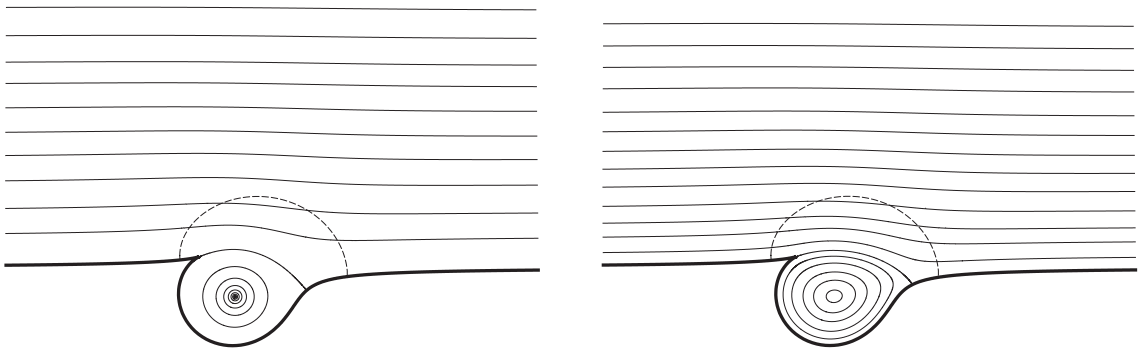

Figure 2.13. Point vortex solution (left); Prandtl-Batchelor solution (right). The dashed line represents the common boundary.

2.2.3 Examples of finite area vortex families

In this section we present some numerical results of growing vortex patches obtained by means of the procedure discussed above. The obstacle considered is the symmetrical snow cornice described in section 2.2.1. Two standing point vortex solutions satisfying the Kutta condition are admitted. By varying the free parameter ψ_s we try to desingularize the point vortex into the Batchelor flow, in order to obtain the entire patch family.

Let us consider the 'low-energy' point vortex solution ($z_L = 0.612 + \mathrm{i}\ 0.310$, γ_L=-4.810). The respective computed family of vortex patches is shown in figure 2.14 and the streamline pattern for the Batchelor-like solution is presented in figure 2.15. In figure 2.16 the trajectories - 'Kutta lines' - taken by the entire vortex patch family respecting the Kutta condition on two different parameters spaces are

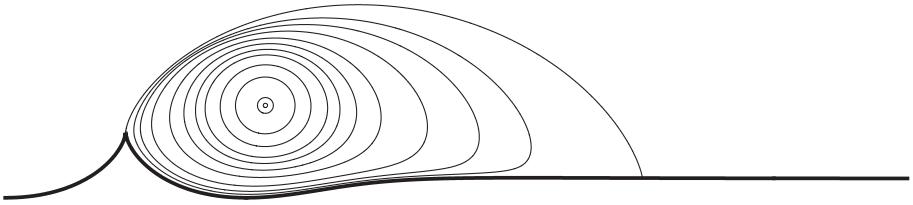

Figure 2.14. Family of vortex patches desingularizing the 'low energy' point vortex solution.

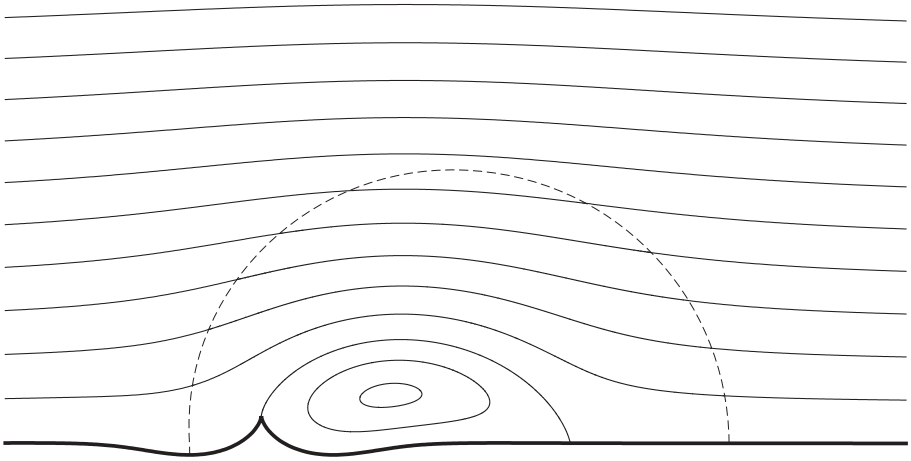

Figure 2.15. Flow field for the 'low-energy' Batchelor-like solution.

presented. On the left-hand side, the trajectory of patches on the (ω,ψ_s)- parameter space is shown. The entire curve cannot be displayed because the point vortex solution reveals an infinity vorticity ω. The trajectory is completely shown in the equivalent plane (γ, A) presented on the right-hand side, where γ is the circulation and A the patch area. The trajectory starts at $A = 0$, pertinent to the point vortex, and ends with the maximum area corresponding to the Batchelor-like solution.

Let us now consider the 'high-energy' point vortex solution (z_H = 4.544+i 2.623, γ_H=-32.964). In this case, since the standing point vortex is further distant from the cusp and the solid wall than the 'low-energy' solution, the complete finite area vortex family extends onto a larger support. We increased Ω_i and the number of grid points with the intent of keeping the same mesh refinement. The excessive computational cost represented a limit to this continuation procedure. Starting from the point vortex solution, the rotational core becomes larger and larger as ψ_s approaches to

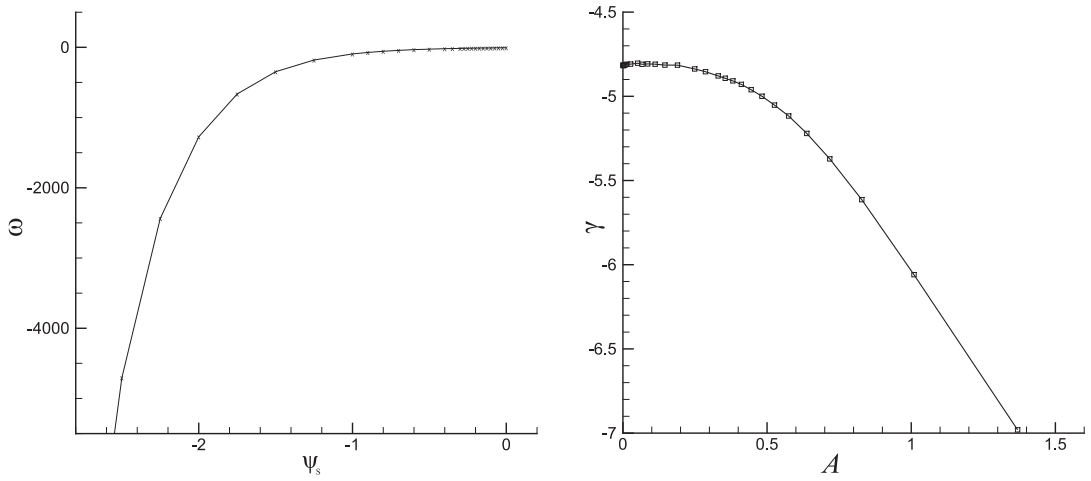

Figure 2.16. Trajectories in the parameter spaces.

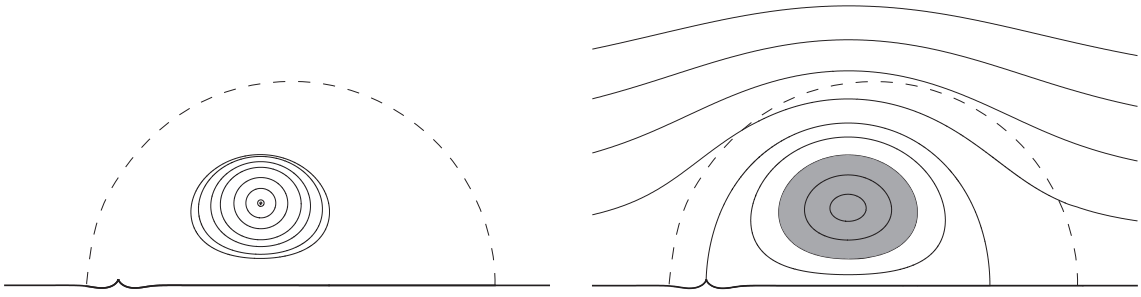

Figure 2.17. Continuation from the 'high-energy' point vortex solution. On the left-hand side the vortex patches correspond respectively to $\psi_s = -24,\ -18,\ -10, -7,\ -5,\ -4,\ -3,\ -2.5$.

zero, but, if the inner domain Ω_i is not large enough to contain the recirculating region, the numerical method tends to be attracted by a solution belonging to the 'low-energy' family.

On the left-hand side of figure 2.17, some finite vortex patches obtained from the 'high-energy' point vortex solution are illustrated. The continuation has been interrupted since the resulting solutions would be related to the 'low-energy' family. On the right-hand side a streamline pattern for $\psi_s = -2.5$ is shown.

As final instance, we investigated about the solutions where the Kutta condition is not respected. If the Kutta condition is not imposed, the space of the solution

acquires a degree of freedom, that is, a local displacement from the 'Kutta line' can be attained. If we introduce ω as a new free parameter, then a solution is defined by an arbitrary choice of ψ_s and ω. The diagram reported at top of figure 2.18 illustrates, on the (ω, ψ_s) parameters space, the local perturbation from a solution P that satisfies the Kutta condition. Two pair of solutions are investigated, both by varying ω for $\psi_s = \psi_{s,\mathrm{P}}$ and by varying ψ_s for $\omega = \omega_{\mathrm{P}}$.

Since our numerical method sets the value of vorticity by the separation condition, the solutions A_1, A_2 are computed by imposing the separation point before the sharp edge and behind it respectively, while an iterative procedure on ψ_s determines the vortex patch areas corresponding to ω_{P}. On the other hand, the solutions B_1, B_2 are obtained by placing the separation point in front of the cusp and behind it, and letting ψ_s be fixed to $\psi_{s,\mathrm{P}}$. In the table 2.2 the data associated to the solutions shown in figure 2.18 are summarized.

solution	ψ_s	A	Γ	ω
P	-0.5	0.189	-4.811	-25.481
A_1	-0.646	0.221	-5.628	-25.482
A_2	-0.392	0.163	-4.156	-25.481
B_1	-0.5	0.227	-5.103	-22.456
B_2	-0.5	0.156	-4.563	-28.593

Table 2.2. Data collection of the vortex patches obtained by a local perturbation of a solution satisfying the Kutta condition.

2.2.4 Vortex-capturing airfoil

With minor variations, the above method can be used to solve the Batchelor flow past an airfoil equipped with a vortex-capturing cavity [1]. We designed a test symmetrical airfoil with a vortex cell by means of a chain of conformal mappings, as described in appendix A.1.2. The airfoil is mapped from the physical z-plane onto the real axis of the σ-plane, as shown in figures 2.19 and 2.20. The σ-plane plays the same role as the μ-plane in section 2.2.2. The half-unit-circle defines two subdomains and the mapping $\sigma = \mathrm{sn}[\zeta,m]/d$, which corresponds to 2.26, transforms the mapped ζ-plane onto the σ-plane. In this geometrical setting the Steklov-Poincaré procedure is adopted. The computation in the inner region is carried out as above, while the external flow has a differently defined complex potential. With reference to figure 2.20, we can notice that the physical infinity is mapped onto $\sigma = \sigma_\infty$ and that the airfoil is mapped onto the real axis, with the point Q mapped onto the point at infinity on the σ-plane. The complex potential w_e can be written

as

$$w_e = \frac{M}{\sigma - \sigma_\infty} + \frac{M^*}{\sigma - \sigma_\infty^*} + \frac{\gamma}{2\pi \mathrm{i}} \log\left(\frac{\sigma - \sigma_\infty}{\sigma - \sigma_\infty^*}\right) + \sum_{j=1}^{\infty} b_j \sigma^{-j} + w_0. \tag{2.48}$$

The first two terms are a doublet and its mirror image, which represent the flow velocity at the physical infinity, the third term is a vortex and its mirror image, pertinent to a vortex at the physical infinity, and the fourth term is a series whose coefficients are real, $b_j \in \mathbb{R}^1$. The complex potential is such that $\psi_e = const$ on the real axis of the σ-plane, that is, the impermeability condition on the solid walls is satisfied. The doublet momentum M is defined by the value of the asymptotic flow velocity $q_\infty \exp(\mathrm{i}\alpha)$, where α is the incidence, thus, as explained in appendix A.1.2, it can be obtained by the equation:

$$q_\infty \mathrm{e}^{-\mathrm{i}\alpha} = \lim_{\sigma \to \sigma_\infty} \frac{\mathrm{d}w_e/\mathrm{d}\sigma}{\mathrm{d}z/\mathrm{d}\sigma}. \tag{2.49}$$

The value of the total circulation past the airfoil and trapped vortex is given by γ, which is defined by enforcing the Kutta condition at the trailing edge, $(\mathrm{d}w_e/\mathrm{d}\sigma)_{\sigma_T} = 0$. The series coefficients b_j are found by enforcing the Neumann boundary condition $(\mathrm{d}\psi_e/d\rho) = (\mathrm{d}\psi_i/d\rho)$ along the common boundary ∂_c, with $\sigma = \exp(\mathrm{i}\phi)$ and with the $g(\phi)$ function now adopting the following form

$$g(\phi) = \mathrm{Im}\left\{\mathrm{e}^{\mathrm{i}\phi}\left[-\frac{M}{(\mathrm{e}^{\mathrm{i}\phi} - \sigma_\infty)^2} - \frac{M^*}{(\mathrm{e}^{\mathrm{i}\phi} - \sigma_\infty^*)^2} + \frac{\gamma}{2\pi \mathrm{i}}\left(\frac{1}{\mathrm{e}^{\mathrm{i}\phi} - \sigma_\infty} - \frac{1}{\mathrm{e}^{\mathrm{i}\phi} - \sigma_\infty^*}\right)\right]\right\} - \sum_{j=1}^{\infty} j b_j \sin(j\phi).$$

The circulation at infinity and the coefficients b_j of the truncated Laurent series depend on each other nonlinearly. Therefore, for each Steklov-Poincaré iteration, the computation of γ and b_j is perfomed by means of a fixed-point algorithm that converged in maximun 10 iterations.

Figure 2.21 shows an example of the streamline pattern as computed by this method for a Batchelor-like solution trapped by the cavity. The dashed line traces the boundary of the inner region Ω_i.

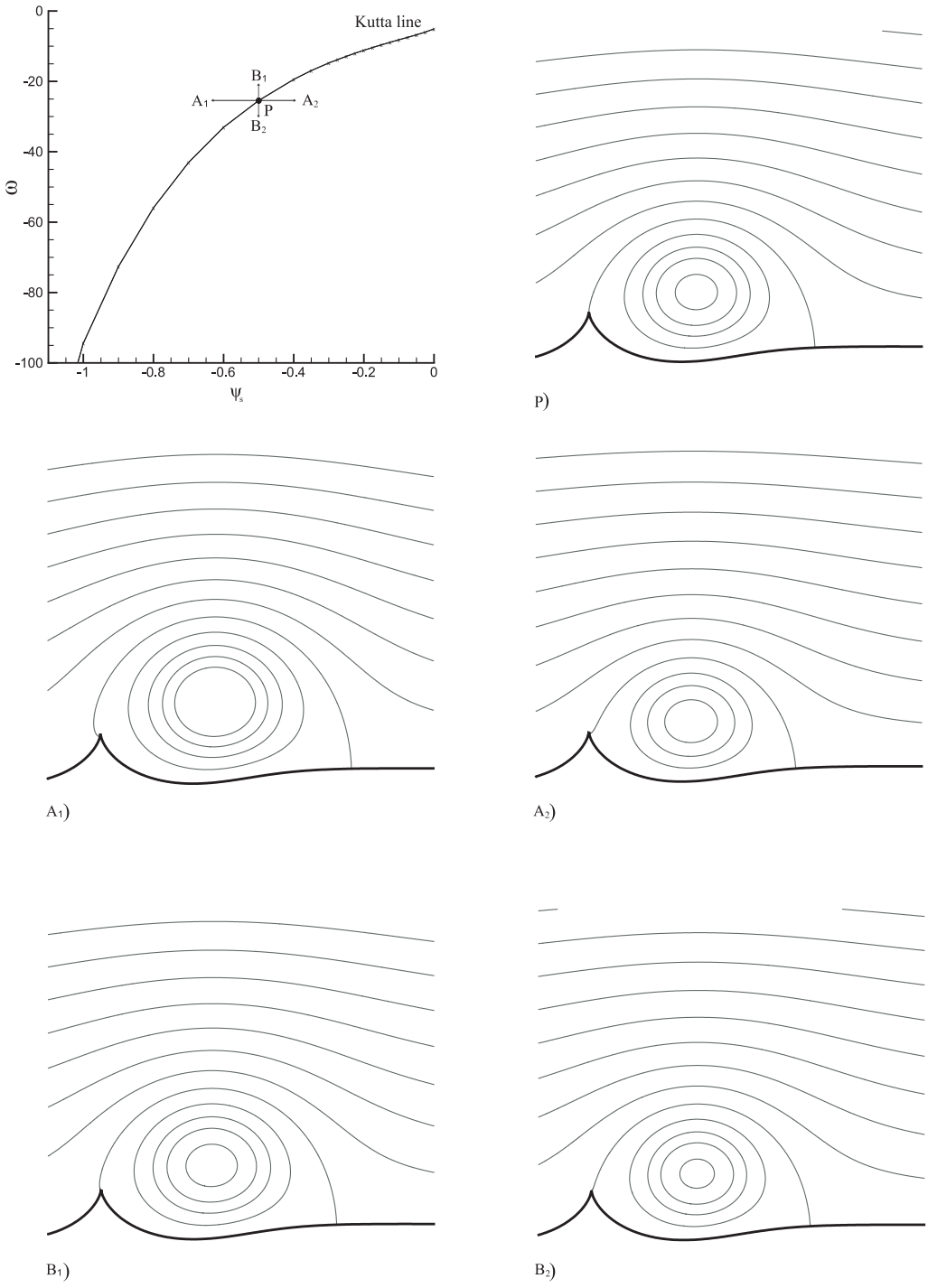

Figure 2.18. Standing solutions obtained by a local displacement from a point on the Kutta line. The vortex patch P is defined by $\psi_{s,\mathrm{P}}$=-0.5, A_{P}=0.189, γ_{P}=-4.811, ω_{P}=-25.481.

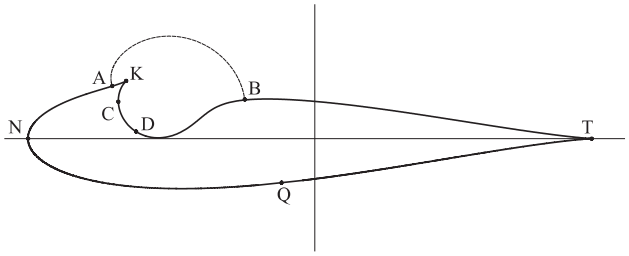

Figure 2.19. z-plane.

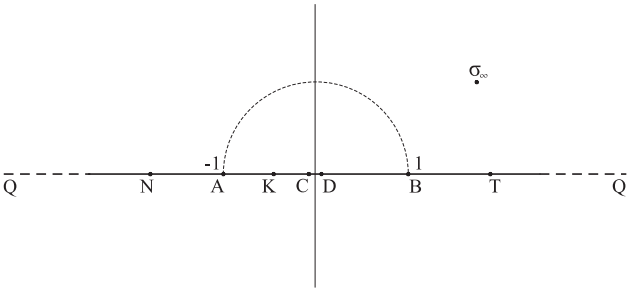

Figure 2.20. σ-plane.

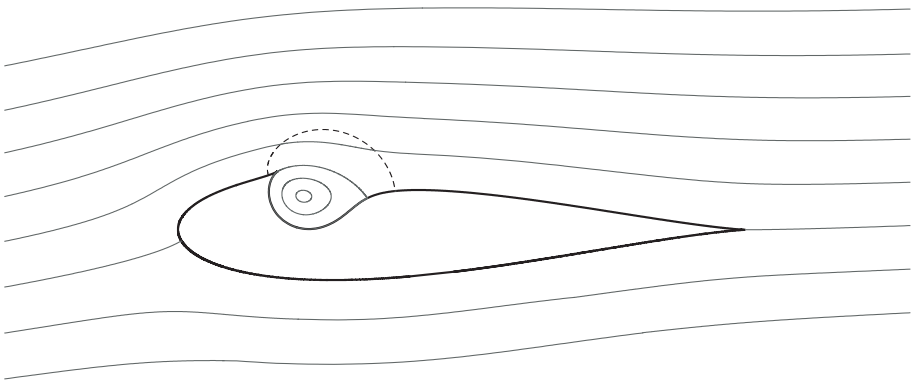

Figure 2.21. Streamlines at $\alpha = 5°$.

2.2.5 Mollified vortex families

In this section the existence of vortex solutions with non constant vorticity patch past some cusped bodies is discussed. Let us consider the Euler model for an incompressible steady flow defined by the equation 2.1. The distribution $\omega(\psi)$ within the recirculating region is not determined by the far field boundary conditions and defines a multiplicity of solutions. Some vortex solutions characterized by vorticity unconstant distribution are here computed. Such kind of cusped bodies admit

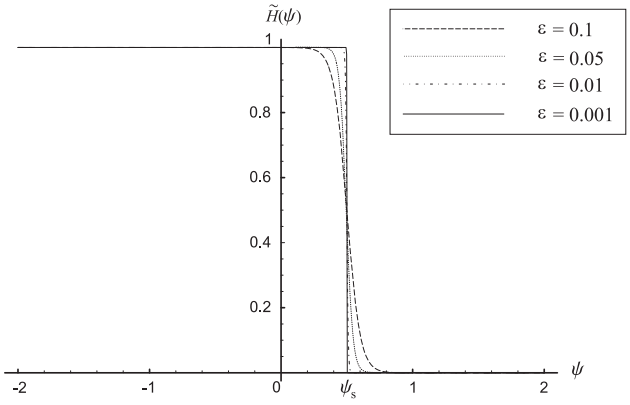

Figure 2.22. Mollified Heaviside function $\tilde{H}(\psi)$.

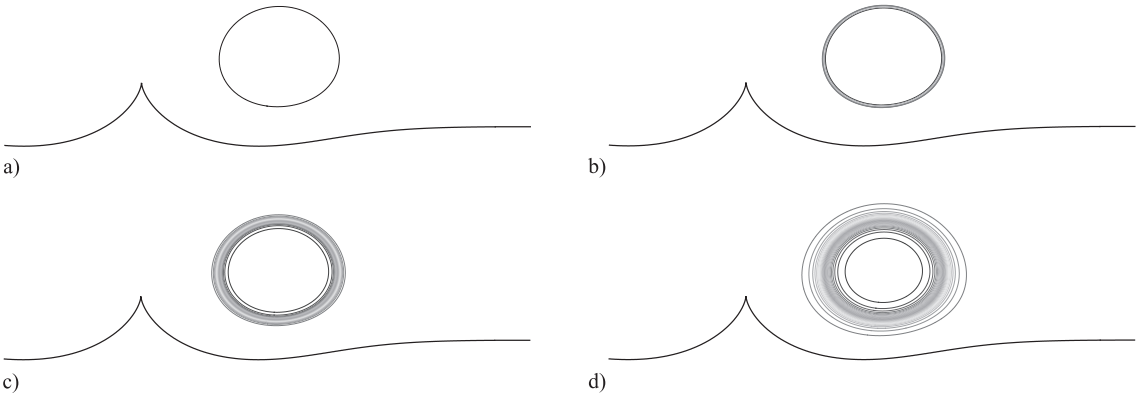

Figure 2.23. Iso-vorticity lines. The solutions are pertinent to $\epsilon \to 0$ and $\epsilon = 0.01, 0.05, 0.1$ respectively.

some constant vorticity patches, and these solutions can be computed by means of

a continuation starting from a point vortex standing in equilibrium and satisfying Kutta (section 2.2.3).

For such families of steady finite area vortex patches we examined the existence of solutions with non constant vorticity distribution. An investigation on these solutions is carried out by modifying of the equation 2.2, such that an non constant constant distribution $\omega = \omega(\psi)$ is determined, that is

$$\nabla^2\psi = -\omega\tilde{H}\left(\psi_s - \psi\right) \tag{2.50}$$

where $\tilde{H}(\cdot)$ is a mollified Heaviside function which smoothes the vorticity jump ω around the separatrix ψ_s. A one-parameter mollified Heaviside function defined as $\tilde{H}(\psi) = 1/2\tanh\left[-(\psi - \psi_s)/\epsilon + 1\right]$ is represented in figure 2.22 for four values of the parameter ϵ. This function is introduced in the algorithm discussed in section 2.2.2 and some numerical solutions are computed.

For instance, we took into consideration a constant vorticity patch with $\psi_s = -0.5$, obtained by the continuation from the low-energy point vortex solution. This solution is the initialization of a successive mollification of the vorticity jump by varying ϵ. In figure 2.23a the constant vorticity solution is shown. The other diagrams are referred to three arbitrary values of ϵ.

Since, for larger ϵ, the vorticity is spread on larger values of ψ, a shear of vorticity tends to reach the boundary of the inner region Ω_i and the numerical method does not converge.

2.3 Concluding remarks

In this chapter, some 2D steady vortex solutions of the incompressible Euler equations are found for some different classes of bodies at incidence. These obstacles are characterized by a sharp edge where the separation is enforced.

A channel-flow is studied for a flat plate and a cambered plate. The curvature of the plate represents a passive control technique that allows to stabilize the flow. For a given plate bend, some point vortex solutions which are in equilibrium and satisfy the Kutta condition are computed. Starting from these stable point vortex solutions, through a numerical continuation procedure, it is possible to find a family of vortex patches with constant vorticity. On the contrary, the flat plate does not admit a point vortex solution in equilibrium that satisfies the Kutta condition, and no vortex patches are found neither. This result is controversial because it contradicts the Turfus' conjecture about the existence of a Prandtl-Batchelor solution past a flat plate at incidence in a channel.

A class of 'snow cornice' obstacles is considered in an unbounded flow domain. A numerical-analytical procedure is devised in order to solve efficiently the flow at infinity and to attain an high order of accuracy nearby the recirculating region. Some finite constant vorticity regions, starting from the desingularization of the point vortex solution up to the Batchelor-like vortex patch, are computed. In addition, we presented some remarks and numerical examples of the possibility of continuing one of these vortex patches with steady Euler solutions characterized by a non-uniform vorticity distribution.

We assumed A, that is ψ_s, to be the parameter defining an element of a vortex patch family satisfying the Kutta condition. The point vortex solution is the first element with $A = 0$, while the Prandtl-Batchelor solution is the last element with constant vorticity in the entire region with closed streamlines. By means of a continuation procedure, we associated the existence of point vortex solutions, in a stable equilibrium state, with the existence of the whole family, both for unbounded flows and bounded flows. In a more general case, without satisfying the Kutta condition, the investigated examples show that vortex patch solutions of the Euler equations can be continued relating to both the vorticity ω and the value of the streamfunction defining the vortex core. In [28], the mathematical conditions under which vortex patch solutions can be continued with respect to both the vorticity ω and value ψ_s are widely discussed.

The results which we presented in this section, provided some evidences in favour of the fact that if there is not a standing point vortex that satisfies the Kutta condition, then the associated family of growing patches obtained by continuation, including the limiting Prandtl-Batchelor solution, does not exist either. In other terms this conjecture argues that if there is no point vortex solution, then there exists no finite wake in the inviscid limit.

Finally, the above method is adopted to solve the Batchelor flow past an airfoil equipped with a suitable vortex-capturing cavity.

Chapter 3

Vortex wake past a vertical axis turbine

In this chapter the unsteady two-dimensional flow field around a vertical axis wind turbine is studied. The main feature of a Vertical Axis Turbine (VAT) is a rotor shaft that works vertically driven by two or more blades. The most important applications of such turbines are in the field of the wind and hydraulic engineering.

The vertical axis turbines can be classified on the basis of the working principle of the blades. Some turbines exploit the drag of the blades in order to move the shaft. Such kind of turbines are defined as Savonius rotors, and the cup anemometer represents a typical example of such as architecture. On the other hand, the lift-based turbines work through the lift generated by the blades, which are in general characterized by an airfoil section. Such kind of turbines are named Darrieus rotors. We took into consideration the typical lift-based architecture as shown in figure 3.1. Among the advantages of this type of turbine we have the independence of the wind direction, the simple mechanical manufacturing and maintenance. On the other hand, the principal drawbacks are the unsteady pulsating torque generated, the low efficiency at high wind speeds compared to the horizontal axis architecture and the profit to the micro wind power generation ($<$ 100 kW) only. The main problem encountered with the aerodynamics of a Darrieus architecture is the complicated unsteady flow phenomena occurring during its working cycle. For each revolution the blades undergo a highly unsteady relative motion with large variations of incidence and absolute value of the relative velocity.

Let us consider a section that is normal to the shaft of the turbine, which rotates with a constant angular speed Ω. The observer is fixed on a blade section with a Cartesian orthogonal frame of reference with versors ($\mathbf{i}$,$\mathbf{j}$,$\mathbf{k}$). The absolute flow field is described on this moving frame of reference. Let $\mathbf{q}_\infty$ be the wind velocity at infinity, R the radius and $\theta(t) = (\Omega t)\mathbf{k}$ the angular position of a single blade. The

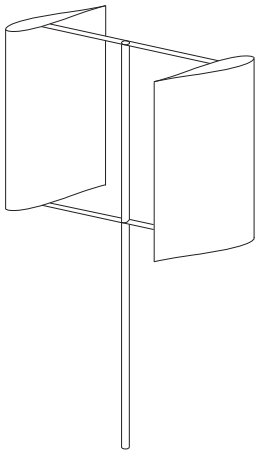

Figure 3.1. Sketch of a Darrieus two-blade vertical axis wind turbine.

relative velocity is determined by $\mathbf{V_r} = \mathbf{q}_\infty - \Omega\mathbf{k} \wedge \mathbf{R}$, where $\mathbf{q}_\infty$ is a rotating vector and the last term represents the translation velocity of the frame of reference. In figure 3.2, the kinematics of the velocities is presented on the hodograph plane. If Ω and q_∞ are constant, the envelope of the relative velocity is identified by a circle C, that gets larger as the rate $q_\infty/\Omega R$ increases.

The high and variable incidence of the stream generates a wide unsteady flow regime and, unlike the wake past an horizontal axis turbine, the blade motion is immersed in the wake generated. This complexity in the flow motion influences the perfomance of the turbine: dynamic stall can occur and the consequent uncontrolled flow detachment and vortex shedding result in high drag, low efficiency and unbalanced loads on the structure. Some recent techniques have been developed in order to design wings and blade sections such that operate in unfavourable conditions, such as in fully separated flow regime. The ongoing European research project [1] devised this technique especially to control the stall on the aircraft wings, but in general, as discussed above in chapter 2, the vortex trapping technique is attained with the aim of preventing the vortex shedding past an arbitrary bluff body. The vortex trapping technology consists of one or more vortex cells located on the profile, which act as a passive control device capable of avoiding the vortex shedding, thus enhancing the efficiency.

We propose to adopt these ideas with the aim of designing an unconventional lift-based profile for a VAT architecture. Since, in the model shown in figure 3.2, the incidence oscillates between opposite values, the traditional design consists of

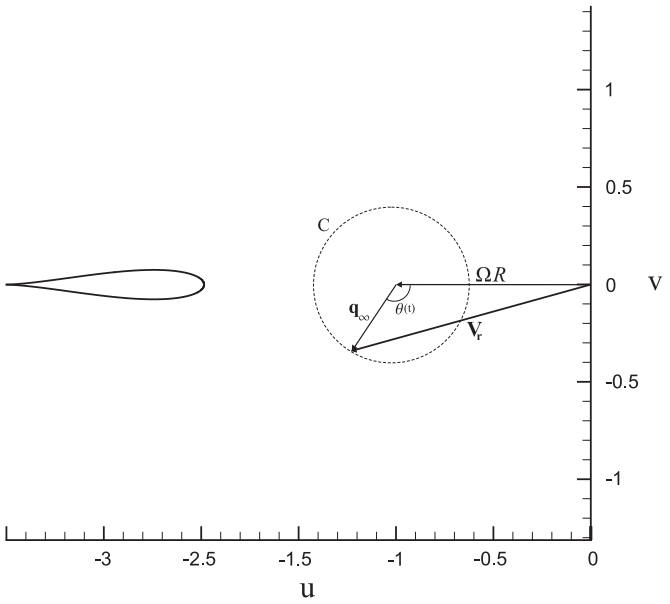

Figure 3.2. Velocity triangle on the odograph plane (u,v). The dashed line is the locus of the relative velocity V_r for $q_\infty/\Omega R = 1/4$.

symmetric blade sections which work at high angles of attack. We devised two identical cavities which are suitably located close to the leading edge in order to control the flow by making two vortex cells. The separation of the flow is forced at two cusped edges, two recirculating regions are generated and the reattachment of the flow occurs at the smooth cavity end. In the spirit of the vortex-cell technology developed by [1], we suppose that, at stall condition, the unsteadiness of the separation points is avoided and the flow pattern with trapped vortices is preserved. In addition, since at incidence the trapped vortices are not symmetric, the circulations of two vortex structures are time dependent and the airfoil acts as an adaptative airfoil that modifies its camber with the relative velocity. A preliminary design of such an airfoil was devised by means of a sequence of conformal mappings and a detailed report is presented in appendix A.1.3.

The aim of the present study is to survey on the vortex wake past the VAT architecture and, generally, to develop a set of analytical and numerical strategies *ad hoc* in order to describe the incompressible full unsteady flow past moving bodies. As final purpose, the development of such tools can be addressed to study the behaviour and performance of the new concept blade. We investigate on such problem by means of two different approaches. In section 3.1 the analysis is devoted to the study of the incompressible and inviscid flow field by means of a potential flow model.

In section 3.2, the unsteady incompressible Navier-Stokes equations are solved in terms of the vorticity equation. Both the methodologies consist of either mixed analytical-numerical or only numerical simulations of two dimensional phenomena governed by the incompressible Euler or Navier-Stokes equations. The solutions are attained through a Lagrangian description of the trajectories of vortex particles that approximate the distribution and the dynamics of the vorticity ([17]).

These two methods were devised with the aim of providing some efficient tools in the project of a vertical axis turbine. In the pre-project phase and without high computational resources, the inviscid analysis allow to determine the geometrical features (chord/radius ratio, position of the vortex-cell edges) and to estimate the performance of the turbine by varying the operating conditions. In a second phase, the turbine provided by the inviscid model, can be tested on the viscous solver and the aerodynamic design of the blade profile can be derived.

3.1 Inviscid analysis

The 2D unsteady inviscid rotational flow past moving bodies is addressed. The aim of this analysis is to develop a set of techniques which allow a modelization of the separation and a realistic survey of the instabilities and interactions of vortex structures in the wake past a vertical axis turbine.

The organization of this section is as follows. In section 3.1.1 we propose an analytical-numerical approach based on the conformal mapping theory and the blob vortex method that allows to describe the unsteady flow field. A vortex trapping profile is tested on a vertical axis turbine with single-blade configuration and the results are presented in section 3.1.2. Some first results referred to this topic were presented in Zannetti *et al.* (2007) [81]. An investigation of the vortex dynamics in a doubly connected domain is addressed in section 3.1.3, where the major reference is Zannetti *et al.* (2008) [82]. These results represent the preliminary suggestion to extend the analysis to the vortex wake past a two blades turbine configuration. In section 3.1.4 a low-order formulation of the two-blade configuration is presented. Finally a technique devoted to the evaluation of the turbine performances is discussed in section 3.1.5.

In this work, the airfoils adopted for the blade section of the vertical axis turbine, are obtained by some classical transformations, such as Joukowski's or Kármán-Trefftz's mappings, applied on one or two unit circles. On the other hand, it is important to remark that, by means of the theory of functions of complex variables (see, for instance, Moretti (1964) [43]), a generic simply connected region can be described by a chain of conformal mappings and transformed onto a circle. Moreover, as shown by Ives (1976) [33], a general mixed analytical-numerical conformal mapping method can be adopted to transform any doubly connected region with two arbitrary airfoils into two circles. Therefore the present inviscid analysis could be extended to a vertical axis turbine characterized by one or two blades with an arbitrary section's shape.

3.1.1 The blob vortex method

The inviscid model of two dimensional vortex shedding is based on the approximate description of the free shear layers by vortex particles. According to Clements (1973) [13] the vorticity is concentrated in point vortices and the flow is modelled as a potential flow with point singularities immersed within (*discrete* or *blob vortex method*). The unsteadiness of the flow field is such that the circulation around the bodies changes and the vortex singularities are shed by the separation points. At the beginning, the flow is at rest and the total circulation is null. Once the wind blows or the bodies move, the wake is generated by the shed vortices.

The vortex shedding is based on generating vortices at constant time intervals

in fixed locations close to the sharp edges. The circulation of each newly born vortex is determined by satisfying the Kutta condition, that is, by imposing the flow separation at the edges. As the vortex moves, the Kutta condition is not respected anymore, but it is restored as soon as a new vortex is generated.

This discrete description of the continuous evolution of vortex sheets and its validation are widely discussed in literature (see Clements (1973) [13] Kuwahara (1973) [38], Sarpkaya (1975) [65] and Kiya & Arie (1977) [36]. A general outline of the inviscid vortex methods can be found in Peters (1993) [50]). In the cited literature, a survey of the choice of the simulation parameters, such as release timing and distance d between the origin location and the edge, is provided. Though a possible asymptotic steady solution is independent from this choice, these parameters play an important role in the realistic description of the vortex shedding or transient phenomena.

The vortex method here implemented follows the same criteria used in Zannetti & Iollo (2003) [83]. If the wind velocity q_∞ and the airfoil chord c are chosen as reference velocity and reference length respectively, the distance d is ≈ 0.01, which is in the range recommended in literature. The position of the vortex release is located heuristically downstream from the sharp edge. The release of a new vortex depends on its strength, which has to be larger than a prescribed value. In our simulations the absolute value of the threshold for the vortex generation is 0.0001. The time-marching is determined by a second order scheme with an integration time-step $\Delta t = 0.001$, while the release time is defined as $\Delta t_o = k\ \Delta t$ where k is chosen within the range $1 \div 10$, depending on the simulation time.

The boundary conditions are deduced by the undisturbed velocity at infinity and the body impermeability. According to [41], for a moving body, the impermeability condition can be determined by imposing a suitable distribution of the streamfunction along the solid boundary. Let us define a frame of reference (x, y) fixed on the body and the curvilinear abscissa s which marks a point ($x_b(s)$, $y_b(s)$) on the solid moving wall. Since this frame of reference moves rigidly with the body, it is a relative frame of reference. The normal component of the absolute velocity is

$$\frac{\partial \psi_b}{\partial s} = (u - \Omega y_b)\frac{\mathrm{d}y_b}{\mathrm{d}s} - (v + \Omega x_b)\frac{\mathrm{d}x_b}{\mathrm{d}s} \tag{3.1}$$

where u,v and Ω are the translation and angular velocity components of the frame of reference in rigid motion. By integrating, we obtain the streamfunction of the absolute motion along the body

$$\psi_b(s) = u y_b(s) - v x_b(s) - \frac{1}{2}\Omega\left(y_b^2(s) + x_b^2(s)\right). \tag{3.2}$$

It is important to remark that, although this boundary condition is described on a

relative frame of reference, it is pertinent to the absolute flow field. In figure 3.3 a sketch illustrating the adopted nomenclature is presented.

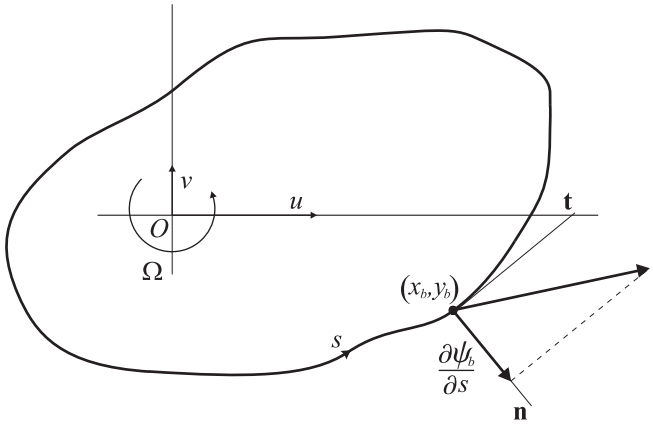

Figure 3.3. Deduction of the impermeability condition.

3.1.2 The single-blade model

We considered the flow past a turbine with a single blade, characterized by an airfoil equipped with two trapping cavities, as described in appendix A.1.3. In a frame of reference fixed on the blade, the complex potential can be defined on the ζ-plane, where $\zeta = \rho e^{i\phi}$ and the image of the blade section is the unit circle $\zeta_b(\phi) = e^{i\phi}$. Let $q_\infty e^{-i\alpha}$ be the complex velocity of the wind in the physical plane, the complex potential $w(\zeta)$ is

$$w = Q_\infty e^{-i\beta}\zeta + \frac{Q_\infty e^{i\beta}}{\zeta} + \frac{1}{2\pi i}\sum_{j=1}^{J}\gamma_j \log\frac{\zeta-\zeta_j}{\zeta-1/\zeta_j^*} + \sum_{n=1}^{N}\frac{(a_n + ib_n)}{\zeta^{n-1}} \tag{3.3}$$

where $Q_\infty e^{-i\beta} = \lim_{\zeta\to\infty} q_\infty e^{-i\alpha} dz/d\zeta$ and γ_j, ζ_j are the circulation and the position of the vortex singularities. The last term is a Laurent series that contains only the negative exponents. If the series is suitably truncated at a large value N, it can be determined so that the motion of the blade is taken into account. The a_n, b_n coefficients are real and can be tuned by the stream function distribution on the blade ψ_b, generally represented by equation 3.2. On the ζ-plane the image of the

blade contour is $\zeta = \mathrm{e}^{\mathrm{i}\phi}$, then the impermeability boundary condition is then set by

$$\begin{aligned} \mathrm{Im}[w(\zeta)]_{|\zeta|=1} &= \sum_{n=1}^{N} b_n \cos(n-1)\phi - a_n \sin(n-1)\phi \\ &= u y_b(\phi) - v x_b(\phi) - \frac{\Omega}{2}(x_b^2(\phi) + y_b^2(\phi)) \end{aligned} \tag{3.4}$$

where $u = \Omega R$, $v = 0$, $x_b(\phi) = \mathrm{Re}[z(\zeta(\phi))]$ and $y_b(\phi) = \mathrm{Im}[z(\zeta(\phi))]$.

The circulation of the newly born vortices is determined by imposing the Kutta condition at the sharp edges $\mathrm{E}_i = \mathrm{K}, \mathrm{K}^*, \mathrm{T}$. For a moving body the Kutta condition is satisfied when the relative velocity is not infinite at the cusps E_i. By means of the remarks discussed in appendix A.2.1, the Kutta condition is expressed by the equations

$$\mathrm{Im}\left[\frac{\mathrm{d}w}{\mathrm{d}\zeta}\mathrm{e}^{\mathrm{i}\phi}\right]_{\zeta_K} = 0,\ \mathrm{Im}\left[\frac{\mathrm{d}w}{\mathrm{d}\zeta}\mathrm{e}^{\mathrm{i}\phi}\right]_{\zeta_{K^*}} = 0,\ \mathrm{Im}\left[\frac{\mathrm{d}w}{\mathrm{d}\zeta}\mathrm{e}^{\mathrm{i}\phi}\right]_{\zeta_T} = 0. \tag{3.5}$$

These three equations represent a linear system where the unknowns are the circulations γ_K, γ_{K^*}, γ_T of the new vortices placed in the origin points close to the cusps. Furthermore, for each generation, the number J of the vortices in the wake is increased.

The vortex trajectories are computed by integrating in time the relative velocities $\dot{\zeta}^*_{r,v}$ in the transformed ζ-plane and then by mapping the new locations on the physical z-plane. Since the complex potential and the complex velocity are defined in the transformed plane, the choice of integrating the vortex velocities in the ζ-plane allows to save computational cost, because the vortex locations in the physical plane can not to be conserved. According to the Routh rule (see, for instance, [77], [13]) the conjugate relative velocity of the vortex in the physical plane is

$$\dot{z}^*_{r,V} = \left[\left(\zeta'^* - \frac{\gamma}{4\pi\mathrm{i}}\frac{\frac{\mathrm{d}^2 z}{\mathrm{d}\zeta^2}}{\frac{\mathrm{d}z}{\mathrm{d}\zeta}}\right)\frac{1}{\frac{\mathrm{d}z}{\mathrm{d}\zeta}}\right]_V - q^*_{t,V} \tag{3.6}$$

where $q^*_{t,V}$ is the velocity in the vortex location due to the transport of the frame of reference, and ζ'^*_V is the velocity that a free vortex should possess through the advection on the transformed plane, that is

$$\zeta'^*_V = \lim_{\zeta\to\zeta_V}\left(\frac{\mathrm{d}w}{\mathrm{d}\zeta} - \frac{\gamma_V}{2\pi\mathrm{i}}\frac{1}{\zeta - \zeta_V}\right). \tag{3.7}$$

The difference between ζ'^* and $\dot{\zeta}^*$ is meaningful. As regards $\dot{\zeta}^*$, it represents the rate of change of a particle location in the transformed ζ-plane during its physical

advection. On the other hand, ζ'^* is the advection velocity that a particle on the ζ-plane would possess in virtue of the complex potential.

Finally the relative velocity of the vortex in the ζ-plane can be expressed by

$$\dot{\zeta}^*_{r,V} = \frac{\dot{z}^*_{r,V}}{\left(\frac{\mathrm{d}z}{\mathrm{d}\zeta}\right)^*_V}. \tag{3.8}$$

In our simulations the numerical integration of the vortex trajectories was performed on a distributed memory HP Linux cluster platform, equipped with 9 nodes bi-dual core AMD Opteron 2.2 GHz. The Fortran library for the parallel communication is the free MPICH2 protocol.

Some visualizations and results of the flow past the single-blade turbine are presented subsequently. Let us consider an impulsively started motion, pertinent to a turbine whose blade-chord to turbine-radius ratio is $l/R = 1/2$ and whose turbine-speed to wind speed ratio is $q_\infty/\Omega R = 1/5$. In figure 3.4 a frame of the simulation is shown. The dots in the figure represent the point vortices. The different colours are related to the spin, red for the counter-clockwise and blue for the clockwise. The snapshot is taken at $t = 27$ and in the flow fields $J = 38239$ vortices are immersed. The streamline patterns pertinent to the relative and the absolute motion are shown

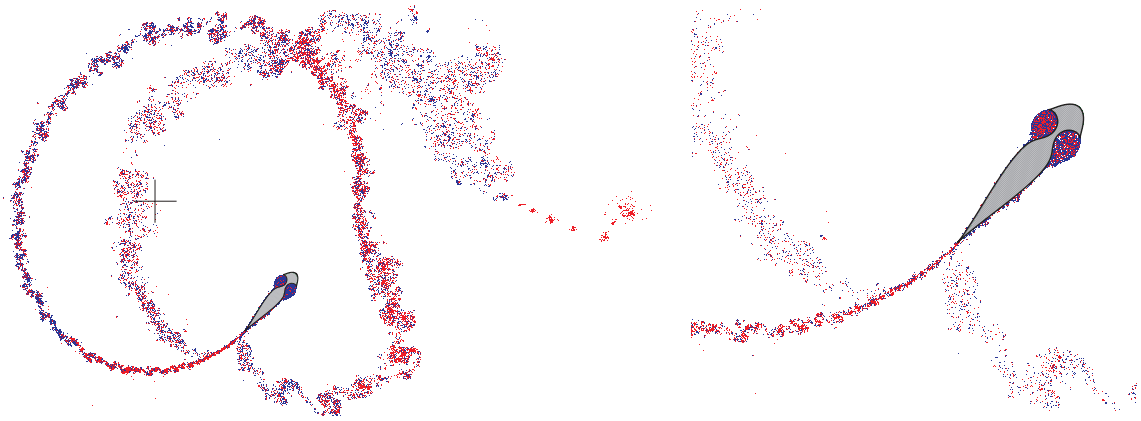

Figure 3.4. Vortex wake (left). Trapping vortex cavities and interaction with the wake (right). $q_\infty/\Omega R = 1/5$, $l/R = 1/2$.

in figure 3.5. The cavities entrap two vortex structures that are unsymmetrical because of the non-null angle of attack of the relative velocity. The snapshot is taken at $t = 0.01$ and the starting vortex is only just released by the trailing edge, as can be seen in the relative motion streamlines pattern is visible.

By increasing the speed ratio $q_\infty/\Omega R$ the envelope of the relative velocity is larger, as discussed in 3. The cavities operate at higher incidences and the vortex structures captured by the cavities can detach. For instance, the figure 3.6 shows two snapshots taken before and after the shedding of a vortex dipole, for a simulation where $q_\infty/\Omega R = 1/2$.

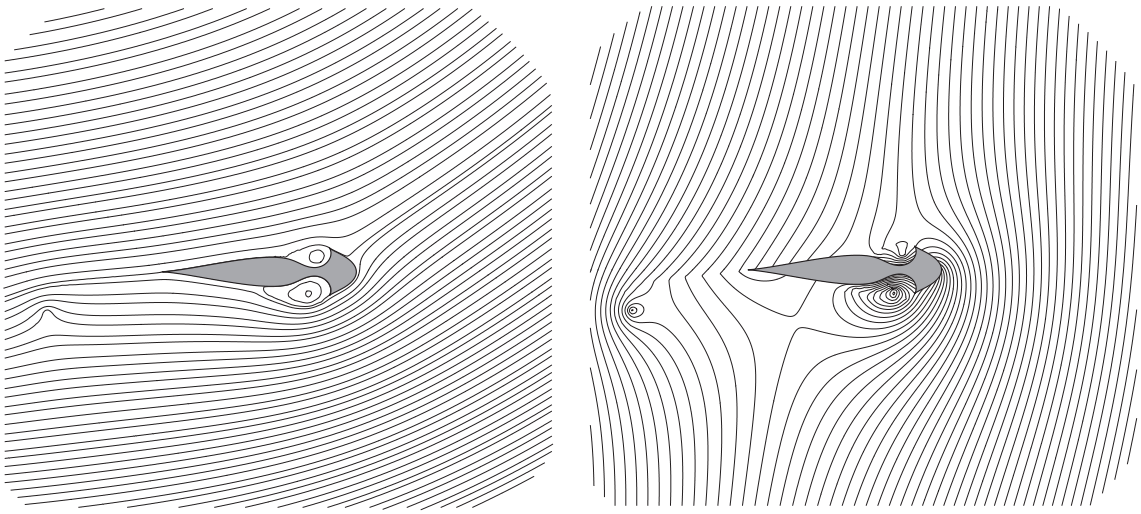

Figure 3.5. Streamlines field for a relative (left) and absolute frame of reference (right).

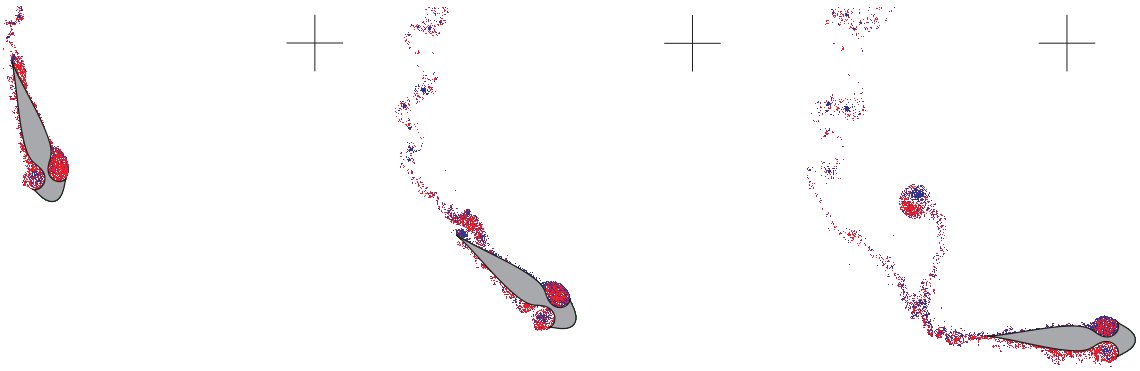

Figure 3.6. Detachment of a vortex dipole. Snapshots at $t = 0.275, 0.325, 0.375$. $q_\infty/\Omega R = 1/2$, $l/R = 1/2$.

These numerical examples show that vortical structures are generated and trapped by the cavities and that vortex shedding is prevented. In spite of the fact that this

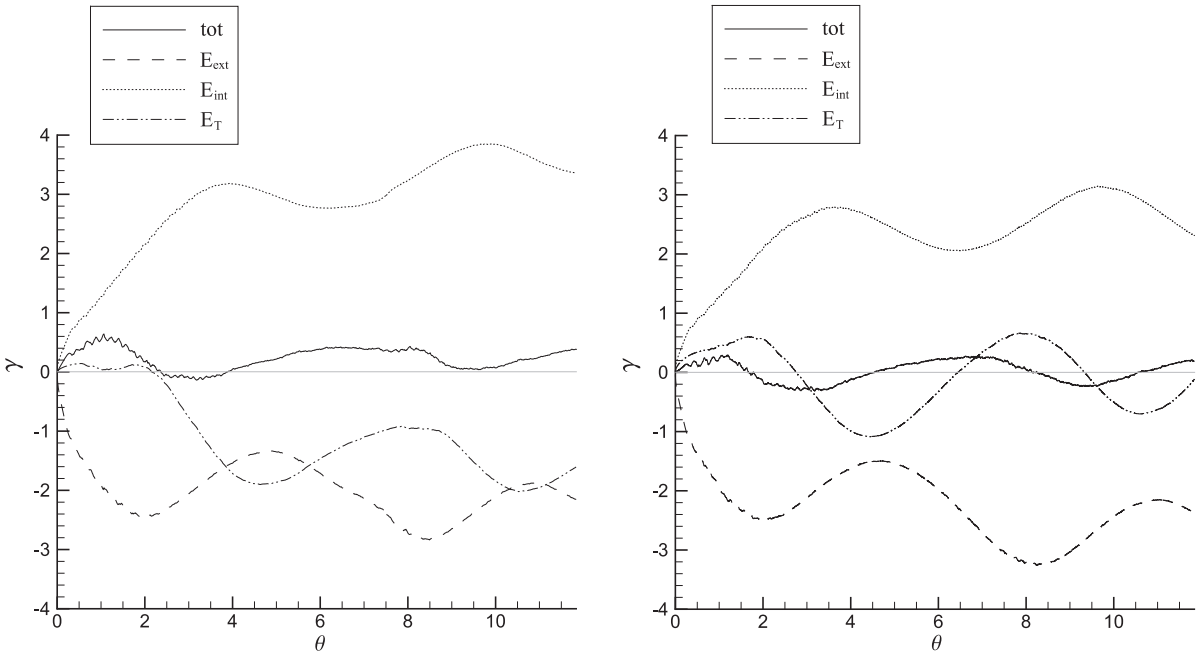

Figure 3.7. On the left-hand-side, evolution of the circulation for the rotating blade $q_\infty/\Omega R = 1/5$, $l/R = 1/2$. On the right-hand-side, evolution of the circulation for a still profile which experiences the same envelope of the relative velocity.

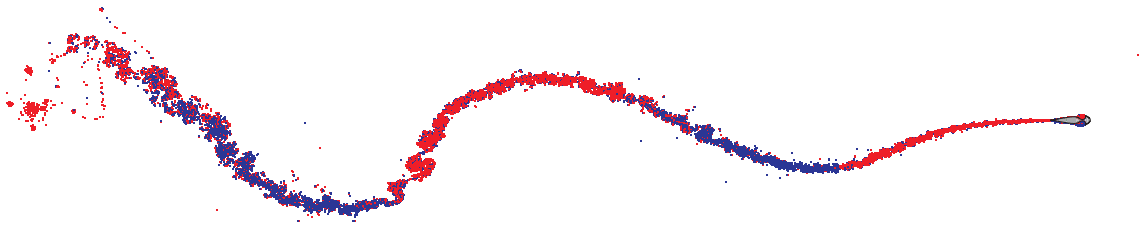

Figure 3.8. Wake pattern for a non rotating motion with same envelope of the relative velocity.

model is inviscid and does not take into account the incidental secondary separations, it allows the investigation of the physical vortex shedding phenomena. The Kutta condition is able to model the main viscous effect causing the flow separation, and the blob-vortex method represents an high order discrete approximation of the inviscid unsteady vortex wake (see references cited in 3.1.1).

In figure 3.7 the history of the circulation is illustrated. In the picture on the

left-hand-side the integral in time of the circulations generated by the internal, external and trailing edge are presented *versus* the blade angular position $\theta = \Omega t$. By applying the Kelvin theorem, the circulation around the blade results as the opposite of the sum of the circulations of the wake vortices; in this figure it is represented by the solid line. In spite of the symmetrical kinematics of the relative velocity described by the hodograph plane 3, the blade circulation shows a non null value with a positive average. Indeed, the motion of the blade is circular and, owing to the wake effect, the internal side of the blade differently acts from the external one.

In the picture on the right-hand-side of figure 3.7, we shown the evolution of the circulation for the profile involved in another motion but with the same envelope of the relative velocity. In this motion, the frame of reference is galileian and is fixed on the profile; in other terms, the profile does not move and the relative velocity 'seen' by the profile is equal to the absolute velocity. The absolute velocity corresponds to the upstream velocity, which varies with time. In particular, the time history of the upstream velocity is chosen so that it follows the same evolution of the relative velocity experienced by the blade section in the simulation represented in figure 3.4.

The aim of this test is to compare two kinds of motion characterized by a different flow dynamics but with the same kinematics of the relative velocity. In the case of the rotating blade, illustrated in figure 3.4 and on the left-hand-side of figure 3.7, the time evolution of the circulation shows that a variable lift with a non null average is exerted on the blade profile, that is, on the average, the mechanical power on the shaft is non null. In the case of the still profile, which whose the wake pattern is displayed in figure 3.8, the history of the circulation around the body, i.e. the lift, is periodic and its average value is approximately null (see the right-hand-side of figure 3.7). This result is coherent with the fact that the profile does not move and the upstream velocity is periodic.

3.1.3 Vortex wake past a two-elements airfoil

The study of the vortex motion in a region with a double connection is relevant to several problems in aerodynamics and hydrodynamics, such as the flow past multiple airfoils and the sea motion past islands. The theory of such kind of flows takes up several references in literature, see, for instance Marshall & McDonald (2004), [34], (2005) [35] and Crowdy & Marshall (2005) [20]. The vortex dynamics in such a problem is the preliminary subject of the investigation of the flow past a two-bladed vertical axis turbine.

We studied the transient flow motion past an airfoil equipped with a flap, initially at rest. The matter here presented is suitably developed for the two-bladed vertical axis turbine case by Ottino (2008) [48].

Following the study of Ferrari (1930) [23] of the analytical solution of the potential flow past a biplane section, the blob vortex method presented in 3.1.1 and applied in 3.1.2 for a domain with a single connection, is here devised for a doubly connected case.

With the aim of presenting an example, a suitable conformal mapping sequence is practiced in order to map two circles on the ν-plane onto an airfoil with flap in the physical z-plane. The image of the airfoil is defined as main circle (m), while the image of the flap is the secondary circle (s). In addition, in order to describe the flow field by means of the blob vortex method, a second mapping is needed: the outer region of the two circles in the ν-plane is transformed into a rectangle on the final χ-plane. More details are reported in appendix A.1.4.

As devised in [23], the complex velocity $\mathrm{d}w/\mathrm{d}\chi$ in the χ-plane (figure 3.9) must have a second order pole to represent the wind velocity and first order poles to represent the vortex singularities. On the χ-plane, the impermeability condition of the solid boundaries have to be imposed through infinite reflections referred to the vertical sides of the rectangle. Since the conformal mapping is periodic as compared to the horizontal limits of the rectangle, the infinite reflections have to be imposed with the horizontal boundaries as well. Therefore, the complex velocity has to be determined by a doubly periodic function (see, for instance, [70]), with the real semiperiod $\omega = a + b$ and the imaginary semiperiod $\omega' = \mathrm{i}\pi$. Now let us

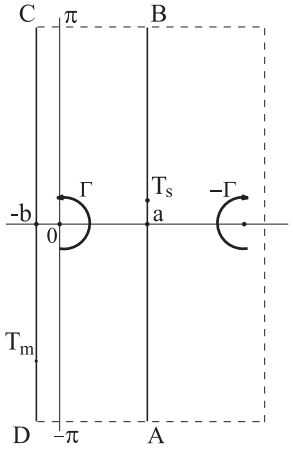

Figure 3.9. χ-plane.

describe the asymptotic solution for the steady flow, where the vortex shedding at the beginning is terminated and the circulation around two airfoils $-\Gamma$ is equivalent to the opposite circulation at infinity Γ. In this case, the flow field implies that the complex velocity can have point vortex only at $\chi = 0$ and $\chi = 2a$. According to the

double periodicity of the χ-plane, the complex velocity can be defined by means of the Weierstrass elliptic functions, that is

$$\frac{\mathrm{d}w}{\mathrm{d}\chi} = -[Q^*_\infty \wp(\chi) - Q_\infty \wp(\chi - 2a)] + \frac{\Gamma}{2\pi \mathrm{i}}[\zeta(\chi) - \zeta(\chi - 2a)] + \mathrm{i}\kappa \tag{3.9}$$

where $\wp$ and ζ represent a first-order and second-order pole, respectively. The constant $\kappa \in \mathbb{R}^1$, according to the theory of the elliptic functions, is introduced, since two elliptic functions characterized by the same poles only differ by a constant.

By taking into account the relations $\mathrm{d}\zeta(\chi)/\mathrm{d}\chi = -\wp(\chi)$, $\frac{\mathrm{d}}{\mathrm{d}\chi}\log\sigma(\chi) = \zeta(\chi)$ and integrating the above equation, the complex potential becomes

$$w = Q^*_\infty \zeta(\chi) - Q_\infty \zeta(\chi - 2a) + \frac{\Gamma}{2\pi \mathrm{i}} \log \frac{\sigma(\chi)}{\sigma(\chi - 2a)} + \mathrm{i}\kappa\chi, \tag{3.10}$$

where Q^*_∞ can be determined by the complex velocity at infinity in the z-plane (see for instance the Sec. 3.1.2), that is

$$Q^*_\infty = -2q^*_\infty \frac{c(1 - z_c)\mathrm{e}^{-\mathrm{i}\beta}}{\tau_s \tau_m} \frac{\lambda_T - \lambda_N + 1/\lambda^*_T - 1/\lambda^*_N}{\nu_T - \nu_N + 1/\nu^*_T - 1/\nu^*_N}. \tag{3.11}$$

The equation 3.9 is defined when Γ and κ are determined. By fixing the Kutta condition at the two trailing edges T_m, T_s and solving the linear system, the flow field is determined. Following 3.1.2, the Kutta condition can be enforced by

$$\left(\frac{\mathrm{d}w}{\mathrm{d}\chi}\right)_{\chi_{T_m}} = 0, \quad \left(\frac{\mathrm{d}w}{\mathrm{d}\chi}\right)_{\chi_{T_s}} = 0. \tag{3.12}$$

If $w = \phi + \mathrm{i}\,\psi$, where ϕ is the velocity potential function and ψ is the stream function, then $\gamma_m = \mathrm{Re}(w_C - w_D)$, $\gamma_s = \mathrm{Re}(w_A - w_B)$ are the circulations around the main and the secondary airfoils, the total circulation around the whole airfoil with flap is $(\gamma_m + \gamma_s) = -\Gamma$. By introducing the potential 3.10 and taking into account the properties of the elliptic functions $\zeta(\chi + 2\omega') = \zeta(\chi) + 2\eta'$ and $\log\sigma(\chi + 2\omega') = \log\sigma(\chi) + 2\eta'\chi$, the circulations around the airfoils are

$$\gamma_m = -4\mathrm{i}\eta' \left[\mathrm{Im}\left(Q_\infty + \frac{\Gamma a}{2\pi}\right)\right] - 2\pi\kappa, \quad \gamma_s = -\Gamma - \gamma_m, \tag{3.13}$$

where $\eta' = \zeta(\omega')$.

Now the transient that follows the impulsive starting of the double airfoil is studied. The asymptotic behaviour of the transient flow has to tend to the above steady solution. The unsteady rotational flow field generated by the starting can

be modelled by the blob vortex method discussed in section 3.1.1. In the following computation, the choice of the numerical parameters has been carried out by taking into account the prescriptions discussed in the previous section. At the initial time, the flow is at rest and the total circulation is null. Once the motion is generated, the vorticity begins being released and, by the Kelvin's circulation theorem $\mathrm{d}\Gamma/\mathrm{d}t = 0$, the total circulation is conserved.

Following the discrete approximation of the vorticity field, the complex velocity on the transformed χ-plane is defined by

$$\begin{aligned}\frac{\mathrm{d}w}{\mathrm{d}\chi} = &- \left[Q^*_\infty \wp(\chi) - Q_\infty \wp(\chi - 2a)\right] + \frac{1}{2\pi \mathrm{i}} \sum_{j_m=1}^{N} \gamma_{j_m} \left[\zeta\left(\chi - \chi_{j_m}\right) - \zeta\left(\chi + \chi^*_{j_m} - 2a\right)\right] \\ &+ \frac{1}{2\pi \mathrm{i}} \sum_{j_s=1}^{N} \gamma_{j_s} \left[\zeta\left(\chi - \chi_{j_s}\right) - \zeta\left(\chi + \chi^*_{j_s} - 2a\right)\right] + \mathrm{i}\kappa(t)\end{aligned} \tag{3.14}$$

and by integration the complex potential is

$$\begin{aligned}w = &Q^*_\infty \zeta(\chi) - Q_\infty \zeta(\chi - 2a) + \frac{1}{2\pi \mathrm{i}} \sum_{j_m=1}^{N} \gamma_{j_m} \log \frac{\sigma\left(\chi - \chi_{j_m}\right)}{\sigma\left(\chi + \chi^*_{j_m} - 2a\right)} \\ &\frac{1}{2\pi \mathrm{i}} \sum_{j_s=1}^{N} \gamma_{j_s} \log \frac{\sigma\left(\chi - \chi_{j_s}\right)}{\sigma\left(\chi + \chi^*_{j_s} - 2a\right)} + \mathrm{i}\kappa(t)\chi,\end{aligned} \tag{3.15}$$

where the subscripts m, s indicate the vortices shed by the main and secondary airfoils, N is the number of the released vortex couples , $\chi_{j_{m,s}}$ are their locations and $\kappa(t) \in \mathbb{R}^1$ uniquely defines the elliptic function that, for now, it is unknown. This function can be established by the Kelvin's circulation theorem, that is, the physical requirement that the sum of the bound and shed circulations past each body must remain constant.

Therefore the sum of the bound circulation and shed circulation has to be null for each airfoil, that is, $\gamma_m + \sum \gamma_{j_m} = 0$ and $\gamma_s + \sum \gamma_{j_s} = 0$. Referring to figure 3.9, by integration around two airfoils

$$\mathrm{Re}\left(\oint \frac{\mathrm{d}w}{\mathrm{d}\chi}\mathrm{d}\chi\right) = -\left(w_C - w_D\right) - \left(w_A - w_B\right) = \sum_{j_m=1, j_s=1}^{N} \left(\gamma_{j_m} + \gamma_{j_s}\right) \tag{3.16}$$

and by integration around each airfoil

$$\left(w_C - w_D\right) = \gamma_m, \quad \left(w_A - w_B\right) = \gamma_s. \tag{3.17}$$

One of the two 3.17 can be adopted to compute the function $\kappa(t)$, that is we can enforce

$$(w_C - w_D) = -\sum_{j_m}^{N} \gamma_{j_m}, \quad \text{or} \quad (w_A - w_B) = -\sum_{j_s}^{N} \gamma_{j_s}. \tag{3.18}$$

Considering the presence of the branch cuts between the point singularities at $\chi_{j_{m,s}}$ and $2a - \chi^*_{j_{m,s}}$, it is better to employ the first of the equations 3.18 in order to compute $\kappa(t)$. By using the above quasi-periodicity properties of the Weierstrass elliptic functions we obtain

$$\kappa(t) = \frac{1}{2\pi} \left\{ \sum_{j_m=1}^{N} \gamma_{j_m} + 2\frac{\eta'}{\mathrm{i}\pi} \sum_{j_{m,s}}^{2N} \gamma_{j_{m,s}} \left[a - \mathrm{Re}\left(\chi_{j_{m,s}}\right) \right] - 4\mathrm{i}\eta' \mathrm{Im}\left(Q_\infty\right) \right\}, \tag{3.19}$$

where the dependence on time of κ is hidden in the motion of the point singularities, located in $\chi_{j_{m,s}}(t)$.

Figure 3.10. Wake pattern at $t = 0.3$ and $t = 0.7$.

In the blob vortex method, the Kutta condition is imposed when the vortex singularities are shed, that is, the two equations $(\mathrm{d}w/\mathrm{d}\chi)_{\chi_{T_m}} = 0$ and $(\mathrm{d}w/\mathrm{d}\chi)_{\chi_{T_s}} = 0$ have to be set. At the same time, the equation 3.19 has to be imposed; therefore, these three equations establish a 3×3 linear system which is solved at each vortex generation, where the unknowns are κ, γ_{N_m}, γ_{N_s}.

The vortex advection is done by integrating in time the vortex velocities on the transformed χ-plane and then on mapping the vortex locations on the physical plane z-plane, as discussed in section 3.1.2. According to the Routh rule, the mapped vortex velocity is similar to 3.8, that is

$$\dot{\chi^*_j} = \left(\chi'^*_j - \frac{\gamma_j}{4\pi\mathrm{i}} \frac{\mathrm{d}^2 z/\mathrm{d}\chi^2}{\mathrm{d}z/\mathrm{d}\chi} \right) / J, \tag{3.20}$$

where J is the mapping Jacobian $J = |\mathrm{d}z/\mathrm{d}\chi|^2$ and χ'^*_j can be expressed by through the equation 3.7, that is

$$\begin{aligned} \chi'^*_j = &-[Q^*_\infty \wp(\chi_j) - Q_\infty \wp(\chi_j - 2a)] \\ &+ \frac{1}{2\pi\mathrm{i}} \left[\sum_{n=1, n\neq j}^{2N} \gamma_n \zeta(\chi_j - \chi_n) - \sum_{n=1}^{2N} \gamma_n \zeta(\chi_j + \chi^*_n - 2a) \right] + \mathrm{i}\kappa(t). \end{aligned} \tag{3.21}$$

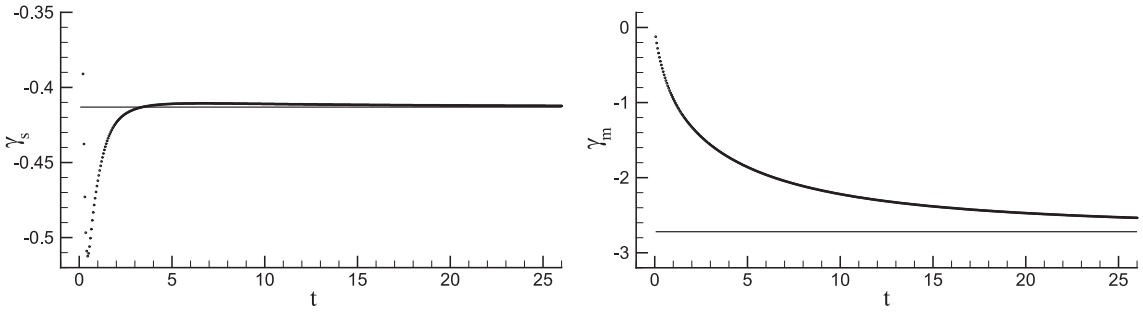

Figure 3.11. Time evolution of the circulation around the secondary element (left) and the main element (right).

A simulation of a transient flow has been computed for the same flow whose asymptotic steady state was computed above. The main goal of the simulation of the flow past an impulsively started double airfoil, is to reach the steady state as the limit of the time dependent solution. In other terms, this test represents a validation of the numerical integration of the velocities, which is performed to compute the vortex trajectories. The figure 3.10 illustrates two snapshots of the initial rolling up of the wakes released by the trailing edges of the two airfoils at angle of incidence $\alpha = 5°$. The time history of the circulations around the airfoils is presented in figure 3.11, where it is shown how the circulations asymptotically tend to the stationary values.

3.1.4 Low order model for the two-blade turbine

In this section a low order mathematical model of two-dimensional unsteady flow is addressed in order to describe the vortex wake past a vertical axis turbine. High order simulations of such kind of flow through a blob vortex method have been performed by Ottino in [48].

In this analysis the flow field is defined by a complex potential that takes into consideration the doubly connected domain, as in 3.1.3, and the boundary condition for moving bodies, as devised in [41]. The advection of the vortex singularities is carried out by means of the discrete vortex method proposed by Clements (1973) [13] (for more details see the sections 3.1.1, 3.1.2 and 3.1.3).

In the blob vortex model the vortex shedding is represented by vortex singularities with constant strength. The motion of the vortex is described by a *local* velocity that is the complex velocity at the vortex location without the self-induced contribution, and the Routh's correction is introduced when the velocity is evaluated on the mapped plane. When a vortex is generated, its circulation is once and for all

determined by enforcing the Kutta condition at the sharp edges and the vortex is released if its intensity is high enough. At the succeeding time-step, the vortex moves and the Kutta condition is not respected anymore until a new vortex is generated. The choice of the release time is discussed in section 3.1.1 and generally depends on the simulation time.

This approach represents an high-order model for the incompressible Euler equations. Since the number of the vortex singularities increases at each generation step, the computational cost is an important drawback of this model. On the other hand, a complete investigation of the performances of a vertical axis turbine would require a large amount of simulation cycles, by varying the design parameters, such as the chord-radius ratio c/R, the working ratio $q_\infty/\Omega R$ and the cavity shape in the case of a trapping vortex blade section.

A low-order mathematical model that describes the separation in the presence of sharp edges is now taken into account. We considered a technique where the circulation of the discrete vortex arising close to a cusp is time dependent, that is the nascent point vortex is connected to the edge by a *feeding* sheet. The discrete-vortex/feeding-sheet combination allows to model a continuous vortex sheet shed by the sharp edge by means of a reduced number of parameters.

Brown & Michael (1954) [8] argued that, if the point vortex with variable intesity is advected by the local vortex velocity, the joint system point vortex/feeding sheet experiences a force. Referring to the illustrations by Peters (1993) [50], the figure 3.12 shows a sketch of a feeding sheet that connects the point vortex with variable strength V and the sharp edge T. The mathematical representation of the feeding vortex sheet is a branch cut due to the logarithmic singularity representing the vortex. We consider the unsteady Bernoulli's equation for an irrotational flow (see **??**) $p+\rho\frac{\partial\phi}{\partial t}+V+\frac{1}{2}\rho q^2=p^0$, where ϕ is the velocity potential and V is the potential of an external conservative force. Since the velocity across the sheet is continuous, if we enforce the Bernoulli's equation at two limit points of the path l, the pressure difference acting on the line connecting the edge to the point vortex is determined. This static pressure jump is uniform along the sheet and is proportional to the rate of the circulation. As reported in [50], the pressure force can be expressed by

$$F_p = \mathrm{i}\rho\dot{\gamma}_V\left(z_V - z_T\right) \tag{3.22}$$

where ρ is the fluid density. In [8] a Magnus force F_M experienced by the point vortex is suggested such that the system is force-free, that is

$$F_M = -\mathrm{i}\rho\gamma_V\left(\dot{z}_V - z'_V\right) \tag{3.23}$$

where z'_V is the local velocity. The force balance yields the following equation that

governs the motion of a variable strength point vortex

$$\dot{z}_V = z'_V - \frac{\dot{\gamma_V}}{\gamma_V}\left(z_V - z_T\right), \tag{3.24}$$

where the last term is the so-called Brown & Michael's correction term. This force-free reduced order model has been adopted in literature in discrete vortex methods for predicting the loads due to the unsteady separation past bluff bodies or wings. On the other hand, this model is able to balance the forces but let a spurious moment to be introduced, as the figure 3.12 shows. This drawback is overcome in Howe (1996) [32], where another vortex sheet modelization based on a modified Brown & Michael's equation is devised. A wide explanation of this model, references, validations and comparisons with other reduced techniques are reported in [50], Cortelezzi (1996) [16] and [32].

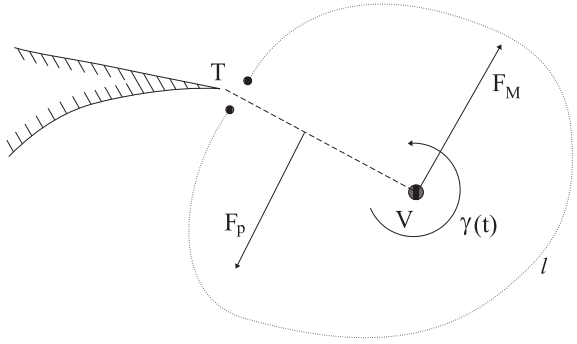

Figure 3.12. Feeding sheet (dashed line) between the sharp edge and the point vortex.

The vortex wake past the vertical axis wind turbine is now modelled by means of the Brown & Michael equation 3.24. The two blade sections are obtained by a chain of conformal mappings that maps the outer region of two profiles, identical and symmetrycal to the axis, onto an annulus similar to the μ-plane obtained in A.1.4 for the airfoil with a flap. Finally, the flow region is mapped onto a rectangle on the χ-plane (figure 3.13). The blades are indicated with the subscripts m, s and are related to the interior and the exterior circles of the μ-plane annulus, respectively.

As discussed in [48], the trailing edges are defined by $\chi_{T,m}$, $\chi_{T,s}$, while the locations of the new point vortices are $\chi_{V,m}$, $\chi_{V,s}$ where m,s denote the related generating airfoil. The subscript j indicates a free point vortex. Q_∞ is defined in the transformed plane χ-plane and represents the momentum of the doublet corresponding to the wind velocity in the physical z-plane. Following [48], the equation 3.14, which describes the vortex motion in a doubly connected domain, is modified by taking into account the moving boundaries, that is

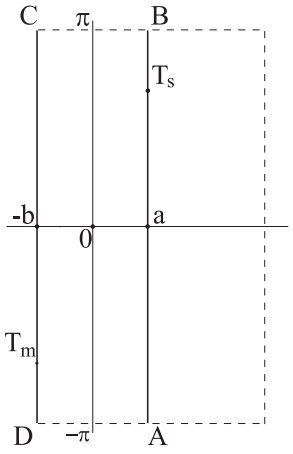

Figure 3.13. χ-plane.

$$\begin{aligned}\frac{\mathrm{d}w}{\mathrm{d}\chi} =& - Q^*_\infty \wp(\chi) + Q_\infty \wp(\chi+\omega) + \frac{\mathrm{d}w_2}{\mathrm{d}\chi} + \mathrm{i}\kappa \\ &+ \frac{1}{2\pi\mathrm{i}} \sum_{j=1}^{N-2} \gamma_j \left[\zeta(\chi-\chi_j) - \zeta(\chi+\chi_j^*-\omega)\right] \\ &+ \frac{1}{2\pi\mathrm{i}} \gamma_m \left[\zeta(\chi-\chi_{V,m}) - \zeta(\chi+\chi_{V,m}^*-\omega)\right] + \frac{1}{2\pi\mathrm{i}} \gamma_s \left[\zeta(\chi-\chi_{V,s}) - \zeta(\chi+\chi_{V,s}^*-\omega)\right]\end{aligned} \tag{3.25}$$

where $\eta = \zeta(\omega)$, $\eta' = \zeta(\omega')$ and N is total number of released vortices. The term w_2 is a series that does not add any singularities to the flow field, converges inside the annulus of the μ-plane and allows to define the boundary conditions for moving bodies. It is the version of the Laurent series with only negative exponents, discussed in section 3.1.2, for doubly connected domain.

In the Brown & Michael numerical model the circulation of a nascent vortex varies with time while it is advected by the flow field with the corrected velocity 3.24. As soon as the time derivative of the circulation becomes null, i.e. the intensity does not change anymore, the vortex is shed with the constant strength and advected with its local velocity. In addition, another vortex with variable strength is generated close to the sharp edge. When a new vortex is going to be created, its intensity increases and it is released only if the circulation threshold is reached.

Looking at the equation 3.25, the contribution of the variable strength vortices to the flow field is provided by the last two terms, where $\gamma_m = \gamma_m(t)$ and $\gamma_s = \gamma_s(t)$.

On the other hand, the vortices with constant intensities are represented by the summation.

As presented in [48], at each time-step, the Kutta condition and the Kelvin's theorem around a profile have to be enforced, such that γ_m,γ_s and κ are computed and the flow field is uniquely determined. The advection of the variable strength vortices needs to evaluate the time derivatives of the circulations $\dot{\gamma}_m$,$\dot{\gamma}_s$. A wide discussion and the mathematical derivations are reported in appendix A.2.2.

The heuristic choice of simulation parameters, such as release timing, location and marching time-step is coherent with the indications discussed in section 3.1.1. The absolute value of the generation threshold for the circulation is 0.001. In figure

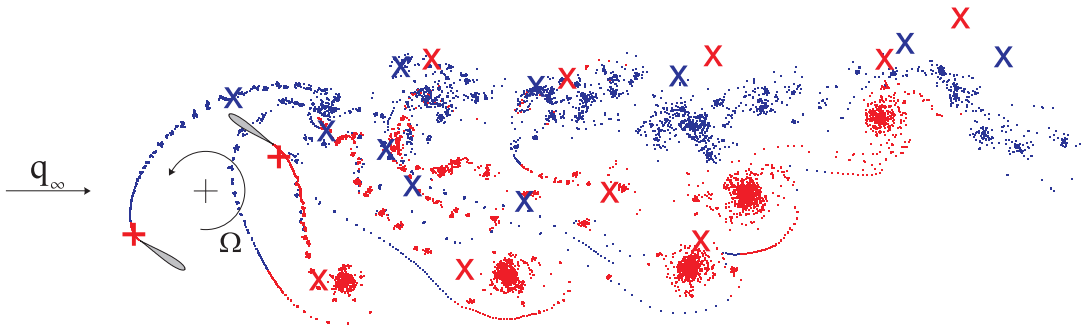

Figure 3.14. Wake pattern represented by the high-order model (dots) and the low-order model (crosses) at $t = 36$. The "+" close to the trailing edges indicate the variable intensity vortices.

3.14 we present a visualization of the wake issued by a turbine with the chord/radius ratio $c/R = 0.74$ and with the operating ratio $q_\infty/\Omega R = 0.88$.

In this picture the wake pattern computed by the reduced order model, marked by crosses, is compared to the solution computed by [48], marked by dots. The colour of the marks depends on the clockwise or counterclockwise spin. In the high-order model the wake consists in $N = 14200$ point vortices, while in the low-order model in $N = 20$. All the simulations have been performed on a distributed memory HP Linux cluster platform, equipped with 9 nodes bi-dual core AMD Opteron 2.2 GHz. The high-order simulation run on 12 processors and spent ≈ 180 hours of real time, while the low-order run on a single processor and spent ≈ 8 minutes. The saving of the computational resources and processor run-time represents the major advantage of the reduced-order model. The time history of the bound circulations is presented in figure 3.15. The solid lines represent the low order simulation and the dash-dotted line the high order simulation. The sub-scripts m,s indicate the blade section around the circulation has been computed.

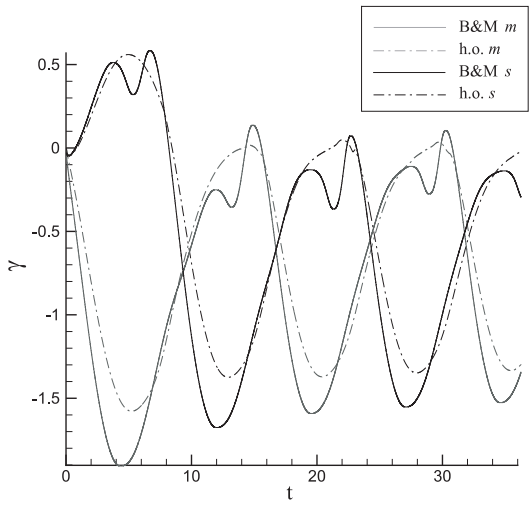

Figure 3.15. Time history of the blade circulations computed by the high-order model (h.o.) and the low-order model (B & M).

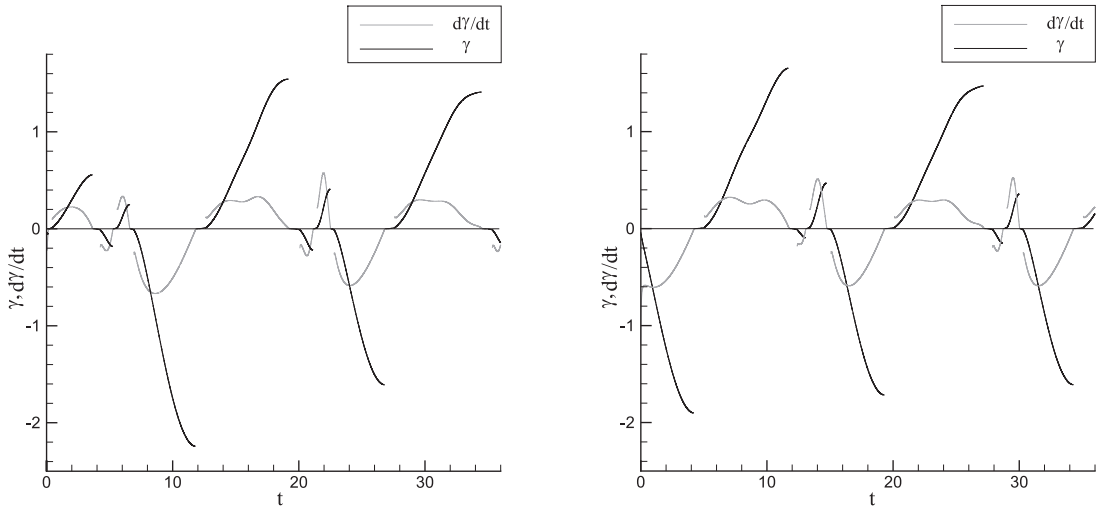

Figure 3.16. Time history of the circulation and of its time derivative for the variable intensity vortices. The left-hand side and right-hand side pictures are pertinent to the vortices shed by the m and s blade, respectively.

The time history of the blade circulations computed by means of the reduced-order model shows an agreement with the results of the high-order model, in terms of phase, average values and amplitudes. An estimation of forces and torque through

the impulse theory, discussed in section 3.1.6, represents another meaningful point in order to compare the proposed models. This problem is the subject of an ongoing research activity.

In figure 3.16 the time history of the circulation and of the circulation time derivative for the variable-strength point vortices m,s is displayed. When the time derivative of the circulation tends to zero, i.e. the strength of the vortex is going to be constant, then the vortex is released and a new vortex is generated close to the related trailing edge. As soon as a constant intensity vortex is released, the nascent vortex has an intensity lower than the threshold and is not advected until the circulation increases enough.

We presented here a low-order model which allows to simulate the inviscid unsteady wake past a two-blades VAT with a minimum computational cost. This method represents an efficient tool for the preliminary design of such kind of machinery.

3.1.5 Forces and torque

The rigorous evaluation of the performances from the results, as given by the blob vortex method, is not a simple task. It consists of computing the dynamical effects of a rotational unsteady incompressible flow in a system of moving bodies. Many contributions concerning this topic can be found in the literature. See, for instance, Quartapelle & Napolitano (1982) [56], Wells (1998)[75], Pan & Chew (2002)[49], Graziani & Bassanini (2002) [31], Protas (2007) [55] and references therein.

There are two methods that can be considered for deducing the dynamical actions from the simulations performed with a blob vortex method. The first method is based on integrating the pressure on the body's solid walls by means of the unsteady Bernoulli equation. The Blasius' formulas discussed in [41] could be used for this purpose. The main drawback of applying this approach in a blob vortex method is determined by the strong noise that affects the pressure signal close to the solid wall as a consequence of the vorticity concentrated in vortex singularities. The second method is based on determining the dynamical actions by means of the time derivatives of the linear and angular impulse of a fluid system (see, for instance, [62]). This approach is most suitable for the present flow simulation and it is the way that we intend to take into account. Subsequently, a general survey of the evaluation of forces that the fluid exerts on a system of bodies moving rigidly is presented.

The evaluation of the time dependent forces in viscous incompressible flow without computing the pressure field is widely discussed in literature. Some references can be found in Quartapelle & Napolitano (1982) [56], Noca *et al.* (1999) [46], Pan & Chew (2002) [49] and Protas (2007) [55]. In particular in the seminal work [56] the pressure variable is eliminated from the force equation at the cost of an additional variable, that is a solution of a Laplace problem. Noca *et al.* (1999) present some closed formulations of the incompressible Navier Stokes equations, such that the evaluation of the unsteady forces exerted on a moving body requires only the information of the velocity field and its derivatives in a fluid region that includes the body. These expressions are particularly popular both in the experimental techniques, such as the Digital Particle Image Velocimetry (DPIV), and in the numerical approaches, such as the $\psi - \omega$ methods, where the pressure field is not explicitly determined.

Following [46], let us consider a solid moving body surrounded by an arbitrary time dependent control volume $V(t)$, that is defined by the external surface $S(t)$, the internal body surface $S_b(t)$ and the branch-cut surfaces $S_u(t)$ (figure 3.17). The fluid dynamic force exerted by the flow on the body can be evaluated by the momentum

equation in integral form, that is

$$\begin{aligned}\mathbf{F} = &- \frac{\mathrm{d}}{\mathrm{d}t}\int_{V(t)} \mathbf{u}\ \mathrm{d}V \\ &+ \oint_{S(t)} \mathbf{n}\cdot[-p\,\mathbf{I} - (\mathbf{u}-\mathbf{u}_S)\mathbf{u} + \mathbf{T}]\ \mathrm{d}S \\ &- \oint_{S_b(t)} \mathbf{n}\cdot(\mathbf{u}-\mathbf{u}_S)\mathbf{u}\ \mathrm{d}S,\end{aligned} \tag{3.26}$$

where $\mathbf{n}$ is the unit normal vector pointed outward, $\mathbf{u}$ is the flow velocity, $\mathbf{u}_S$ is the boundary velocity, i.e. internal body surface velocity, p is the pressure, the density is unit and is omitted, $\mathbf{I}$ is the unit tensor, $\mathbf{T}$ the incompressible viscous stress tensor $\mathbf{T} = \mu(\nabla\mathbf{u} + \nabla\mathbf{u}^T)$ and μ is the dynamic viscosity. In addition, the moment $\mathbf{M}_O$ of

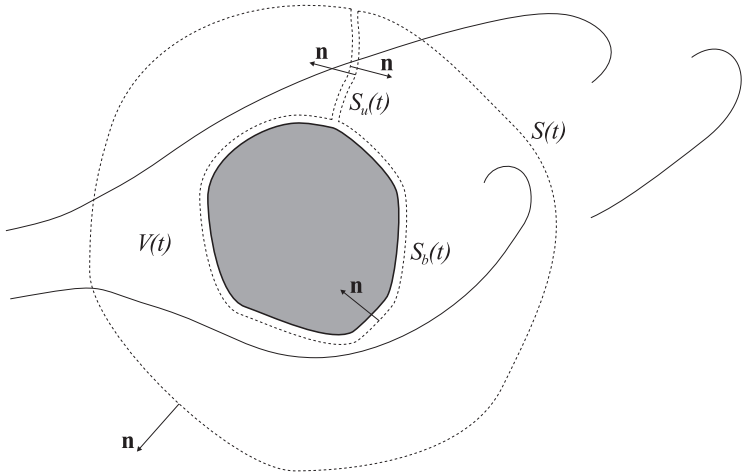

Figure 3.17. Sketch of the control surfaces and volume enclosing a moving body immersed in a free stream.

the force $\mathbf{F}$ referred to the origin O of the frame of reference is

$$\begin{aligned}\mathbf{M}_O = &- \frac{\mathrm{d}}{\mathrm{d}t}\int_{V(t)} \mathbf{x}\wedge\mathbf{u}\ \mathrm{d}V \\ &+ \oint_{S(t)} \mathbf{x}\wedge\{\mathbf{n}\cdot[-p\,\mathbf{I} - (\mathbf{u}-\mathbf{u}_S)\mathbf{u} + \mathbf{T}]\}\ \mathrm{d}S \\ &- \oint_{S_b(t)} \mathbf{x}\wedge\{\mathbf{n}\cdot(\mathbf{u}-\mathbf{u}_S)\mathbf{u}\}\ \mathrm{d}S,\end{aligned} \tag{3.27}$$

By using some vectorial identities and basic transformations, the equation 3.26 is modified by Noca *et al.* in three formulations that only require only the knowledge of

the velocity and its derivatives in $V(t)$. These three expressions have been validated through some numerical and experimental applications. Referring to the terminology proposed in [46], in section 3.2.4 we took into consideration the so-called 'impulse' equation and 'momentum' equation.

The 'impulse equation' is the extension of the definition of hydrodynamical impulse to a viscous flow, proposed by Saffman (1992) [62]. Indicating with $N = 2$ or $N = 3$ the 2D or 3D flow, the equation is

$$\begin{aligned}\mathbf{F} = &-\frac{1}{N-1}\frac{\mathrm{d}}{\mathrm{d}t}\int_{V(t)} \mathbf{x}\wedge\boldsymbol{\omega}\ \mathrm{d}V \\ &+ \oint_{S(t)} \mathbf{n}\cdot\boldsymbol{\gamma}_{imp}\ \mathrm{d}S \\ &+ \frac{1}{N-1}\frac{\mathrm{d}}{\mathrm{d}t}\oint_{S_b(t)} \mathbf{x}\wedge(\mathbf{n}\wedge\mathbf{u})\ \mathrm{d}S - \oint_{S_b(t)} \mathbf{n}\cdot(\mathbf{u}-\mathbf{u}_S\mathbf{u})\ \mathrm{d}S,\end{aligned} \tag{3.28}$$

with

$$\begin{aligned}\boldsymbol{\gamma}_{imp} =& \frac{1}{2}u^2\mathbf{I} - \mathbf{u}\mathbf{u} - \frac{1}{N-1}(\mathbf{u}-\mathbf{u}_S)(\mathbf{x}\wedge\boldsymbol{\omega}) + \frac{1}{N-1}\boldsymbol{\omega}(\mathbf{x}\wedge\mathbf{u}) \\ &+ \frac{1}{N-1}\left[\mathbf{x}\cdot(\nabla\cdot\mathbf{T})\mathbf{I} - \mathbf{x}(\nabla\cdot\mathbf{T})\right] + \mathbf{T}.\end{aligned}$$

If we suppose that the flow at infinity is at rest, the body is substituted by a distribution of image vorticity, and the control volume $V(t)$ extends over the whole space including the body, the equation 3.28 expresses the well-known invariance of the hydrodynamical linear impulse, such that $\mathbf{F} = -\frac{1}{N-1}\frac{\mathrm{d}}{\mathrm{d}t}\mathbf{I}$ where $\mathbf{I}$ is the first moment of the vorticity evaluated on $V(t)$.

The 'momentum equation' is an equivalent expression that involves the same integrals as the equation 3.26, but does not require the pressure variable, namely

$$\begin{aligned}\mathbf{F} = &-\frac{\mathrm{d}}{\mathrm{d}t}\int_{V(t)} \mathbf{u}\ \mathrm{d}V \\ &+ \oint_{S(t)} \mathbf{n}\cdot\boldsymbol{\gamma}_{mom}\mathrm{d}S - \oint_{S_b(t)} \mathbf{n}\cdot(\mathbf{u}-\mathbf{u}_S)\mathbf{u}\ \mathrm{d}S,\end{aligned} \tag{3.29}$$

where

$$\begin{aligned}\boldsymbol{\gamma}_{mom} =& \frac{1}{2}u^2\mathbf{I} + (\mathbf{u}_S-\mathbf{u})\mathbf{u} - \frac{1}{N-1}\mathbf{u}(\mathbf{x}\wedge\boldsymbol{\omega}) + \frac{1}{N-1}\boldsymbol{\omega}(\mathbf{x}\wedge\mathbf{u}) \\ &- \frac{1}{N-1}\left[\left(\mathbf{x}\cdot\frac{\partial\mathbf{u}}{\partial t}\right)\mathbf{I} - \mathbf{x}\frac{\partial\mathbf{u}}{\partial t}\right] \\ &+ \frac{1}{N-1}\left[\mathbf{x}\cdot(\nabla\cdot\mathbf{T})\mathbf{I} - \mathbf{x}(\nabla\cdot\mathbf{T}) + \mathbf{T}\right].\end{aligned}$$

Now, we will focus on the evaluation of the forces and moments in the case of a control volume extending to infinity. Let us consider the flow field around a system of moving bodies immersed in a free stream with a constant velocity $\mathbf{q}_\infty$ at infinity. For sake of simplicity the frame of reference is Cartesian and the position is defined by $\mathbf{X}$. By means of a Galileian transformation $\mathbf{x} = \mathbf{X} - \mathbf{q}_\infty\, t$, a new frame of reference $\mathbf{x}$ can be introduced so that the infinity is at rest. A first trivial application of this transformation is reported in appendix A.2.5. In addition we supposed that the external forces vanish at infinity and the vorticity vanishes outside some finite regions.

By following [62] and with the aforesaid hypothesis, it is important to remark that at large distances the flow is irrotational, that is $\mathbf{u} = \nabla\phi$, where the velocity potential ϕ can be defined as the expansion

$$\phi = \sum_{n=0}^{\infty} \frac{a_n S_n(\theta,\lambda)}{r^{n+1}}.$$

$S_n(\theta,\lambda)$ are harmonic surfaces, (r,θ,λ) are spherical, polar coordinates and a_n are some real coefficents, which depend on the vorticity distribution. In the absence of sources or sinks, $a_0 = 0$ and the leading term goes with $1/r^2$. This hypothesis of decay of the velocity allows to annul the surface integrals on $S(t)$ in the equations 3.26 and 3.27, when the surface tends to infinity. Finally, the impermeability condition on the solid boundaries and the above consideration on the flow at the infinity permit to replace the equations 3.26 and 3.27 with the following expressions

$$\mathbf{F} = -\frac{\mathrm{d}}{\mathrm{d}t}\int_{V_\infty} \mathbf{u}\ \mathrm{d}V \tag{3.30}$$

$$\mathbf{M}_O = -\frac{\mathrm{d}}{\mathrm{d}t}\int_{V_\infty} \mathbf{x}\wedge\mathbf{u}\ \mathrm{d}V \tag{3.31}$$

where the integrals determine the momentum and the angular momentum of the whole flow field. Through the vectorial identity (see [62])

$$\int_V \mathbf{x}\wedge\nabla\wedge\mathbf{u}\ \mathrm{d}V = (N-1)\int_V \mathbf{u}\ \mathrm{d}V + \oint_S \mathbf{x}\wedge(\mathbf{n}\wedge\mathbf{u})\ \mathrm{d}S$$

the time derivative of the integral in the equation 3.30 becomes

$$\frac{\mathrm{d}}{\mathrm{d}t}\int_{V_\infty} \mathbf{u}\ \mathrm{d}V = \frac{1}{N-1}\frac{\mathrm{d}}{\mathrm{d}t}\int_{V_\infty} \mathbf{x}\wedge\boldsymbol{\omega}\ \mathrm{d}V + \frac{1}{N-1}\frac{\mathrm{d}}{\mathrm{d}t}\oint_{S_b(t)} \mathbf{x}\wedge(\mathbf{n}\wedge\mathbf{u})\ \mathrm{d}S. \tag{3.32}$$

This equation is meaningful because it expresses how the force exerted on a body is provided by two contributions: a volume integral, that includes the effects of the

wake and the other bodies' systems replaced by some image vorticity distributions (see [62]), and a surface integral. The surface integral represents the contribution, to the dynamical action, of a bound vorticity, that consists of a vortex sheet with the strength defined by the tangential component on the boundaries of the absolute velocity. In other terms, the body is replaced by a vortex dynamical equivalent and the whole system 'flow field + bodies' can be considered as a single fluid system.

Let us define the intensity of the bound vorticity as $\boldsymbol{\kappa} = \mathbf{n} \wedge \mathbf{u}$, with $\mathbf{n}$ pointed outward from the control surface, i.e. inward towards the solid body. The force is then determined by

$$\mathbf{F} = -\frac{\mathrm{d}}{\mathrm{d}t}\left[\frac{1}{N-1}\int_{V_\infty} \mathbf{x} \wedge \boldsymbol{\omega}\ \mathrm{d}V + \frac{1}{N-1}\oint_{S_b(t)} \mathbf{x} \wedge \boldsymbol{\kappa}\ \mathrm{d}S\right]. \tag{3.33}$$

The same approach can be applied to the moment equation 3.31. By replacing the volume integral in the right-hand side with the following identity (see [62])

$$\int_V \mathbf{x} \wedge \mathbf{u}\ \mathrm{d}V = -\frac{1}{2}\int_V r^2\boldsymbol{\omega}\ \mathrm{d}V - \frac{1}{2}\oint r^2(\mathbf{n} \wedge \mathbf{u})\ \mathrm{d}S \tag{3.34}$$

the moment equation becomes

$$\mathbf{M}_O = -\frac{\mathrm{d}}{\mathrm{d}t}\left[-\frac{1}{2}\int_{V_\infty} r^2\boldsymbol{\omega}\ \mathrm{d}V - \frac{1}{2}\oint_{S_b(t)} r^2\boldsymbol{\kappa}\ \mathrm{d}S\right]. \tag{3.35}$$

where $r^2 = \mathbf{x} \cdot \mathbf{x}$.

From the equations 3.33 and 3.35 the linear and angular hydrodynamical impulse can be deduced. They are two natural invariants of the flow and, by indicating with $\mathbf{I}$ the linear impulse and with $\mathbf{A}$ the angular impulse of the flow, we have $\mathbf{F} = -\mathrm{d}\mathbf{I}/\mathrm{d}t$ and $\mathbf{M}_O = -\mathrm{d}\mathbf{A}/\mathrm{d}t$. If there are no bodies within the flow field, no force and moment are exerted and the quantities $\mathbf{I}$ and $\mathbf{A}$ are conserved in time. As discussed above, the two impulses take into account of the 'wake' and the 'bound vorticity' contributions, therefore the invariants can be defined as $\mathbf{I} = \mathbf{I}_w + \mathbf{I}_{bv}$ and $\mathbf{A} = \mathbf{A}_w + \mathbf{A}_{bv}$. By comparing these expressions with the right-hand sides of both the equations 3.33 and 3.35, the following definitions easily can be found

$$\begin{aligned} \mathbf{I}_w &= \frac{1}{N-1}\int_{V_\infty} \mathbf{x} \wedge \boldsymbol{\omega}\ \mathrm{d}V, \quad \mathbf{I}_{bv} = \frac{1}{N-1}\oint_{S_b(t)} \mathbf{x} \wedge \boldsymbol{\kappa}\ \mathrm{d}S \\ \mathbf{A}_w &= -\frac{1}{2}\int_{V_\infty} r^2\boldsymbol{\omega}\ \mathrm{d}V, \qquad \mathbf{A}_{bv} = -\frac{1}{2}\oint_{S_b(t)} r^2\boldsymbol{\kappa}\ \mathrm{d}S. \end{aligned} \tag{3.36}$$

3.1.6 Performances evaluation

An approach devoted to the realistic evaluation of the turbine performance is now taken into account. The estimation of the forces and torque exerted on the turbine's

shaft can be efficiently carried out by means of the impulse theory discussed in the previous section.

As first consideration, a rough approximation of the forces could be attempted by assuming the flow as quasi-steady, that is, by applying the Joukowski theorem to the instantaneous blade circulation generated by the instantaneous asymptotic relative velocity assumed as steady. Since the unsteadiness is an intrinsic feature of such kind of flow field, as discussed in the introduction of chapter 3, this approach however is deceptive. This method is now presented.

Let us consider the one-blade turbine described in section 3.1.2. In figure 3.18, the trapped vortex blade circulation (solid line) is compared to the circulations the blade would experience if the flow were steady. In particular, the dotted line is related to a blade with trapped vortices, while the dash-dotted line is pertinent to a blade without trapped vortices. The actual unsteady circulation is very far from the steady ones and it does not allow for a realistic approximations of the performances on the basis of a quasi-steady estimation. It shows a much smaller amplitude and a different phase as a consequence of the transient nature of the flow and of the wake effect.

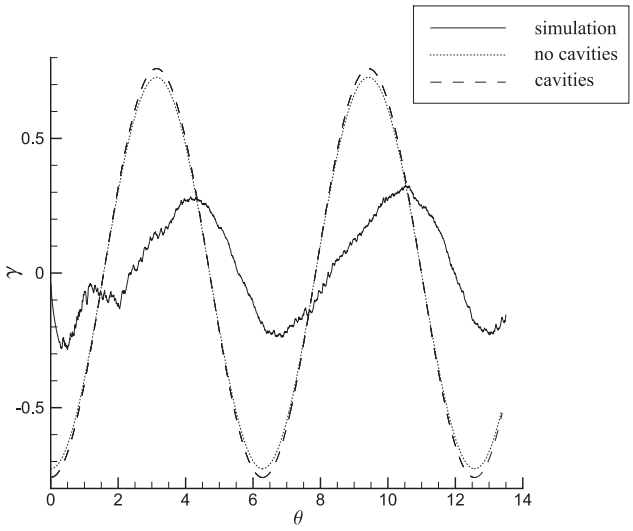

Figure 3.18. Single blade turbine $q_\infty/\Omega R$=0.2: steady and unsteady circulations *versus* blade angular position

The steady circulation past the blade with trapped vortices has been computed analytically by imposing the Kutta condition at the three edges of the blade for a given relative velocity at infinity. It allows to compute the circulation at infinity and the strength of the trapped vortices, which are assumed as point vortices located in

equilibrium position. The vortex equilibria result as being stable. The method used to determine the equilibrium positions of the trapped vortices and their stability is described in [77] and discussed in section 2.2.

The comparison between the steady circulations, with and without the trapped vortices, offers a clue on the effect of the trapped vortices. The amplitude of the circulation related to the blade with trapped vortices is slightly larger than that without trapped vortices, hence the effect of enhancing the turbine performances should be small. Therefore, the main outcome expected by the trapped vortices is the stall control rather than the perfomance improvement, which is however present.

It is important to remark that these assumptions need to be validated by the full unsteady model, and the effect of the cavities on the blade's performance would have be verified through the explicit estimation of the evolution in time of the loads.

With the hydrodynamical impulse theory, the unsteady loads exerted on the turbine can be evaluated. Let us take into consideration the 2D inviscid flow model pertinent to the blob vortex method presented in section 3.1.1. In a Cartesian frame of reference with versors $\mathbf{i}$, $\mathbf{j}$, $\mathbf{k}$ the relations 3.36 become

$$\begin{aligned} \mathbf{I}_w &= \int_{S_\infty} \omega\ \mathbf{x} \wedge \mathbf{k}\ \mathrm{d}S, \qquad & \mathbf{I}_{bv} &= \oint_B \kappa\ \mathbf{x} \wedge \mathbf{k}\ \mathrm{d}s \\ \mathbf{A}_w &= -\frac{1}{2} \int_{S_\infty} \omega\ r^2 \mathbf{k}\ \mathrm{d}V, & \mathbf{A}_{bv} &= -\frac{1}{2} \oint_B \kappa\ r^2 \mathbf{k}\ \mathrm{d}s, \end{aligned} \tag{3.37}$$

where S_∞ indicates the supports where the vorticity takes place, B is the solid boundary traced by the curvilinear coordinate s and $\kappa\mathbf{k} = \mathbf{n} \wedge \mathbf{u}$ is the bound vorticity. In the single-blade model presented in section 3.1.2, the blade section in the physical z-plane is mapped onto a unit circle in the transformed ζ-plane. The flow field was described through a complex potential $w = w(z(\zeta))$ in which the vorticity is modelled as some vortex singularities.

The frame of reference is fixed on the blade, *ergo*, by means of a Galileian transformation, we can compute the absolute velocity of the flow with the infinity at rest by subtracting the velocity of the stream. Indicating with $\mathbf{V}_{abs}$ the absolute velocity, we can write

$$\mathbf{V}^*_{abs} = \left(\frac{\mathrm{d}w}{\mathrm{d}\zeta}\ \frac{1}{\frac{\mathrm{d}z}{\mathrm{d}\zeta}} - q_\infty \mathrm{e}^{-\mathrm{i}\alpha} \right) \tag{3.38}$$

where $(\cdot)^*$ indicates the complex conjugate, $q_\infty \mathrm{e}^{\mathrm{i}\alpha}$ is the free stream velocity evaluated on the moving frame of reference in the physical plane. Now the bound vorticity distribution can be determined. In figure 3.19, a sketch of the body contour is illustrated. According with the notation adopted in the conformal mappings, the normal $\mathbf{n}$ is chosen outward form the wall and β is the angle evaluated in the physical plane.

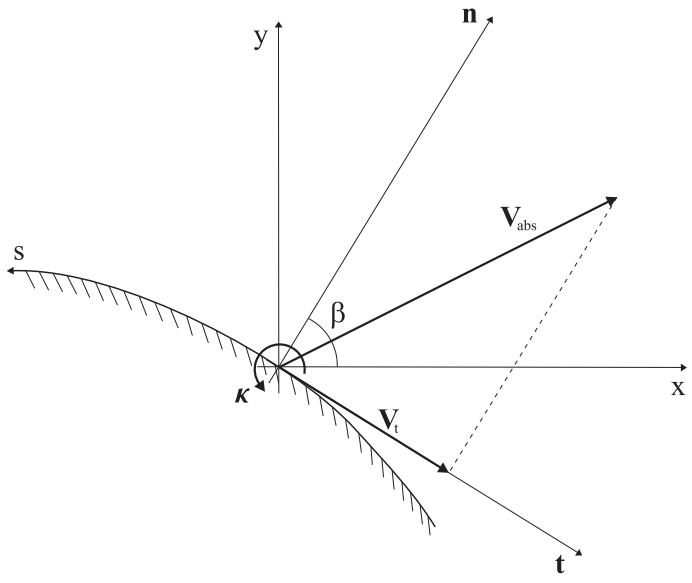

Figure 3.19. Bound vorticity evaluation

The basic property of conformal mappings of preserving the angles $\frac{\mathrm{d}z}{\mathrm{d}\zeta} = \left|\frac{\mathrm{d}z}{\mathrm{d}\zeta}\right| \, \mathrm{e}^{\mathrm{i}(\beta-\phi)}$, allows to determine β depending on the angle between the normal and the body ϕ on the transformed plane.

The tangential component of the absolute velocity is $\mathbf{V}_t = \mathrm{Im}\left[\mathbf{V}^*_{abs}\mathrm{e}^{\mathrm{i}\beta}\right]$. Finally, taking into account of the bound vorticity definition, we can write

$$\kappa = -\mathrm{Im}\left[\left(\frac{\mathrm{d}w}{\mathrm{d}\zeta} - q_\infty \mathrm{e}^{-\mathrm{i}\alpha}\frac{\mathrm{d}z}{\mathrm{d}\zeta}\right)\frac{\mathrm{e}^{\mathrm{i}\phi}}{\left|\frac{\mathrm{d}z}{\mathrm{d}\zeta}\right|}\right] \tag{3.39}$$

The relations 3.37 can be easily adapted to the blob vortex method. If N is the number of the free point vortices immersed in the flow field, the contribution of the wake to the impulses is expressed by the following summations

$$I^x_w = \sum_{i=1}^{N}\gamma_i \; y_i, \;\; I^y_w = -\sum_{i=1}^{N}\gamma_i \; x_i, \;\; A_w = -\frac{1}{2}\sum_{i=1}^{N}\gamma_i \left(x_i^2 + y_i^2\right). \tag{3.40}$$

The bound vorticity contribution is evaluated by means of an integral on the body contour computed on the mapped plane. Being $s = z(\mathrm{e}^{\mathrm{i}\phi})$ and substituting $\mathrm{d}s = \left|\frac{\mathrm{d}z}{\mathrm{d}\zeta}\right| \, \mathrm{d}\phi$ in the line integrals of equations 3.37, the impulses related to the bound

vorticity are

$$
\begin{aligned}
I_{bv}^{x} &= -\int_{0}^{2\pi} \mathrm{Im}\left[\left(\frac{\mathrm{d}w}{\mathrm{d}\zeta} - q_{\infty}\mathrm{e}^{-\mathrm{i}\alpha}\frac{\mathrm{d}z}{\mathrm{d}\zeta}\right)\mathrm{e}^{\mathrm{i}\phi}\right]\; y_B(\phi)\;\mathrm{d}\phi \\
I_{bv}^{y} &= \int_{0}^{2\pi} \mathrm{Im}\left[\left(\frac{\mathrm{d}w}{\mathrm{d}\zeta} - q_{\infty}\mathrm{e}^{-\mathrm{i}\alpha}\frac{\mathrm{d}z}{\mathrm{d}\zeta}\right)\mathrm{e}^{\mathrm{i}\phi}\right]\; x_B(\phi)\;\mathrm{d}\phi \\
A_{bv} &= \frac{1}{2}\int_{0}^{2\pi} \mathrm{Im}\left[\left(\frac{\mathrm{d}w}{\mathrm{d}\zeta} - q_{\infty}\mathrm{e}^{-\mathrm{i}\alpha}\frac{\mathrm{d}z}{\mathrm{d}\zeta}\right)\mathrm{e}^{\mathrm{i}\phi}\right]\; (x_B(\phi)^2 + y_B(\phi)^2)\;\mathrm{d}\phi
\end{aligned}
\tag{3.41}
$$

The set of equations 3.40 and 3.41 evaluate the linear and the angular impulse for a 2D inviscid rotational flow field. By taking the time derivative of these quantities, the forces and the moment of the forces, referring the origin of the frame of reference for a moving body are computed. For instance, the above cited equations, represent a straightforward and efficient approach to estimate the dynamical actions exerted on the bodies by the flows simulated in the previous sections 3.1.2, 3.1.3 and 3.1.4. In appendix A.2.6, a full analytical example of this procedure in computing the dynamical actions on a moving body is reported.

3.2 Viscous analysis

This part is devoted to present and validate a technique for the study of the unsteady incompressible viscous flow interacting with moving bodies. This subject represents a natural continuation of the previous inviscid analysis on the unsteady 2D flow past bodies characterized by a rigid motion.

The outline of this work is as follows. The section 3.2.1 illustrates the numerical solution of the vorticity equation based on a step of the Lagrangian advection of the vortex particles and a step of diffusion computed on a Cartesian grid. The continuity condition at the solid boundaries is enforced by means of a penalization technique. In section 3.2.3, a survey of strategies to compute the aerodynamic forces acting on the bodies is presented. A validation of the method is widely presented in 3.2.4, where several test cases with the 2D circular cylinder benchmark have been carried out. In section 3.2.5, some preliminary simulations of the wake past the vertical axis turbine are discussed.

3.2.1 The vortex level-set flow model

The numerical simulation of a full unsteady incompressible viscous flow, with a set of moving bodies immersed within, shows several difficulties for grid based methods. The main drawbacks income from the re-grid procedure in tracing the body motion, and from the high resolution necessary at the solid boundaries for high Reynolds numbers.

An efficient and accurate technique necessary in order to simulate such a kind of flow is represented by vortex methods (see, for instance, Cottet & Koumoutsakos (2000) [17]). For our simulations, we followed the innovative approach proposed by Coquerelle et al. (2006) [14] and Coquerelle & Cottet (2008) [15].

In these works, the Navier Stokes equation is defined in terms of a vorticity formulation and the vorticity field is numerically determined by a particle discretization. The no-slip condition at the solid wall boundaries is enforced by means of a penalization model (Angot et al. (1999) [4]). The interaction of the incompressible fluid with the rigid bodies is modelled through some level-set functions (see, for instance, Sethian (1996) [66]) which follow the different interfaces immersed in a Cartesian grid pattern and allow to manage the rigid motion and the collisions of the bodies. This approach exhibits a wide set of applications, such as in the multi-phase fluid dynamics and in more general problems of coupling between fluids and structures. The simulation of the vortex wake behind a vertical axis turbine involve a single phase fluid and a rigid rotation of two symmetrical straight blades immersed in an undisturbed stream.

Following [17], the hybrids vortex methods are based on the combination of

Lagrangian mesh-free schemes and Eulerian grid based schemes on the same flow region. These two approaches numerically solve different terms of the governing equations. An example of hybrid method is the Vortex-In-Cell (VIC) scheme: the non linear advection is computed by tracking the trajectories of the Lagrangian particles through a set of ODEs, whereas an Eulerian grid is adopted to solve efficiently the velocity field and the diffusive term.

The vortex level-set technique is a Vortex-In-Cell approach where the whole fluid-solid set is studied as a single system, i.e. a single flow. The coupling between the fluid and the solid boundaries is devised through a penalization method which enforces the continuity condition and provides the no-slip condition for the vorticity generation.

Let us consider a domain D with boundaries ∂D, where a single-phase fluid region $F(t)$ and a solid multi-connected region are defined $S(t)$, such that $F(t) \cup S(t) = D$. The rigid motion valid in $S(t)$ is formed by the linear velocity $\mathbf{v_G}$ of a pole, for instance the centre of mass, located in $\mathbf{x}_G$, and the angular velocity $\mathbf{\Omega}$; the velocity for each rigid set of bodies is then $\bar{\mathbf{u}} = \mathbf{v}_G + \mathbf{\Omega} \wedge (\mathbf{x} - \mathbf{x}_G)$. The incompressible 3D Navier Stokes equation without external force fields

$$\frac{\partial \mathbf{u}}{\partial t} + (\mathbf{u} \cdot \nabla)\mathbf{u} - \nu \nabla^2 \mathbf{u} + \frac{1}{\rho} \nabla p = 0 \tag{3.42}$$

and the continuity equation

$$\nabla \cdot \mathbf{u} = 0 \tag{3.43}$$

are enforced in $F(t)$. By considering the fluid-solid system as a single flow, the governing equation in the whole region D is

$$\frac{\partial \mathbf{u}}{\partial t} + (\mathbf{u} \cdot \nabla)\mathbf{u} - \nu \nabla^2 \mathbf{u} + \frac{1}{\rho} \nabla p = \lambda \chi_{S(t)} (\bar{\mathbf{u}} - \mathbf{u}) \tag{3.44}$$

where $\mathbf{u}$ is a 'fluid' velocity in $F(t)$ and a $\mathbf{u}$ 'rigid' velocity in $S(t)$. On the right-hand side, the penalization term is defined by the penalization parameter $\lambda \gg 1$, the rigid motion velocity $\bar{\mathbf{u}}$ and the characteristic function $\chi_{S(t)}$ capturing the solid boundaries. The parameter λ has the dimension of the reciprocal of a time unit, then the penalization term plays the role of an extra volume force term that induces the velocity field within $S(t)$ to become $\bar{\mathbf{u}}$. A brief investigation on the correct sign of the penalization term is reported in appendix A.2.3. A wide discussion on the advantages and the accuracy of the penalization technique, references and comparison with other immersed boundary approaches can be found in [4], Bruneau & Mortazavi (2004) [9] and Mittal & Iaccarino (2005) [42].

The penalized formulation of the Navier Stokes equation is a typical context where the implicit definition of the interfaces is natural and effective. Let us define ϕ as a signed distance function that is negative inside $S(t)$ and positive outside. The

characteristic function can then be defined by $\chi_{S(t)} = H(\phi)$, where $H(\cdot)$ is a suitable step function (appendix A.2.4). Following Sethian (1996) [66], the dynamics of an implicit surface is governed by an Hamilton-Jacobi equation with the form $\phi_t + \mathrm{H}(\nabla\phi) = 0$ where H is an hamiltonian function which is space and time dependent (see [69]). Since we consider a set of rigidly moving bodies, the level-set function has to satisfy

$$\frac{\partial\phi}{\partial t} + (\bar{\mathbf{u}} \cdot \nabla)\phi = 0 \tag{3.45}$$

and ϕ keeps unalterated the signed distance function.

Finally, let us consider the penalized Navier Stokes equation in the vorticity formulation. By applying the curl to the equation 3.44, we obtain

$$\frac{\partial\boldsymbol{\omega}}{\partial t} + (\mathbf{u} \cdot \nabla)\,\boldsymbol{\omega} = (\boldsymbol{\omega} \cdot \nabla)\mathbf{u} + \nu\nabla^2\boldsymbol{\omega} + \lambda\nabla \wedge [H(\phi)(\bar{\mathbf{u}} - \mathbf{u})]\,. \tag{3.46}$$

Let $\mathrm{d}/\mathrm{d}t(\cdot)$ be the notation pertinent to the material derivative and by expanding the penalization term, the equation becomes

$$\frac{\mathrm{d}\boldsymbol{\omega}}{\mathrm{d}t} = (\boldsymbol{\omega} \cdot \nabla)\;\mathbf{u} + \nu\nabla^2\boldsymbol{\omega} + \lambda H(\phi)\,(\bar{\boldsymbol{\omega}} - \boldsymbol{\omega}) + \lambda\delta(\phi)\,[\nabla\phi \wedge (\bar{\mathbf{u}} - \mathbf{u})] \tag{3.47}$$

where $\delta(\phi)$ is the 1D Dirac delta function, $\bar{\boldsymbol{\omega}} = 2\,\boldsymbol{\Omega}$ and $\nabla\phi$ corresponds to the unit normal pointed inwards. The last two terms play a significant physical role in the model. The first term clears the vorticity difference within the bodies, whereas the second member represents a vorticity generation term that is localized on the solid boundaries (bound vorticity, see [62]) and allows the no-slip condition to be imposed. The penalized vorticity equation 3.47 means that the rate of change of the vorticity, advected by the fluid in a Lagrangian frame of reference, is governed by the diffusive effects, the stretching effects, the production of bound vorticity and the vorticity cancellation within the solid bodies.

In vortex methods (see [17]) the rate of change of vorticity is modelled by means of discrete vortex particles, such that the solution of the equation 3.47 is localized only in the rotational regions of the flow field. This is the most important advantage of the vortex methods, that is the computational efforts are naturally addressed only to specific flow field zones. The vorticity field $\boldsymbol{\omega}$ is represented by a set of particles

$$\boldsymbol{\omega}(\mathbf{x}) = \sum_{p=1}^{N} \nu_p\,\boldsymbol{\omega}_p\,\zeta\,(\mathbf{x} - \mathbf{x}_p) \tag{3.48}$$

where N is the number of particles, $\mathbf{x}_p$ is the location and ν_p, $\boldsymbol{\omega}_p$ are the volume (constant due to the incompressibility constraint) and the strenght of a generical particle p. In addition, $\zeta(\cdot)$ is a smooth distribution function such that $\int \zeta(\mathbf{x})d\mathbf{x} = 1$,

which acts on the vortex support. The vortex particle advection can be described in the Lagrangian formulation by the following ODE

$$\frac{\mathrm{d}\mathbf{x}_p}{\mathrm{d}t} = \mathbf{u}\left(\mathbf{x}_p,t\right). \tag{3.49}$$

Since the incompressible velocity field is divergence-free, from the vector field theory (see, for instance, [68]) we can define a vector potential $\boldsymbol{\psi}$, such that

$$\mathbf{u} = \nabla \wedge \boldsymbol{\psi} \tag{3.50}$$

The vector potential $\boldsymbol{\psi}$ is a 3D extension of the so-called streamfunction ψ employed in chapters 2 and 3. The following vectorial identity allows to establish a relation between the streamfunction and the vorticity field

$$\nabla \wedge (\nabla \wedge \boldsymbol{\psi}) = \boldsymbol{\omega} = \nabla(\nabla \cdot \boldsymbol{\psi}) - \nabla^2\boldsymbol{\psi},$$

and, by imposing that the potential vector be solenoidal $\nabla \cdot \boldsymbol{\psi} = 0$, the equation becomes

$$\nabla^2\boldsymbol{\psi} = -\boldsymbol{\omega}. \tag{3.51}$$

The velocity field can be derived from a given vorticity field by means of the equation 3.51, a set of boundary conditions on ∂D and the definition 3.50. A discussion on the choice of a suitable set of boundary conditions is reported in the subsequent section 3.2.2.

The set of equations 3.45, 3.46 or 3.47, 3.48, 3.49, 3.50 and 3.51 with boundary conditions, represents the flow model of the level-set vortex method. The governing equation 3.46 (or 3.47) is in a dimensional form. A non-dimensional formulation can be inferred by introducing the following set of non-dimensional quantities, based on the reference length l_{ref}, the reference time t_{ref} and the reference velocity $u_{ref} = l_{ref}/t_{ref}$

$$\tilde{\mathbf{x}} = \mathbf{x}/l_{ref}, \;\; \tilde{t} = t/t_{ref}, \;\; \tilde{\mathbf{u}} = \mathbf{u}/\; u_{ref}$$
$$\tilde{\boldsymbol{\omega}} = \boldsymbol{\omega}\; t_{ref}, \;\; \tilde{\lambda} = \lambda\; t_{ref}, \;\; \tilde{\nabla}(\cdot) = \nabla(\cdot)\; l_{ref}$$

where the notation $\tilde{(\cdot)}$ indicates a non-dimensional quantity. Since the fluid is incompressible, the density ρ is considered unit. Defining the Reynolds number as $\mathrm{Re} = u_{ref}\; l_{ref}/\nu$ and replacing the non-dimensional quantity in the equation 3.46, the non-dimensional penalized vorticity equation reads

$$\frac{\partial\boldsymbol{\omega}}{\partial t} + (\mathbf{u}\cdot\nabla)\,\boldsymbol{\omega} = (\boldsymbol{\omega}\cdot\nabla)\mathbf{u} + \frac{1}{\mathrm{Re}}\nabla^2\boldsymbol{\omega} + \lambda\nabla\wedge\left[H(\phi)(\bar{\mathbf{u}}-\mathbf{u})\right], \tag{3.52}$$

where the $\tilde{(\cdot)}$ notation has been suppressed for clarity.

3.2.2 The level-set Vortex-In-Cell algorithm

In the previous section, we discussed how the level-set vortex method is a variation of a VIC technique. The VIC method is an hybrid technique that combines a particles mesh-free approach with a grid-based scheme to solve different members of the same governing equation. Taking into account the VIC scheme proposed in [14], in this section an algorithm is devised, with the aim of improving the accuracy and validating this method with standard benchmarks.

The present method is based on a viscous splitting algorithm, that is a technique used in order to manage successively the inviscid and the viscous processes of the governing equation. In [17] a wide and detailed discussion on the accuracy of this algorithm is reported. Considering a discretization in time $t^n = n\Delta t$ applied to the equation 3.46 or 3.47 where t^{n+1} is the time level to compute, each integration step Δt is formed by two substeps. During the first substep, the vortex elements are advected by the local flow velocity. From the new vortex particles' locations, the vorticity field is remeshed on the grid by means of an interpolation procedure. During the second substep, the diffusion operates on the new vortex locations on the grid and corrects the vorticity field. Since the governing equation exhibits a penalization term, an additional substep has to be introduced such that the vorticity field takes into account the no-slip condition at the solid boundaries.

It is important to remark that the interpolating-remeshing scheme is a fundamental tool for the accuracy of the whole method. A wide analysis on the remeshed particle methods in comparison with other numerical schemes and some references therein, can be found in [17] and in Cottet & Weynans (2006) [18]; here it is shown how the remeshed particle methods are equivalent to a class of high order finite differences schemes without the constraint of the CFL condition.

For the sake of simplicity, let us consider that the domain D is two-dimensional and is meshed by an orthogonal Cartesian equispaced grid, where $\Delta x \sim \Delta y \sim h$ and the particles' volume is $\nu_p = \Delta x \Delta y$. In our work, we adopted the M_4' smoothing interpolation formula that is third order accurate (see, for instance, [17]). The M_4' scheme can be described, for instance, by the following 1D interpolation kernel

$$M_4'(\tilde{x}) = \begin{cases} 0 & \text{if } |\tilde{x}| > 2 \\ \frac{1}{2}(2 - |\tilde{x}|)^2(1 - |\tilde{x}|) & \text{if } 1 \leq |\tilde{x}| \leq 2 \\ 1 - \frac{5\tilde{x}^2}{2} + \frac{3|\tilde{x}|^3}{2} & \text{if } |\tilde{x}| \leq 1, \end{cases} \tag{3.53}$$

where $\tilde{x} = x/\Delta x$ and x is the distance from the point to interpolate. In this 1D example, the influenced stencil consists of four surrounding grid points. In the 2D case, the M_4' scheme takes into account of the sixteen closest grid points around the particle to interpolate/remesh.

The algorithm is now discussed by studying an iteration in time. Let us consider that the flow field is known at the time level t^n and both the vorticity and the velocity field are defined on the grid. The particles trajectories 3.49 are integrated for the time-step Δt by means of a fourth order Runge-Kutta scheme (RK4). During a time-step Δt, for each RK substep, the velocity is interpolated from the grid onto the updated particle's position. As soon as the final location of a particle is determined, a remesh procedure assigns the new vorticity field on the grid. In the present method, all the interpolation (grid points to particles) or remesh (particles to grid) procedures are carried out by means of the aforesaid formula 3.53.

Let Δt and Δt_{conv} be the time-steps associated to solve the diffusive and the convective phenomena respectively. The quality of the numerical simulation also depends on choice of these time-steps. Following Ploumhans *et al.* (2000) [53], a cell Reynolds number in vortex methods can be defined as $\mathrm{Re}_h = |\omega|h^2/\nu$ and a good resolution requires $\mathrm{Re}_h = O(1)$, so that the principal viscous scales are detected. On the other hand, the diffusive phenomena are solved with accuracy by imposing $\nu\Delta t/h^2 = O(1)$. Multiplying these two conditions, we obtain an accurate choice of the convective time-step $\Delta t_{conv} \sim 1/|\omega|$. This condition is used with the aim of making more stable the advection at large Reynolds numbers as well. These assumptions are adopted to choice a suitable convective time-step for the RK4 scheme.

In the present method, the RK4 scheme operates for a convective time-step that is defined by $\Delta t_{conv} \sim 1/|\omega^n_{max}|$, where ω^n_{max} is the maximum absolute valued of the vorticity field at t^n. Being $k = \Delta t/\Delta t_{conv}$, the RK4 scheme is then successively applied for k-times, and the iterated remeshing steps allow to distribute the vorticity onto the grid.

Let us consider the motion of a solid wall into the level-set VIC algorithm. The level-set function ϕ is defined as a signed distance function, that is, its zero level corresponds to the body's wall. At t^0, the signed distance function is initialized as a scalar value on a support S_ϕ defined on the grid points. The body's trajectory can be evaluated by integrating the equation 3.45. Since the motion defined by $\bar{\mathbf{u}}$ is rigid, ϕ does not change and it is not necessary a reinitialization procedure.

The equation 3.45 can be interpreted as a material derivative $\mathrm{d}\phi/\mathrm{d}t = 0$, and the motion can be integrated through a lagrangian method. For each time-step, the locations representing the support S_ϕ, where ϕ is defined, are advected by $\bar{\mathbf{u}}$. From these new positions, the signed distance function is remeshed on the grid and the body's boundary is hence transported. Moreover, if the rigid motion is prescribed, the trajectory is known *a priori* and the signed distance function can be constructed and stored at starting once and for all.

Let us take to handle the remaining parts in the governing equation 3.46. Since

the stretching term vanishes for 2D flows, we consider now the viscous and penalization contributions. The diffusive term is integrated onto the grid by means of an Euler explicit scheme, while the laplacian is evalutated, with a second order accuracy, by the standard centred finite differences five points stencil.

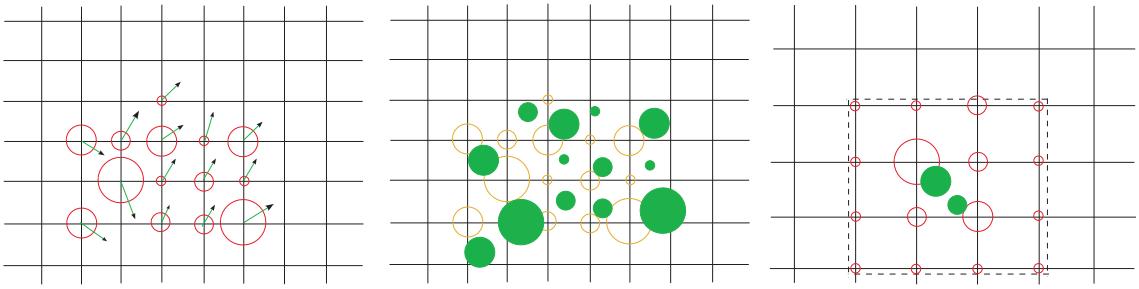

Figure 3.20. Particles interpolation scheme. The circle's size denotes the strenght of the particle and the solid circles represent the advected particles. a) vortex particles and velocity field; b) advection step; c) remesh-diffusion step.

The discretization and the integration of the penalization term affect the choice of the penalization parameter λ, and the larger the value of λ, the better the quality of the penalization, i.e. the quality of the boundary condition at the fluid/solid interface. An Euler explicit time discretization does not allow to use $\lambda > 1/\Delta t$, and as a result several tests have been carried out therein.

On the other hand, following [15], an implicit Euler time discretization for the penalization term in the Navier Stokes equation yields

$$\mathbf{u}^{n+1} = \frac{\mathbf{u}^n + \lambda H(\phi)\Delta t\ \bar{\mathbf{u}}^n}{1 + \lambda H(\phi)\Delta t}$$

Finally the vorticity field at the time-step t^{n+1} is evaluated on the grid by taking the curl $\omega^{n+1} = \nabla \wedge \mathbf{u}^{n+1}$ and computing the derivatives through the second order centred finite differences approximations.

The problem of evaluating the velocity field and the boundary conditions is now taken into account. Being ω^{n+1}, the updated vorticity field, the stream function field is computed by solving the linear Poisson equation 3.51 on the Cartesian orthogonal grid with boundary conditions on ∂D. In our simulations, a Fast Poisson Solver is adopted (Fishpack90 library [3]). A multigrid solver (for instance, Mudpack library [2]) can be recommended for higher grid refinement and parallel computations, even though there is loss in efficiency.

In vortex methods, boundary conditions are explicitly used only to solve the Poisson equation and are enforced on the non-primitive variable ψ. A wide investigation on the boundary conditions for such kinds of problems is also reported in Mortazavi (1997) [44] and Mortazavi & Giovannini (2001) [45]. In general, a drawback of grid-based vortex methods is represented by the accurate choice of boundary conditions for the velocity field. The Eulerian-Lagrangian domain decomposition (see [17]) is an hybrid technique that can overcome the boundaries' constraint: an Eulerian grid-based vortex method solves the regions of the flow field where the velocity/vorticity gradients are important, whereas a pure Lagrangian approach is performed in the regions where the convection is prevalent.

In the present method, on the upstream and downstream boundaries, a Neumann condition is enforced. On the lower and upper boundaries, a Dirichlet condition settles the flow mass rate. The direct enforcement of a given velocity distribution as boundary condition, for instance a ground effect or a parabolic velocity profile at upstream, can be implicitly carried out by means of the penalization term. Through a suitable level-set function within the flow field, we can define an arbitrary region where a fixed velocity distribution is settled. For instance, a 2D channel flow can be simulated by means of two horizontal strips, where $\bar{\mathbf{u}} = 0$, along the lower and upper boundaries.

A blockage effect arising from the boundary conditions has been observed in terms of an increased shedding frequency and a distorted wake near the downstream boundary. Indeed the validation tests in the case of the 2D flow past a circular cylinder have been carried out in an extended domain, such that the blockage effects are negligible (see section 3.2.4).

In figure 3.20 the particle interpolating/remeshing scheme is illustrated, and the algorithm devised for the level-set vortex method is summarized below.

initialization $n = 0$ - time-step

1. stream function initialization (on grid)
2. preliminary velocity and vorticity field (on grid)
3. penalization (on grid):
    - implicit penalization substep
    - penalized vorticity field and Poisson problem
    - penalized velocity field

---

marching $n = 1$ - time-step

1. advection of the particles (RK4):
    - for each RK sub-step the velocities are interpolated from the grid to the particles
    - vorticity remesh (particles $\rightarrow$ grid)
2. explicit diffusion substep (on grid)
3. Poisson problem (on grid)
4. preliminary velocity field (on grid)
5. rigid motion of the distance function
6. penalization (on grid):
    - implicit penalization substep
    - penalized vorticity field and Poisson problem
    - penalized velocity field

---

marching $n = 2$ - time-step

. . .

3.2.3 Forces evaluation

A survey of the evaluation of the unsteady forces exerted on moving bodies is above reported in section 3.1.5. The advantage of the level set penalization technique is in the aptitude to handle moving interfaces. The 'one-shot' penalization here devised allows to track the solid boundary with an accuracy of $O(\Delta x)$, and the exact detection of the wall is not straightforward. The forces and moments computation by means of an explicit integration of pressures and viscous stresses is not simple, because it depends on the accuracy of the velocity gradients close to the fluid/solid interfaces.

Connected to the vortex methods, where the pressure field is not necessarily derived, the theory of the hydrodynamic impulse offers a closed formulation for computing the unsteady forces experienced by a moving body immersed in an incompressible and rotational flow (see section 3.1.5). The main advantage provided by the impulse theory is that the forces can be determined without requiring the pressure field and the integration of stresses along the rigid boundaries. Indeed, the linear impulse $\mathbf{I}$ and the angular impulse $\mathbf{A}$ are natural invariants of the flows, with the condition that external body forces, vorticity and velocity vanish at infinity. For viscous flows the invariance of $\mathbf{I}$ and $\mathbf{A}$ exists on condition that flow is unbounded, because the effect of viscosity at the boundaries is equivalent to an extra body force. A more detailed discussion on the impulse theory and references therein are reported in [62].

Since in the Vortex-In-Cell method the velocity and vorticity fields are supported on a mesh, and the flow field can be determined only within the boundaries of the computational domain D, the forces' computation through the hydrodynamic impulse is not straightforward. In the case of a set of bodies immersed in a stream, the wake generated is naturally convected out of the boundaries, the outgoing vorticity is lost and the hydrodynamic impulses of the whole flow field can not to be evaluated.

This drawback can be overcome by means of the 'impulse' equation 3.28 or the 'momentum' equation 3.29 discussed in section 3.1.5, where the forces can be computed by evaluating the velocity field or its derivatives within a prescribed control volume. In section 3.2.4 the aforesaid equations are used to validate the level set vortex method on the classical benchmark of 2D incompressible flow past the circular cylinder.

3.2.4 2D circular cylinder test case

The literature about the classical benchmark of the bluff body aerodynamics is wide. A deepened survey of this subject with several physical remarks and references therein can be found in Williamson (1996) [76].

Here, we present some results of the numerical simulations of an incompressible flow past a 2D circular cylinder performed by the level set vortex method by varying the Reynolds number. Three ranges of Reynolds numbers are taken into account.

A low Reynolds analysis has been carried out for ($\mathrm{Re} = 60 \div 200$), where the flow is laminar and without 3D wake instabilities [76]. We investigated the capability of the numerical method to predict the correct vortex shedding frequencies and the steady solutions for $\mathrm{Re} < \mathrm{Re}_{crit} \approx 49$, where Re_{crit} marks the bifurcation point of the wake instability. Moreover, the time evolution of C_D and C_L for $\mathrm{Re} = 100$ and $\mathrm{Re} = 200$ is provided and is compared with the results found in literature. In Ploumhans & Winckelmans (2000) [53] the flow past an impulsively started 2D circular cylinder at $\mathrm{Re} = 550$ was studied through a high resolution vortex method. The vorticity field and the C_D time history are compared with the simulations provided by the present method. The highest Reynolds number tested here is $\mathrm{Re} = 9500$, for an impulsively started cylinder. The vorticity pattern and the drag time history are compared with the numerical simulations of Koumoutsakos & Leonard (1995) [37] yielded by a vortex method.

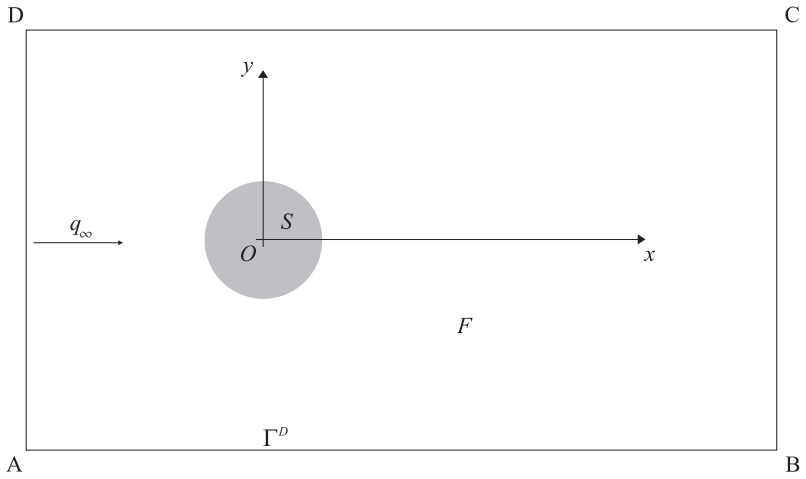

Figure 3.21. Computational domain $D = F \cup S$, where F is the fluid region and S is the solid body region.

The computational domain and the geometrical setup are shown in figure 3.21, where D is a rectangle delimited by its boundaries Γ^D. The diameter d of the circular cylinder is unit, the free stream q_∞ is unit and the Reynolds number is defined by $\mathrm{Re} = q_\infty d/\nu$. The whole computational domain is meshed by an equispaced Cartesian orthogonal grid.

For the subsequent simulations of the wake past the circular cylinder, the flow field is computed by solving the Poisson problem 3.51 with a Neumann condition

at downstream Γ^D_{DA} and upstream Γ^D_{BC}, while a Dirichlet condition of the streamfunction over Γ^D_{AB} and Γ^D_{CD}. In particular, the potential flow around the cylinder is considered and the value of the associated streamfunction is enforced over Γ^D_{AB} and Γ^D_{CD}, that is

$$\psi = q_\infty y \left(1 - \frac{(d/2)^2}{x^2 + y^2}\right).$$

The undisturbed stream q_∞ passing through the cylinder is used as initialization.

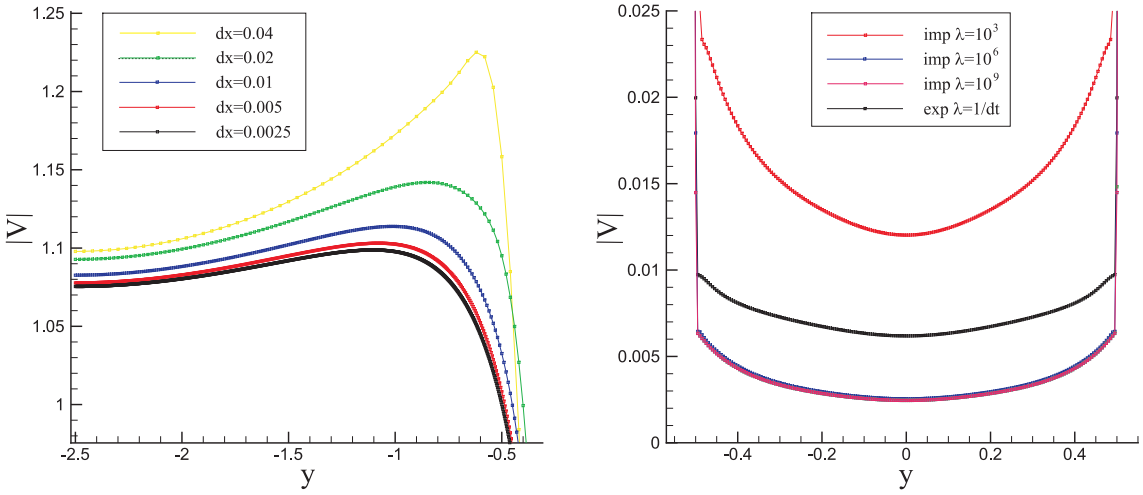

Figure 3.22. Convergence on grid test (left). Effect of the penalization parameter λ (right).

At first, the convergence on grid of the present method is verified. We considered an impulsively started cylinder at $\mathrm{Re} = 550$. The numerical simulation was stopped at the instant time $t = 3$ and the l^2-norm of the velocity is plotted along a section $x_s = 1.5$ of the flow field. By increasing the grid refinement the velocity profiles converge to a single curve, as presented in the left-hand side picture in figure 3.22. The penalization parameter has been set to $\lambda = 10^{10}$ and the space discretizations are reported in figure.

By varying the penalization level, the velocity profiles at $t = 3$ obtained along a section $x_s = 0$ through the cylinder are plotted in figure 3.22 on the right-hand side picture. We compared in terms of the quality of penalization the implicit penalization based on the equation 3.52 to the explicit penalization (see section 3.2.2). Practically, the explicit penalization allows to use $\lambda \leq 1/\Delta t$, whereas the implicit penalization is unconditionally stable for high values of the penalization parameter [15]. The velocity profiles computed by the implicit penalization for three values of λ are compared to the profile obtained by the explicit penalization. For

$\lambda > 10^6$ the quality of the penalization does not get better. The space discretization adopted here is $h = 0.005$, but some tests have been carried out show that the quality of the penalization improves with higher grid refinement.

The numerical validations, illustrated in figure 3.22, are referred to the initial transient of an impulsively started circular cylinder. Since these tests were obtained at t=3, when the vortex wake is not fully developed, the simulation is not so influenced by the computational domain boundaries. Therefore both tests were performed on a rectangular computational domain $D = [-1.5, 4.5] \times [-2.5, 2.5]$.

Let us consider the low Reynolds analysis. At low Reynolds numbers, the viscous effects are predominant, so that the choice of the time discretization has to take into account the fine-resolution of the diffusion phenomena. Following [53] the non-dimensional time-step Δt is determined by the condition $\Delta t/(h^2\ \mathrm{Re}) \sim O(1)$.

Various tests have been carried out by increasing the blockage ratio $d/(y_D - y_A)$, and a growth of the shedding frequency has been noticed. The size of the computational domain is chosen such that the effects of the boundaries on the shedding frequencies are negligible. The subsequent simulations have been performed on a flow region enclosed in the rectangle $D = [-7.5, 25] \times [-7.5, 7.5]$ with 3250×1500 grid points ($h = 0.01$). The penalization is enforced by means of the implicit formulation 3.52 and the penalization parameter is $\lambda = 10^{10}$.

The flow regime is laminar and the solution is steady and stable for $\mathrm{Re} < \mathrm{Re}_{crit}$. In figure 3.23, the streamlines of the steady solution at $Re = 13.05$ is shown. On the left-hand side, a picture of an experimental visualization is reported (see van Dyke (1982) [73]) and the the equivalent frame computed by the present method is shown on the right-hand side.

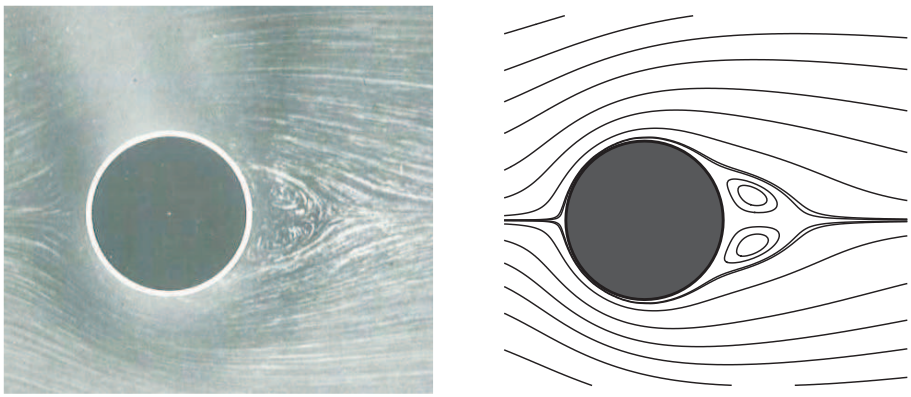

Figure 3.23. Streamlines at $Re = 13.05$

By increasing the Reynolds number, the flow regime is still laminar but the steady solution becomes unstable when $\mathrm{Re} > \mathrm{Re}_{crit}$. On the left-hand side picture of figure 3.24, the amplitude A_ω of the fluctuation of the vorticity reported at the arbitrary monitoring point $P = (2.5,\ 0.5)$ is plotted by varying Re. Since for a flow regime close to the bifurcation point Re_{crit} the wake instabilities grow slowly, for $\mathrm{Re} < 60$ the numerical simulation, without introducing any perturbation, did not show the wake oscillations within a reasonable computation time. However, the critical Reynolds number can be extrapolated through the amplification factor curve. Being $\mathrm{St} = fd/q_\infty$ the Strouhal number, where f is the vortex shedding

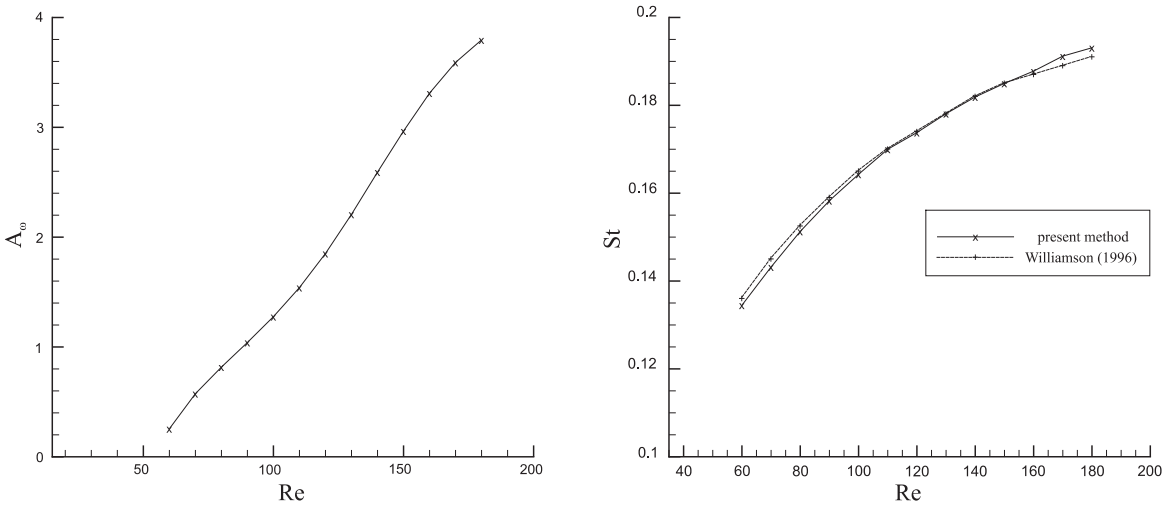

Figure 3.24. Amplification factor A_ω curve (left). Strouhal-Reynolds curve (right).

frequency, a comparison between the numerical and the experimental St *versus* Re curve is shown on the right-hand side of figure 3.24. The experimental data are given by [76]. An estimation of the average relative error between the curves yields $\approx 0.6\%$.

The evaluation of forces has been carried out by means of the 'momentum equation', discussed in section 3.2.3 (the mathematical derivation for the 2D circular cylinder test case is presented in appendix A.2.7). We investigated on the averaged values and the amplitudes of the fluctuations of drag and lift coefficients for flows at $\mathrm{Re} = 100$ and $\mathrm{Re} = 200$. The following results were obtained: at $\mathrm{Re} = 100$ $\bar{C}_D = 1.40$, $\Delta C_D = 0.01$, $\Delta C_L = \pm 0.32$. At $\mathrm{Re} = 200$ $\bar{C}_D = 1.44$, $\Delta C_D = 0.05$, $\Delta C_L = \pm 0.75$. In figure 3.25, the time history of C_D and C_L for the flow past the circular cylinder at $\mathrm{Re} = 200$ is shown. These quantities can be well-compared with the results in literature. For instance some numerical results at the same Reynolds numbers and references therein can be found in Russell & Jane Wang (2003) [59].

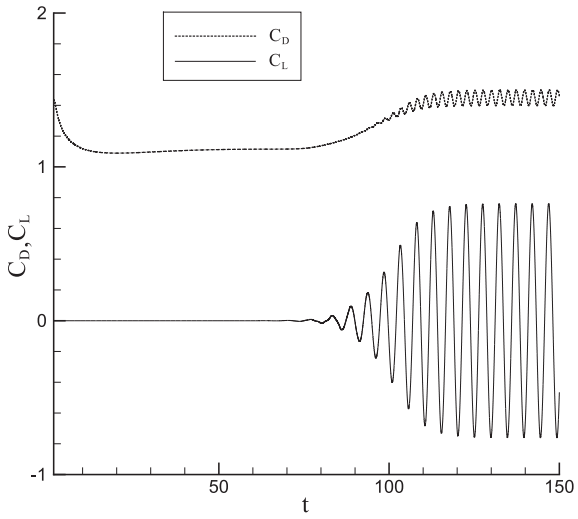

Figure 3.25. Time evolution of the drag and lift coefficients at Re = 200.

These two simulations have been performed on the computational domain $D = [-3.75,\ 12.5] \times [-3.75,\ 3.75]$ with $h = 0.005$ and the penalization parameter is $\lambda = 10^{10}$. The control volume is enclosed by the rectangle $V = [-1.75,\ 3.25] \times [-1.75,\ 1.75]$.

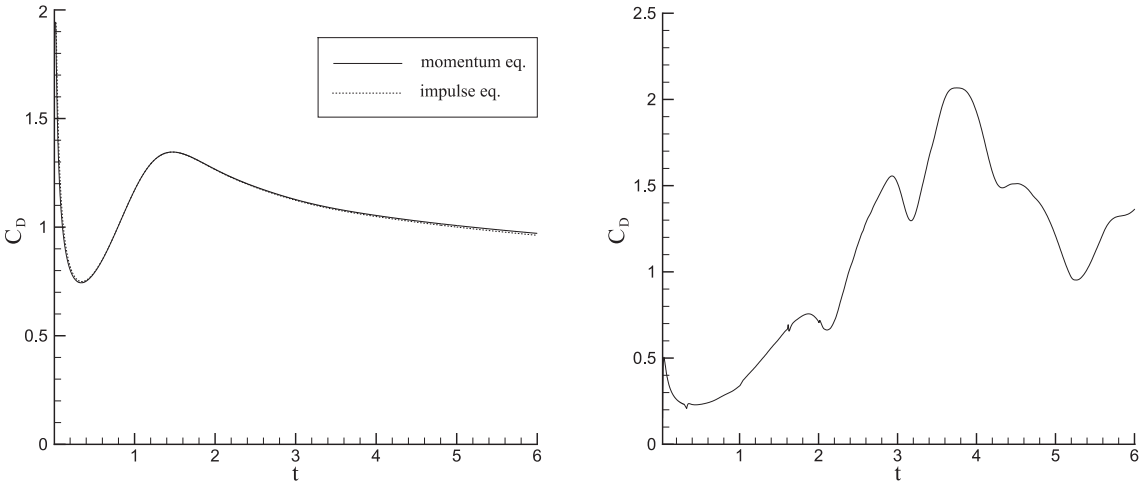

Figure 3.26. Time evolution of the drag coefficient for the impulsively started cylinder at Re = 550 (left) and at Re = 9500 (right).

Let us consider the test case of the 2D flow around an impulsively started circular

cylinder at Re = 550. The comparison between the C_D time evolutions computed by the 'momentum equation' method and the 'hydrodynamical impulse' method is shown in the picture on the left-hand side of figure 3.26. As discussed in sections 3.1.5 and 3.2.3, the hydrodynamical impulse of a vortex is an invariant of the flow if the velocity and the vorticity at infinity are null. On the contrary, in our computations, a free stream q_∞ is considered at infinity while the frame of reference is fixed on the body. The impulse theory can be applied here only if the velocity at infinity is removed by the Galileian transformation illustrated in appendix A.2.5, and if the computational domain is large enough thus the wake does not perturb the downstream boundary. Therefore the simulations were stopped at t=6, when the boundaries are not influenced by the growing vortex wake yet. The C_D *versus* time curves for two

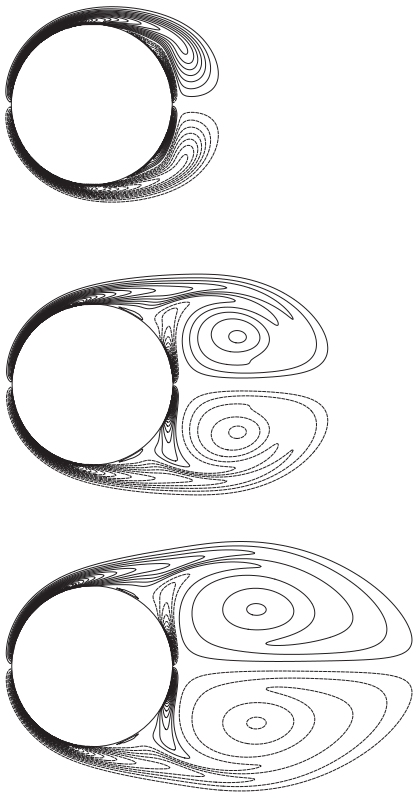

Figure 3.27. Iso-contours of vorticity for t = 1, 3, 5 for the impulsively started cylinder at Re = 550.

methods above are plotted in figure 3.26 (left). The curves coincide by increasing the grid refinement, in accordance with the references in literature (Koumoutsakos & Leonard (1995) [37] and Ploumhans & Winckelmans (2000) [53]). The figure 3.27 shows the iso-contours of vorticity which are in fine accordance with [53]. The

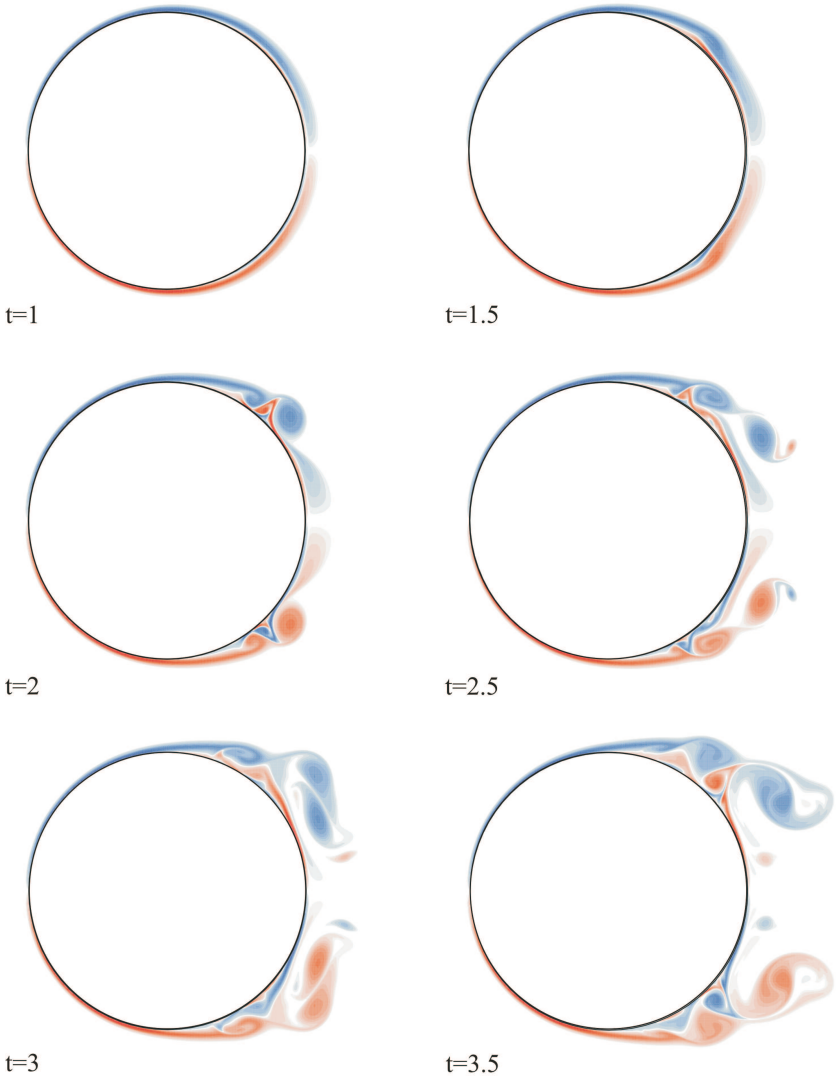

Figure 3.28. Iso-contours of vorticity for $t = 1, 1.5, 2, 2.5, 3, 3.5$ for the impulsively started cylinder at $\mathrm{Re} = 9500$.

computational domain for this simulation is $D = [-3.75, 12.5] \times [-3.75, 3.75]$ with $h = 0.005$ and the penalization parameter is $\lambda = 10^9$.

The last simulation on the circular cylinder benchmark was carried out in the case of flow around the impulsively started cylinder at $\mathrm{Re} = 9500$. Some numerical

results obtained by a vortex method can be found in Koumoutsakos & Leonard (1995) [37]. The Reynolds number is higher than the previous cases and the flow is physically characterized by typical 3D structures (see [76]). Since at large Reynolds numbers the convective phenomena become predominant, the integration time-step is not chosen by the condition $\Delta t/(Re\ h^2) \sim O(1)$, but it is heuristically reduced to $\Delta t = 0.005$. In figure 3.28, six snapshots at the times = 1, 1.5, 2, 2.5, 3, 3.5 of the iso-contours of vorticty are shown and are in good accordance with the results of the simulations provided in [37]. Since the Reynolds number is larger than the previous cases, an higher grid refinement is taken into account in order to trace the smaller scales in the flow field.

In the picture on the right-hand side of figure 3.26 the evolution in time of the drag coefficient is reported, where the computation has been carried out by means of the 'momentum equation'. The computational domain for this simulation is $D = [-1.5, 4.5] \times [-2.5, 2.5]$ with $h = 0.0025$ and the penalization parameter is $\lambda = 10^9$. In accordance with [37], the time is non-dimensionalized and it is based on the cylinder radius.

3.2.5 Preliminary simulations of the vertical axis turbine

Here, we present some simulations of the two dimensional vortex wake past a vertical axis turbine (VAT). The level set vortex method discussed in sections 3.2.1 and 3.2.2 is set in order to manage the rigid motion of a two bladed VAT. The flow regimes at two Reynolds numbers are taken into account.

The unsteady forces and torque exerted on the shaft still have not been computed, but the preliminary tests carried out on the circular cylinder benchmark (see section 3.2.4) suggest that the level set vortex method allows the performance evaluation of the VAT. By means of the time history of the unsteady loads, a dynamical simulation of the turbine immersed in a variable stream and coupled with the characteristic curve of a braking group would be possible.

The results here presented are related to an impulsively started VAT, which is enforced to rotate with a constant angular velocity Ω and is immersed in a stream with velocity q_∞ at infinity. R is the blade radius and c is the airfoil chord.

We discussed, in section 3.2.2, that in the simulation of a set of solid bodies that move rigidly, the numerical integration of equation 3.45 is not necessary. At starting of the computation, the signed distance function ϕ is defined and stored once and for all only over a local support S_ϕ. For each time-step, S_ϕ moves rigidly and, at the new location, ϕ is remeshed on the grid by means of the $M'4$ scheme 3.53. The blade section used in our vertical axis turbine is a symmetrical Kármán-Trefftz airfoil with a slightly smoothed trailing edge. In figure 3.29, some levels of the distance function ϕ that define the airfoil are shown on a coarser grid than the implemented one. If the frame of reference is fixed on the turbine's rotation axis

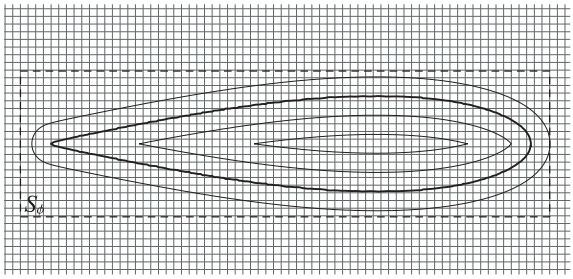

Figure 3.29. Distance function ϕ iso-contours. The dashed rectangle S_ϕ is the support of ϕ.

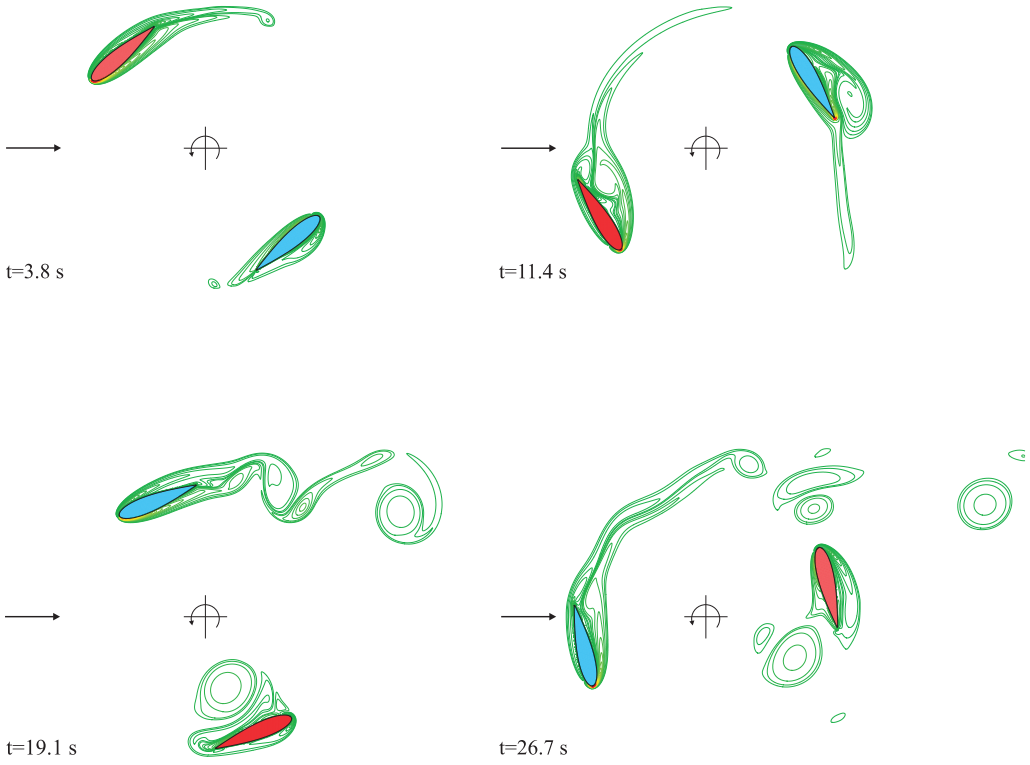

Figure 3.30. Iso-vorticity lines of the wake past the VAT at Re = 1000. Snapshots at times $t = 3.8$, 11.4, 19.1 26.7 in seconds.

then the computational domain is $D = [-6, 6] \times [-3.5, 3.5]$ with 3001×1751 grid points ($\Delta h = 0.004$). The penalization parameter is $\lambda = 10^{10}$. The non-dimensional chord and free stream are unit, while the blade radius is 1.5 and the angular velocity is 1.5. The Poisson problem 3.51 is solved by setting these boundary conditions: on

the upstream/downstream boundaries a Neumann condition is imposed, and on the horizontal boundaries a Dirichlet condition sets the flow mass rate through the flow domain.

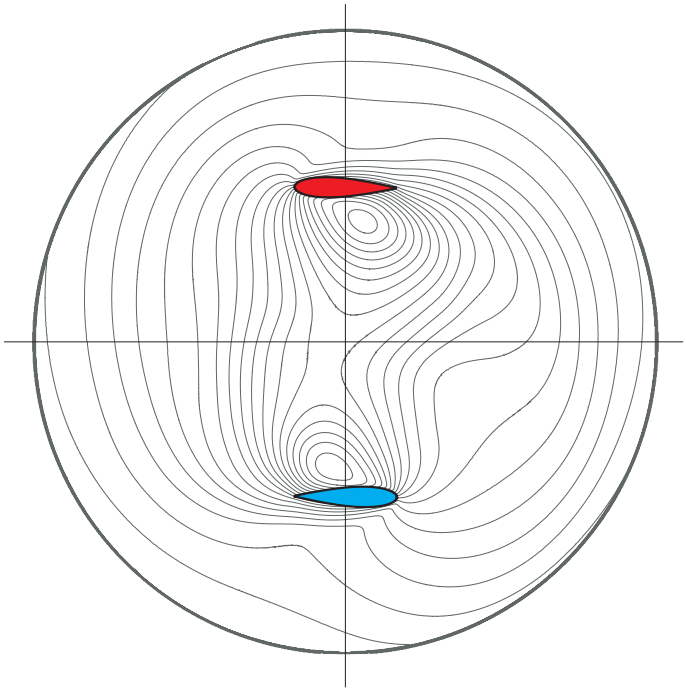

Figure 3.31. Averaged-in-time streamlines for the VAT at Re = 1000. The iso-lines are represented in the relative frame of reference.

The Reynolds numbers for a realistic simulation of a medium/small wind or water turbine can be located in the wide range $10^4 \div 10^6$, where the flow is in a transitional regime and is dominated by convective phenomena. The choice of the integration time-step would be such that Δt is small enough for a vortex particle to move only a fraction of the space discretization h.

However such Reynolds numbers would need a grid refinement which is not achieved in the present work. Two simulations are perfomed in the range of the Reynolds numbers which was verified above for the circular cylinder benchmark. A reasonable Reynolds number for a VAT can be defined by choosing the blade section chord c as reference length and the maximum relative velocity V_{rel}^{max} as reference velocity, where $V_{rel}^{max} = |q_\infty| + |\Omega R|$ (see figure 3.2 in section 3).

A low Reynolds number case is simulated. We considered a wind turbine with a blade section chord $c = 0.2$ m, radius $R = 0.3$ m, rotating with $\Omega = 0.185$ rad/s and immersed in a stream $q_\infty = 0.025$ m/s. The respective Reynolds number

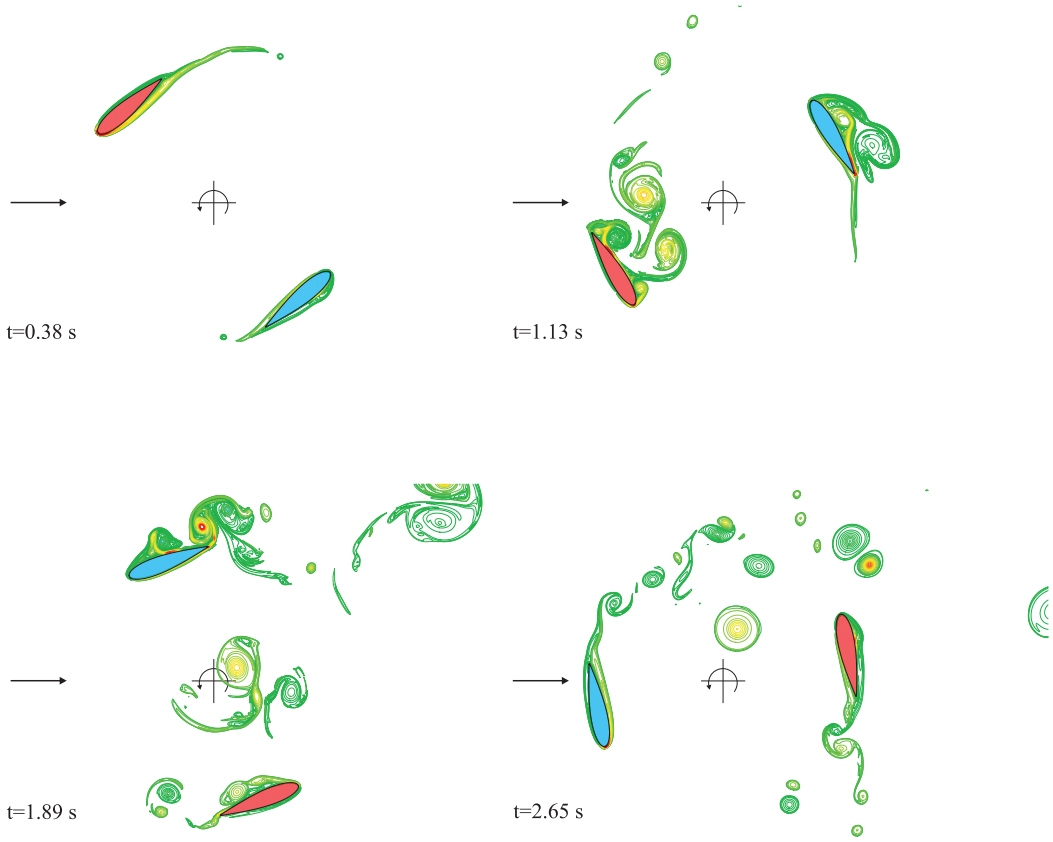

Figure 3.32. Iso-vorticity lines of the wake past the VAT at Re = 10000. Snapshots at times $t = 0.38, 1.14, 1.91, 2.67$ in seconds.

is 1000 ($\nu_{air} = 1.6\ 10^{-5}$ m^2/s at 20°C). As dicussed in 3.2.4, at low Reynolds numbers the time step is assumed by taking into account that the viscous effects are predominant. For this simulation we assumed $\Delta t = 0.001$. In figure 3.30 four snapshots representing the iso-contours of vorticity are reported.

In the introduction 3 we discussed on the unsteadiness of the flow field around a vertical axis turbine. A meaningful description of the flow around the turbine can be provided by evaluating the averaged-in-time stream function field, for a fully developped wake. For such representation, the frame of reference is centred on turbine's axis and rotates jointly with the blades. In figure 3.31 the averaged-in-time stream function for the Re=1000 simulation is shown. The average is computed for a simulation time of ≈ 250 s, that is equivalent to ≈ 7.5 rounds of a blade.

An higher Reynolds number case for a wind turbine operating at low-wind speed is provided by considering the previous VAT geometry with the working conditions

$\Omega = 1.85$ rad/s and $q_\infty = 0.25$ m/s. The respective Reynolds number is 10000. The integration time step is chosen to be $\Delta t = 0.0002$. In figure 3.32 four snapshots of the simulation are presented.

All the computations have been performed on a single CPU of a node bi-dual core AMD Opteron 2.2 GHz, and the runtime required for the simulation of a blade loop is ≈ 24 hours.

3.3 Concluding remarks

The survey of the wake past a vertical axis turbine immersed in a stream, provided the opportunity to devise some numerical and analytical tools which allow to simulate efficiently the inviscid and the viscous flow field around a set of moving bodies.

The inviscid analysis is addressed by means of a blob vortex method which allowed to simulate the two-dimensional rotational unsteady flow field with an high order of accuracy. Though the present method is valid in the limit of an inviscid model and does not take into account the local occurrence of secondary separations, it is able to describe correctly the vortex shedding past bluff bodies. In fact, since the main viscous effect causing the separation is modelled by the Kutta condition, inertia rather than viscosity governs the global instability of the vortex shedding phenomena.

A first simulation was carried out on a single-blade Darrieus turbine with a trapping vortex blade section designed analytically. The numerical examples show that vortical structures are generated and trapped by the cavities and that vortex shedding is prevented. The two-blades architecture is not taken into account here, but a preliminary study on the vortex motion in a doubly connected domain is presented. The flow field has been transformed, by conformal mapping, into a doubly periodic domain where the complex velocity is defined by an elliptic function, which is unique once an additive time-dependent function $\kappa(t)$ is determined. This function is evaluated through the Kelvin theorem, that is through the fact that the sum of the bound and shed circulations past each body has to remain constant. As a realistic example, the impulsive start of an airfoil-flap section is simulated through the blob vortex method.

The wake past the two-blades turbine is described by means of a low-order model in order to overcome the drawback of an excessive cost in computing time. The quality of the simulation has been compared with the corresponding high order simulation. The blade section considered is not equipped with the trapping cavities technology, but this extension can be implemented in a straightforward manner.

A survey of the forces and moments exerted by the fluid on a set of moving bodies in a free stream is given. Through the computation of the linear and angular impulse of the wake vorticity in the whole flow domain and of the bound vorticity at the walls of the moving bodies, the forces and the moments are determined. A general definition of the linear and angular impulse for the flow model simulated by the blob vortex method is given. An analytical example is provided by determining the unsteady loads exerted by the potential flow field on the shaft of a one-bladed VAT with elliptical blade section.

The application of the impulse theory to the low-order model of the two-blades

turbine provides an efficient tool to design a VAT in the pre-project phase. The integration of the performance evaluation method into the reduced-order model is now in progress.

The viscous analysis is carried out through an hybrid vortex method (Vortex-In-Cell scheme), where the continuity condition at the solid boundaries is enforced by means of a penalization technique. The definition of the solid boundaries is made implicitly through a level-set function, which moves rigidly, immersed in a Cartesian equispaced grid. Following Noca *et al.* (1999) [46], for the present method, the forces can be evaluated without any information on the pressure field, but only through the knowledge of the velocity and vorticity fields.

The numerical method is validated by means of several test cases performed at different Reynolds numbers on the classical 2D circular cylinder benchmark. At first the convergence on the grid of the method and the quality of the impermeability condition have been verified. The vortex shedding frequency, in a range of Reynolds numbers where the flow is still 2D ($\mathrm{Re} < 180$), is detected and compared with the experimental data found in literature. The time evolution of the drag and lift coefficients is computed for two Reynolds numbers in the 2D laminar regime, and the results are well compared with the literature. For higher Reynolds numbers, Re=550 and Re=9500, the impulsively started circular cylinder test is considered. The vorticity fields at different times and the time history of the drag coefficient are evaluated and compared with the data in literature.

Finally, the above method is implemented for the vertical axis turbine simulation. Two examples of the vortex wake at different Reynolds numbers are reported. By taking into account of the preliminary results provided by the inviscid method, the evaluation of the turbine's performance and the study of the effect of trapping cavities represent a goal of the ongoing research activity.

Appendix A

Derivations

A.1 Mappings

A.1.1 Curved plate in a channel

The conformal mapping that transforms a channel with a wall-mounted strip onto a channel without obstacles is presented here. In figure A.1, the mapping chain is illustrated. The map operates on a strip on the ζ-plane. The half-τ-plane is obtained by

$$\tau = (\tau - \tau_\infty)e^\zeta + \tau_T$$

where τ_T and τ_∞, respectively, are the images of the tip of the plate and the point at the infinity. The segment A-B on the real axis is mapped onto a circular arc on the σ-plane using the inverse of the elementary mapping $\tau = \sigma + 1/\sigma$. Then a translation/normalization transforms the σ-plane into the λ-plane

$$\lambda = \sigma|i - \lambda_c| + \lambda_c$$

where λ_c is the centre of the entire circle. Another Joukowskii mapping and a successive normalization map the circle on the λ-plane onto a curved plate on the μ-plane

$$\nu = \tfrac{1}{2}\left(\lambda - \tfrac{1}{\lambda}\right)$$

$$\mu = \mathrm{Im}\left[\mu_\mathrm{T}\right]\nu + \mathrm{Re}\left[\mu_\mathrm{T}\right]$$

The physical z-plane is obtained by z =logμ. Two free parameters, μ_c and the reference length y_T, determine the camber and the height of the plate. In our examples μ_c =-2 and y_T =1.3.

A.1.2 Vortex-capturing airfoil

The mapping chain $z \rightarrow \zeta$ is described here. The generated airfoil section results in a variation of the Kármán-Trefftz profile. As shown in figure A.2, the trailing edge T of the airfoil in figure 2.19 is mapped onto the quasi-circle on the λ-plane by the Kármán-Trefftz mapping

$$\frac{z/A - 1}{z/A + 1} = \left(\frac{\lambda - \lambda_T}{\lambda - (\lambda_N + \delta)}\right)^\tau$$

where $\tau = (2\pi - \epsilon)/\pi$, ϵ is the trailing edge angle, A is a scaling factor and $\lambda_N + \delta$ identifies a point located inside the airfoil, close to the leading edge. On the μ-plane (figure A.3), the quasi-circle is mapped onto the unit circle and the cusp K is smoothened through the following modified Ringleb's mapping

$$\lambda = \mu + \frac{a}{\mu - \mu'_K}$$

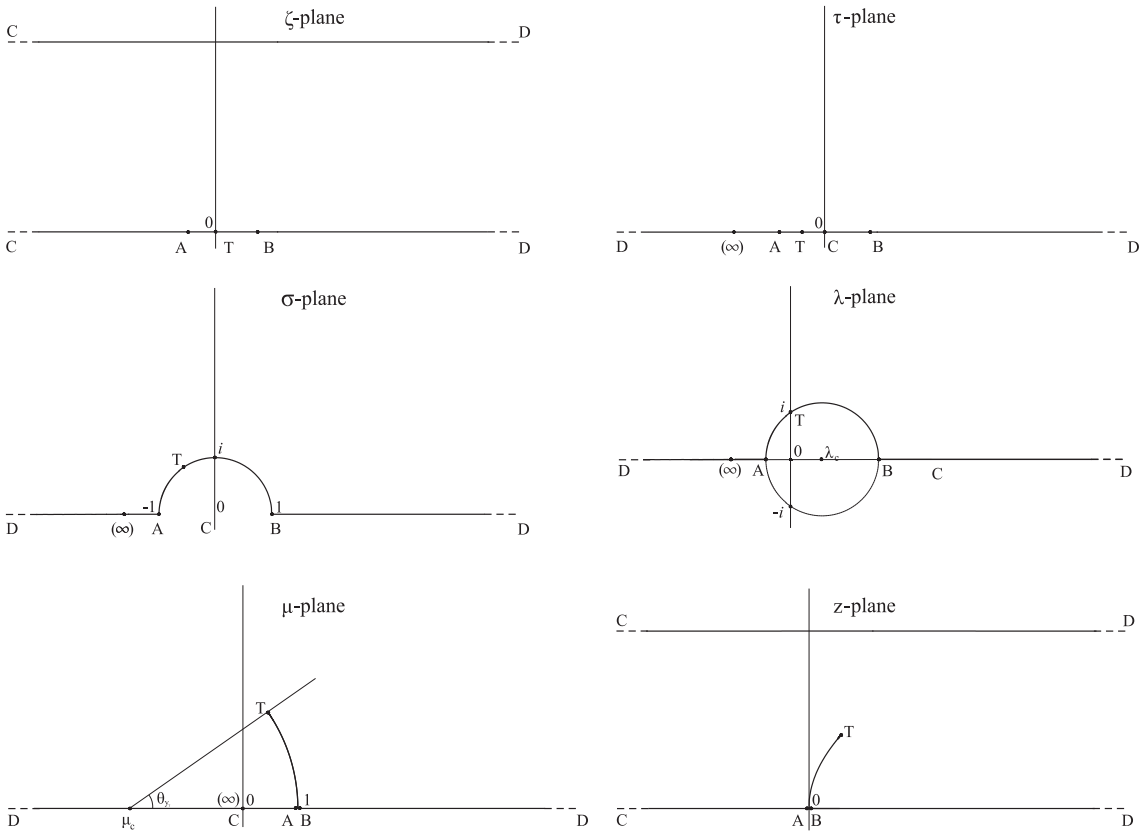

Figure A.1. Mapping chain: $\zeta \rightarrow \tau \rightarrow \sigma \rightarrow \lambda \rightarrow \mu \rightarrow z$ -plane.

where μ'_K is a point in the circle, close to μ_K, $a \in \mathbb{C}^1$, which is determined by enforcing $(\mathrm{d}\lambda/\mathrm{d}\mu)_{\mu_K} = 0$. The region outside the unit circle is mapped onto the upper half-χ-plane by means of a bilinear mapping

$$\chi = \frac{c\mu + d}{\mu + e},$$

where the three coefficients c,d,e are determined by imposing the three conditions $\mu(\infty) = -\mathrm{i}$, $\mu(0) = \mu_K$, $\mu(\chi_B + \chi_s) = \mathrm{i}$ and χ_s is a real parameter which defines the width of the region ABCD. The first condition associates the point Q in the μ-plane with the point at infinity on the χ-plane. χ_A and χ_B are two free parameters that define the boundaries of the common line ∂_c on the solid wall. By means of the following simple mapping A and B are moved respectively to -1 and 1

$$\chi = c_1\sigma + c_2.$$

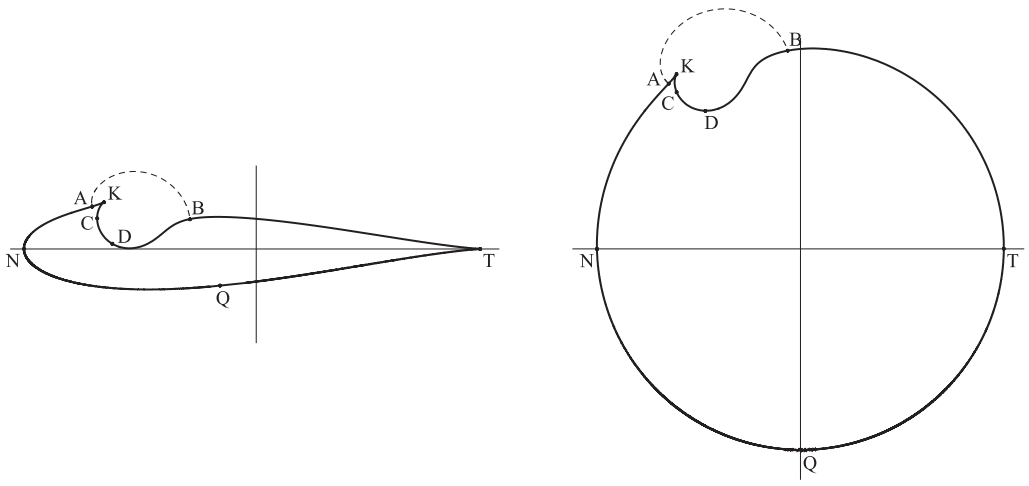

Figure A.2. z-plane (left) and λ-plane (right).

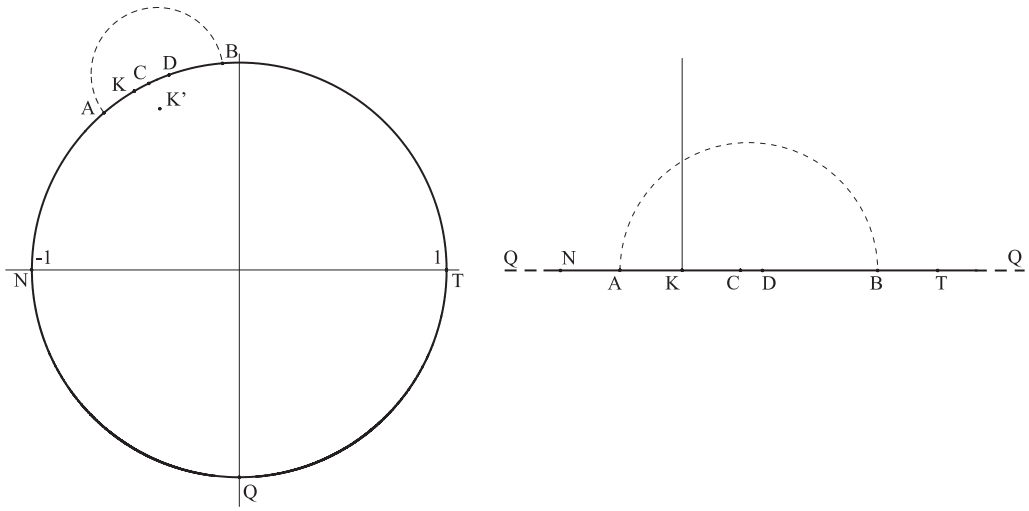

Figure A.3. μ-plane (left) and χ-plane (right).

In figure A.4, the σ-plane is shown. σ_∞ is the image of the infinity in the physical plane. The separatrix between the outer region and the inner region is traced as an half unit circle here. The Jacobi elliptic sine-amplitude function 2.26 maps the unit circle onto the rectangle in the ζ-plane (figure A.4).

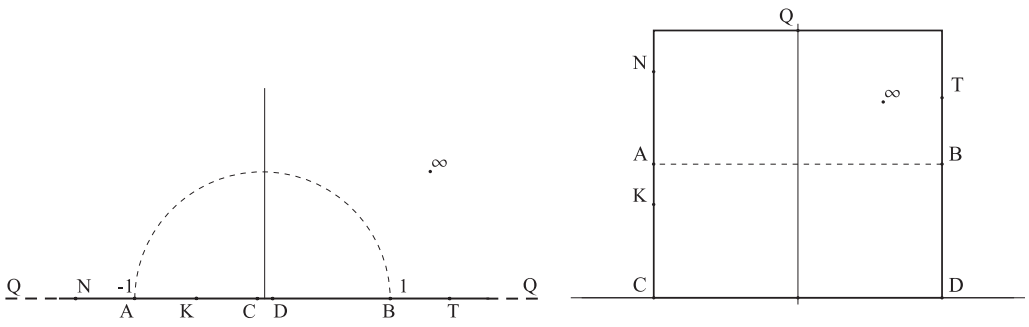

Figure A.4. σ-plane (left) and ζ-plane (right).

Finally the relation between the doublet momentum M and the physical asymptotic flow velocity is taken into account. The equation 2.49 yields the following formula

$$M = q_\infty \mathrm{e}^{-\mathrm{i}\alpha} \frac{2Ac_1}{(\delta + \lambda_N - \lambda_T)\tau}(ec - d).$$

A.1.3 Wind turbine vortex-capturing blade section

According to the Riemann mapping theorem, the airfoil can be conformally mapped from the physical complex z-plane onto the unit circle of the transformed ζ-plane by an analytical $\zeta = \zeta(z)$ where $\lim_{z\to\infty} \zeta(z) = \infty$. The blade section designed for the vertical axis turbine is determined by the following mapping chain that transforms the unit circle in the ζ-plane onto the airfoil in the z-plane. The sequence is shown in figure A.5.

The position of the cusps is defined by the points K and K*, where $(\cdot)^*$ represents the complex conjugation. The unit circle is then mapped onto a quasi-circle in the λ-plane by means of a variation on the Ringleb's mapping

$$\lambda(\zeta) = \zeta + \frac{a}{\zeta - \zeta_{K_1}} + \frac{a^*}{\zeta - \zeta_{K_1^*}}$$

where a,$a^* \in \mathbb{C}^1$, ζ_{K_1} and $\zeta_{K_1^*}$ are two points within the circle and close to the images ζ_K, ζ_{K^*} of the cusps. The coefficients are computed by enforcing the singularities in K, K*, that is $(\mathrm{d}\lambda/\mathrm{d}\zeta)_{\zeta_K} = (\mathrm{d}\lambda/\mathrm{d}\zeta)_{\zeta_{K^*}} = 0$. The point T identifies the position of the airfoil's trailing edge. The airfoil is generated on the intermediate z_1-plane by the Kármán-Trefftz mapping

$$\frac{z_1 - 1}{z_1 + 1} = \left(\frac{\lambda - \lambda_T}{\lambda - (\lambda_N + \delta)}\right)^\tau, \quad \tau = \frac{2\pi - \epsilon}{\pi}$$

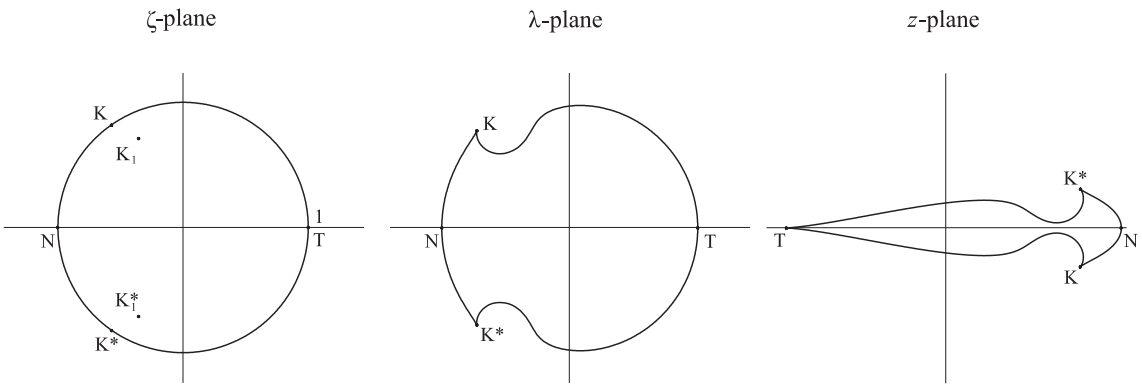

Figure A.5. Mapping sequence for a trapping vortex blade section. $\zeta_K = \exp(\mathrm{i}\ 1.175)$ and $\zeta_{K_1} = 0.93\exp(\mathrm{i}\ 1.05)$.

where ϵ is the trailing edge angle, λ_T and λ_N are the images on the λ-plane of the trailing and leading edge T, N and $\lambda_N + \delta$ is a point close to the nose. A final scale factor $A = z_{1,N} - z_{1,T}$ transforms and overturns the airfoil in z_1-plane on the unit chord profile on the physical z-plane

$$z = z_1/A$$

The mapping chain $z = z\{z_1[\lambda(\zeta)]\}$ depends on the choice of the four parameters ϵ, ζ_{K_1}, ζ_K, δ that allows a wide family of symmetrical airfoils to be generated.

A.1.4 Airfoil with a flap

In this section we illustrate two conformal mappings. The first map allows to transform two circles onto a couple of airfoils and it is a derivation of the biplane section studied by Ferrari (1930) [23]. The second map transforms the region outside of two circles onto the region inside a rectangle.

Let us consider two circles of the complex ν-plane, as shown in figure A.6. The main circle (m) is unit and centred at the origin, while the secondary circle (s) is located in $(x_s,\, 0)$ and the radius is r_s. The secondary element can be mapped onto an airfoil, while the main circle remains the same, mapped by

$$\frac{\lambda - \lambda_{T_s}}{\lambda - \lambda_{N_s}} \frac{\lambda - 1/\lambda^*_{T_s}}{\lambda - 1/\lambda^*_{N_s}} = \left(\frac{\nu - \nu_{T_s}}{\nu - \nu_{N_s}} \frac{\nu - 1/\nu^*_{T_s}}{\nu - 1/\nu^*_{N_s}} \right)^{\tau_s},$$

where ν_{T_s} is located on the secondary circle and represents the trailing edge, ν_{N_s} is inside the circle and $\tau_s = (2\pi - \epsilon_s)/\pi$ with ϵ_s as trailing edge angle. The parameters

λ_{T_s} and λ_{N_s} can be found by regularity conditions of the mapping. The λ_2-plane is obtained by means of the following scaling/translation

$$\lambda_2 = \lambda_1(1 - z_c) + z_c$$

where $\lambda_1 = \lambda e^{i\beta}$ is the λ-plane rotated by β. In the λ_2-plane, the main circle is centred in z_c and is scaled such that it crosses the point $\lambda_2 = 1$ at T_m. The inner point z_c defines the camber and the thickness of the main airfoil. Indeed, the last mapping transforms the main circle onto a Kármán-Trefftz airfoil and the secondary element onto the final shape of the flap in the physical z-plane

$$\frac{z-1}{z+1} = \left(\frac{\lambda_2 - 1}{\lambda_2 + 1}\right)^{\tau_m}$$

where $\tau_m = (2\pi - \epsilon_m)/\pi$ with being ϵ_m the trailing edge angle.

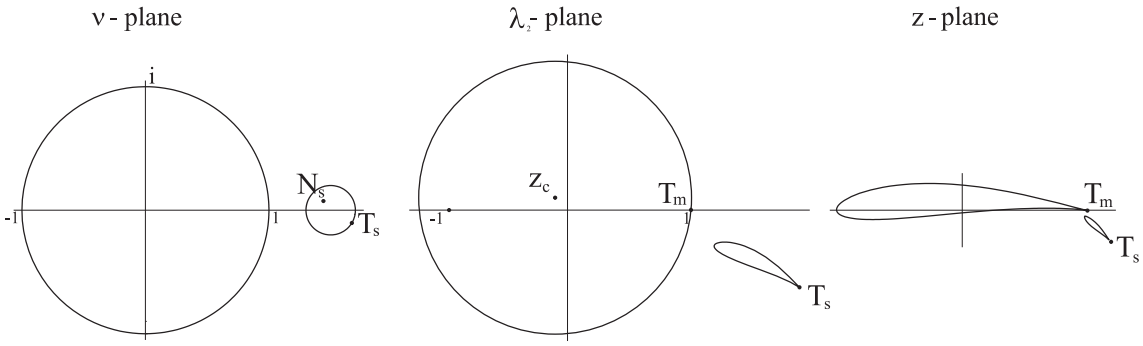

Figure A.6. Mapping sequence to map two circles onto an airfoil with a flap.

The second mapping sequence is displayed in figure A.7. Since the circles of the ν-plan are two members of a family of Apollonius circles, we can determinate the foci $d+c$, $d-c$ by means of the formulas $d = \left(x_s^2 - r_s^2 + 1\right)/2x_s$ and $c = \sqrt{(x_s - d)^2 - r_s^2}$ (see [23]).

The circles are translating and scaled such that the foci are located in $\nu_1 = \pm 1$, by means of the mapping $\nu_1 = (\nu - d)/c$. The Möbius mapping

$$\mu = \frac{\nu_1 + 1}{\nu_1 - 1}$$

maps the region outside the two circles onto the region included between two concentric circles on the μ-plane. The external circle with radius $\rho_s > 1$ corresponds to

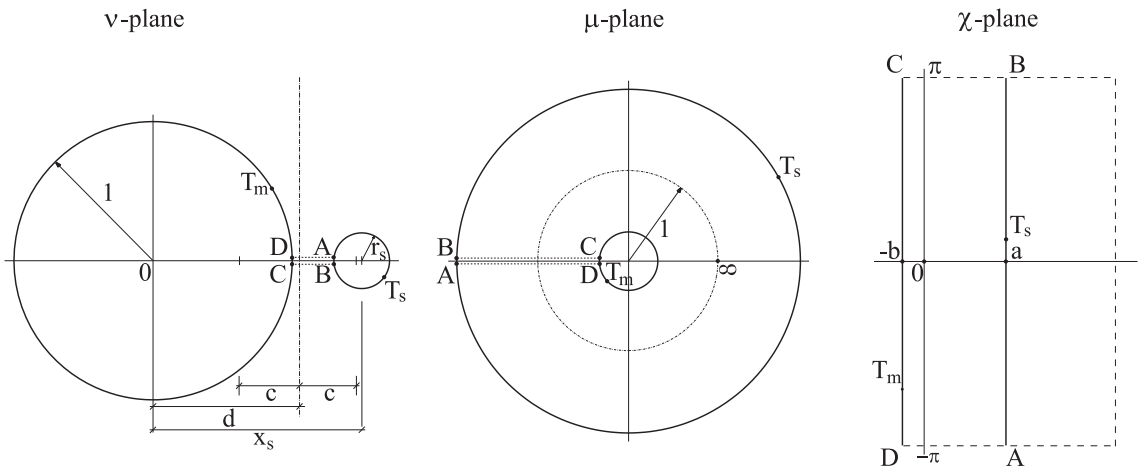

Figure A.7. Mapping sequence to map the region outside two circles onto a rectangle.

the secondary airfoil, while the circle $\rho_m < 1$ is the image of the main airfoil. On the μ-plane, the image of the physical infinity is in the point $\mu = 1$. The final map

$$\chi = \log(\mu)$$

transforms the annulus into the rectangle with boundaries $[-b,\, a] \times [-\pi,\pi]$, where $b = -\log(\rho_m)$ and $a = \log(\rho_s)$.

The mapping chain $\chi \rightarrow z$ allows to map the left boundary CD of the rectangle onto the main circle (m) and the right boundary AB onto the secondary circle (s), while the origin on the χ-plane is the image of the physical infinity. The horizontal boundaries of the rectangle AD and BC are periodic and correspond to a line connecting the airfoils in the z-plane.

A.2 Mathematical derivations

A.2.1 Kutta condition

The deduction of the Kutta condition generically applied in the blob vortex method is presented here. Let us define $z = x + \mathrm{i}y$, $\zeta = \rho \mathrm{e}^{\mathrm{i}\phi}$ and $x = x(\rho,\phi)$, $y = y(\rho,\phi)$. The Kutta condition is satisfied when the relative velocity is not singular at the cusp, that is $(\partial\psi_r/\partial\rho)_{\rho=1} = 0$ in the transformed ζ-plane. Therefore the Kutta condition can be expanded into

$$(\partial\psi_r/\partial\rho)_{\rho=1} = \left(\frac{\partial\psi_r}{\partial x}\frac{\partial x}{\partial\rho} + \frac{\partial\psi_r}{\partial y}\frac{\partial y}{\partial\rho}\right)_{\rho=1} = 0 \tag{A.1}$$

where $\partial\psi_r/\partial y$ and $-\partial\psi_r/\partial x$ are the components of the relative velocity in the physical plane. The following identity is obtained by the Cauchy-Riemann conditions

$$\frac{\mathrm{d}z}{\mathrm{d}\zeta}\mathrm{e}^{\mathrm{i}\phi} = \frac{\partial x}{\partial\rho} + \mathrm{i}\frac{\partial y}{\partial\rho}$$

and it can be used in the expression

$$(u - \mathrm{i}v)\frac{\mathrm{d}z}{\mathrm{d}\zeta}\mathrm{e}^{\mathrm{i}\phi} = \left(u\frac{\partial x}{\partial\rho} + v\frac{\partial y}{\partial\rho}\right) + \mathrm{i}\left(u\frac{\partial y}{\partial\rho} - v\frac{\partial x}{\partial\rho}\right).$$

Now the equation A.1 can be replaced by

$$\mathrm{Im}\left[(u_r - \mathrm{i}v_r)\,\frac{\mathrm{d}z}{\mathrm{d}\zeta}\mathrm{e}^{\mathrm{i}\phi}\right] = 0$$

where $(u_r - \mathrm{i}v_r) = \mathrm{d}w/\mathrm{d}z - (u_t - \mathrm{i}v_t)$ and $(\cdot)_t$ indicates the transport component of the velocity. By taking into account that $\mathrm{d}w/\mathrm{d}z = (\mathrm{d}w/\mathrm{d}\zeta)/(\mathrm{d}z/\mathrm{d}\zeta)$, the Kutta condition is

$$\mathrm{Im}\left\{\left[\frac{\mathrm{d}w}{\mathrm{d}\zeta} - (u_t - \mathrm{i}v_t)\,\frac{\mathrm{d}z}{\mathrm{d}\zeta}\right]\mathrm{e}^{\mathrm{i}\phi}\right\} = 0$$

and, since in the cusp $(\mathrm{d}z/\mathrm{d}\zeta)_{\zeta_{E_i}} = 0$, we obtain

$$\mathrm{Im}\left[\frac{\mathrm{d}w}{\mathrm{d}\zeta}\mathrm{e}^{\mathrm{i}\phi}\right]_{\zeta_{E_i}} = 0. \tag{A.2}$$

A.2.2 Circulation time derivatives in the low order model

The linear system to compute the time derivatives $\dot{\gamma}_m$, $\dot{\gamma}_s$, $\dot{\kappa}$ is addressed here. Let us consider the linear system discussed in 3.1.3, where the strengths of the arising point vortices and $\kappa(t)$ are determined by enforcing the Kutta condition at two trailing edges and by applying the Kelvin theorem around a profile. In [48] this linear system is devised for the two-blade VAT and it is reported subsequently. By referring to figure 3.13, the Kutta conditions and the Kelvin theorem around the blade section m are imposed by the equations

$$\mathrm{Im}\left(\frac{\mathrm{d}w}{\mathrm{d}\chi}\right)_{\chi_{T,m}} = 0, \;\; \mathrm{Im}\left(\frac{\mathrm{d}w}{\mathrm{d}\chi}\right)_{\chi_{T,s}} = 0, \;\; w_C - w_D = -\sum_{j_m=1}^{N} \gamma_{j_m}$$

where j_m indicates the point vortices shed by the m blade. These equations form a 3×3 linear system $Ax = b$, where the vector of the unknowns is $x^T = (\gamma_m,\gamma_s,\kappa)$. By exploiting the quasi-periodic properties of the Weierstrass elliptic functions (see 3.1.3) the coefficients $a_{i,j}$ of the matrix A are

$$\begin{aligned}
a_{1,1} &= \mathrm{Im}\left\{\frac{1}{2\pi\mathrm{i}}\left[\zeta\left(\chi_{T,m} - \chi_{V,m}\right) - \zeta\left(\chi_{T,m} + \chi^*_{V,m} - \omega\right)\right]\right\} \\
a_{1,2} &= \mathrm{Im}\left\{\frac{1}{2\pi\mathrm{i}}\left[\zeta\left(\chi_{T,m} - \chi_{V,s}\right) - \zeta\left(\chi_{T,m} + \chi^*_{V,s} - \omega\right)\right]\right\} \\
a_{1,3} &= 1 \\
a_{2,1} &= \mathrm{Im}\left\{\frac{1}{2\pi\mathrm{i}}\left[\zeta\left(\chi_{T,s} - \chi_{V,m}\right) - \zeta\left(\chi_{T,s} + \chi^*_{V,m} - \omega\right)\right]\right\} \\
a_{2,2} &= \mathrm{Im}\left\{\frac{1}{2\pi\mathrm{i}}\left[\zeta\left(\chi_{T,s} - \chi_{V,s}\right) - \zeta\left(\chi_{T,s} + \chi^*_{V,s} - \omega\right)\right]\right\} \\
a_{2,2} &= 1 \\
a_{3,1} &= \frac{\eta'}{\pi\mathrm{i}}\left[2\ \mathrm{Re}\left(\chi_{V,m}\right) - \omega\right] - 1 \\
a_{3,2} &= \frac{\eta'}{\pi\mathrm{i}}\left[2\ \mathrm{Re}\left(\chi_{V,s}\right) - \omega\right] \\
a_{3,3} &= 2\pi
\end{aligned}$$

and the right-hand side vector $b^T = (b_1, b_2, b_3)$

$$
\begin{aligned}
b_1 =& -\operatorname{Im}\left[-Q_\infty^* \wp\left(\chi_{T,m}\right) + Q_\infty \wp\left(\chi_{T,m}+\omega\right) + \left(\frac{\mathrm{d}w_2}{\mathrm{d}\chi}\right)_{\chi_{T,m}}\right] \\
&+ \operatorname{Im}\left\{\frac{1}{2\pi \mathrm{i}} \sum_{j=1}^{N-2} \gamma_j \left[\zeta\left(\chi_{T,m}-\chi_j\right) - \zeta\left(\chi_{T,m}+\chi_j^*-\omega\right)\right]\right\} \\
b_2 =& -\operatorname{Im}\left[-Q_\infty^* \wp\left(\chi_{T,s}\right) + Q_\infty \wp\left(\chi_{T,s}+\omega\right) + \left(\frac{\mathrm{d}w_2}{\mathrm{d}\chi}\right)_{\chi_{T,s}}\right] \\
&+ \operatorname{Im}\left\{\frac{1}{2\pi \mathrm{i}} \sum_{j=1}^{N-2} \gamma_j \left[\zeta\left(\chi_{T,s}-\chi_j\right) - \zeta\left(\chi_{T,s}+\chi_j^*-\omega\right)\right]\right\} \\
b_3 =& -4\mathrm{i}\eta' \operatorname{Im}\left(Q_\infty\right) - \frac{\eta'}{\pi \mathrm{i}} \sum_{j=1}^{N-2} \gamma_j \left[2\ \operatorname{Re}\left(\chi_j\right) - \omega\right] + \sum_{j_m=1}^{N_m-1} \gamma_{j_m}
\end{aligned}
$$

where N is the number of the shed point vortex, and N_m is the number of the point vortex released by the m profile. By deriving in time the above linear system, we obtain

$$
\begin{aligned}
a_{1,1}\dot{\gamma}_m + a_{1,2}\dot{\gamma}_s + a_{1,3}\dot{\kappa} &= \dot{b_1} - \dot{a}_{1,1}\gamma_m - \dot{a}_{1,2}\gamma_s - \dot{a}_{1,3}\kappa \\
a_{2,1}\dot{\gamma}_m + a_{2,2}\dot{\gamma}_s + a_{2,3}\dot{\kappa} &= \dot{b_2} - \dot{a}_{2,1}\gamma_m - \dot{a}_{2,2}\gamma_s - \dot{a}_{2,3}\kappa \\
a_{3,1}\dot{\gamma}_m + a_{3,2}\dot{\gamma}_s + a_{3,3}\dot{\kappa} &= \dot{b_3} - \dot{a}_{3,1}\gamma_m - \dot{a}_{3,2}\gamma_s - \dot{a}_{3,3}\kappa
\end{aligned}
\tag{A.3}
$$

Since the frame of reference is fixed on the axis and rotates jointly with the blades, the time dependent variables are $\chi_{V,s}$, $\chi_{V,m}$, χ_j, Q_∞ and the complex conjugates

$\chi^*_{V,s}$, $\chi^*_{V,m}$, χ^*_j, Q^*_∞. The derivation in time of the matrix coefficients $a_{i,j}$ yields

$$\begin{aligned}
\dot{a}_{1,1} &= \mathrm{Im}\left\{\frac{1}{2\pi\mathrm{i}}\left[\wp\left(\chi_{T,m}-\chi_{V,m}\right)\dot{\chi}_{V,m}+\wp\left(\chi_{T,m}+\chi^*_{V,m}-\omega\right)\dot{\chi}^*_{V,m}\right]\right\}\\
\dot{a}_{1,2} &= \mathrm{Im}\left\{\frac{1}{2\pi\mathrm{i}}\left[\wp\left(\chi_{T,m}-\chi_{V,s}\right)\dot{\chi}_{V,s}+\wp\left(\chi_{T,m}+\chi^*_{V,s}-\omega\right)\dot{\chi}^*_{V,s}\right]\right\}\\
\dot{a}_{1,3} &= 0\\
\dot{a}_{2,1} &= \mathrm{Im}\left\{\frac{1}{2\pi\mathrm{i}}\left[\wp\left(\chi_{T,s}-\chi_{V,m}\right)\dot{\chi}_{V,m}+\wp\left(\chi_{T,s}+\chi^*_{V,m}-\omega\right)\dot{\chi}^*_{V,m}\right]\right\}\\
\dot{a}_{2,2} &= \mathrm{Im}\left\{\frac{1}{2\pi\mathrm{i}}\left[\wp\left(\chi_{T,s}-\chi_{V,s}\right)\dot{\chi}_{V,s}+\wp\left(\chi_{T,s}+\chi^*_{V,s}-\omega\right)\dot{\chi}^*_{V,s}\right]\right\}\\
\dot{a}_{2,2} &= 0\\
\dot{a}_{3,1} &= \frac{2\eta'}{\pi\mathrm{i}}\mathrm{Re}\left(\dot{\chi}_{V,m}\right)\\
\dot{a}_{3,2} &= \frac{2\eta'}{\pi\mathrm{i}}\mathrm{Re}\left(\dot{\chi}_{V,s}\right)\\
\dot{a}_{3,3} &= 0
\end{aligned} \tag{A.4}$$

and the right-hand side

$$\begin{aligned}
\dot{b}_1 =& -\mathrm{Im}\left[-\frac{\mathrm{d}Q^*_\infty}{\mathrm{d}t}\wp\left(\chi_{T,m}\right)+\frac{\mathrm{d}Q_\infty}{\mathrm{d}t}\wp\left(\chi_{T,m}+\omega\right)\right]\\
&+\mathrm{Im}\left\{\frac{1}{2\pi\mathrm{i}}\sum_{j=1}^{N-2}\gamma_j\left[\wp\left(\chi_{T,m}-\chi_j\right)\dot{\chi}_j+\wp\left(\chi_{T,m}+\chi^*_j-\omega\right)\dot{\chi}^*_j\right]\right\}\\
\dot{b}_2 =& -\mathrm{Im}\left[-\frac{\mathrm{d}Q^*_\infty}{\mathrm{d}t}\wp\left(\chi_{T,s}\right)+\frac{\mathrm{d}Q_\infty}{\mathrm{d}t}\wp\left(\chi_{T,s}+\omega\right)\right]\\
&+\mathrm{Im}\left\{\frac{1}{2\pi\mathrm{i}}\sum_{j=1}^{N-2}\gamma_j\left[\wp\left(\chi_{T,s}-\chi_j\right)\dot{\chi}_j+\wp\left(\chi_{T,s}+\chi^*_j-\omega\right)\dot{\chi}^*_j\right]\right\}\\
\dot{b}_3 =& -4\mathrm{i}\eta'\mathrm{Im}\left(\frac{\mathrm{d}Q_\infty}{\mathrm{d}t}\right)-\frac{\eta'}{\pi\mathrm{i}}\sum_{j=1}^{N-2}\gamma_j\left[2\ \mathrm{Re}\left(\dot{\chi}_j\right)\right].
\end{aligned} \tag{A.5}$$

where $\dot{\chi}_{V,m}$, $\dot{\chi}_{V,s}$, $\dot{\chi}_j$ are the relative point vortex velocities on the χ-plane.

As discussed in section 3.1.4, the Brown & Michael velocity correction for a point vortex with a variable strength is

$$\dot{z}^*_V = z'^*_V - \frac{\dot{\gamma}_V}{\gamma_V}\left(z_V - z_T\right)^* \tag{A.6}$$

where z'_V is the velocity for a point vortex of constant strength, determined by the Routh rule (see the equation 3.6). Being $q_T = \mathrm{i}\,\Omega z$ the transfer velocity of the frame of reference, the complex conjugate of the relative velocity on the physical plane is determined by

$$\dot{z^*_{r,V}} = \dot{z}^*_V - q^*_T. \tag{A.7}$$

By exploiting the chain rule $\frac{\mathrm{d}z}{\mathrm{d}t} = \frac{\mathrm{d}z}{\mathrm{d}\chi}\frac{\mathrm{d}\chi}{\mathrm{d}t}$ and replacing in A.6, the relative velocity of the variable intensity point vortex becomes

$$\dot{\chi}^*_V = A_V - \dot{\gamma}_V B_V \tag{A.8}$$

where

$$\begin{aligned} A_V =& \left(\chi'^* - \frac{\gamma}{4\pi\mathrm{i}}\frac{\mathrm{d}^2 z/\mathrm{d}\chi^2}{\mathrm{d}z/\mathrm{d}\chi}\right)_V \frac{1}{J_V} + \frac{\mathrm{i}\Omega z^*}{(\mathrm{d}z/\mathrm{d}\chi)^*} \\ B_V =& \frac{\dot{\gamma}_V}{\gamma_V}\frac{(z_V - z_T)^*}{(\mathrm{d}z/\mathrm{d}\chi)^*}. \end{aligned}$$

This definition can be used in the equations A.4 and A.5 in order to replace $\dot{\chi}_{V,m}$, $\dot{\chi}_{V,s}$, $\dot{\chi}_j$. Finally the linear system A.3 becomes

$$\begin{aligned} &(a_{1,1} - \alpha_{1,1}\gamma_m)\,\dot{\gamma}_m + (a_{1,2} - \beta_{1,1}\gamma_s)\,\dot{\gamma}_s + a_{1,3}\dot{\kappa} = \dot{b_1} - \alpha_{1,2}\gamma_m - \beta_{1,2}\gamma_s \\ &(a_{2,1} - \alpha_{2,1}\gamma_m)\,\dot{\gamma}_m + (a_{2,2} - \beta_{2,1}\gamma_s)\,\dot{\gamma}_s + a_{2,3}\dot{\kappa} = \dot{b_2} - \alpha_{1,2}\gamma_m - \beta_{2,2}\gamma_s \\ &(a_{3,1} - \alpha_{3,1}\gamma_m)\,\dot{\gamma}_m + (a_{3,2} - \beta_{3,1}\gamma_s)\,\dot{\gamma}_s + a_{3,3}\dot{\kappa} = \dot{b_3} - \alpha_{1,3}\gamma_m - \beta_{3,2}\gamma_s \end{aligned} \tag{A.9}$$

where

$$\begin{aligned} \alpha_{1,1} =& \mathrm{Im}\left\{\frac{1}{2\pi\mathrm{i}}\left[\wp\left(\chi_{T,m} - \chi_{V,m}\right)B^*_{V_m} + \wp\left(\chi_{T,m} + \chi^*_{V,m} - \omega\right)B_{V_m}\right]\right\} \\ \alpha_{1,2} =& \mathrm{Im}\left\{\frac{1}{2\pi\mathrm{i}}\left[\wp\left(\chi_{T,m} - \chi_{V,m}\right)A^*_{V_m} + \wp\left(\chi_{T,m} + \chi^*_{V,m} - \omega\right)A_{V_m}\right]\right\} \\ \alpha_{2,1} =& \mathrm{Im}\left\{\frac{1}{2\pi\mathrm{i}}\left[\wp\left(\chi_{T,s} - \chi_{V,m}\right)B^*_{V_m} + \wp\left(\chi_{T,s} + \chi^*_{V,m} - \omega\right)B_{V_m}\right]\right\} \\ \alpha_{2,2} =& \mathrm{Im}\left\{\frac{1}{2\pi\mathrm{i}}\left[\wp\left(\chi_{T,s} - \chi_{V,m}\right)A^*_{V_m} + \wp\left(\chi_{T,s} + \chi^*_{V,m} - \omega\right)A_{V_m}\right]\right\} \\ \alpha_{3,1} =& \frac{2\eta'}{\pi\mathrm{i}}\mathrm{Re}\left(B^*_{V_m}\right) \\ \alpha_{3,2} =& \frac{2\eta'}{\pi\mathrm{i}}\mathrm{Re}\left(A^*_{V_m}\right) \end{aligned}$$

$$\beta_{1,1} = \mathrm{Im}\left\{\frac{1}{2\pi \mathrm{i}}\left[\wp\left(\chi_{T,m}-\chi_{V,s}\right)B^*_{V_s}+\wp\left(\chi_{T,m}+\chi^*_{V,s}-\omega\right)B_{V_s}\right]\right\}$$

$$\beta_{1,2} = \mathrm{Im}\left\{\frac{1}{2\pi \mathrm{i}}\left[\wp\left(\chi_{T,m}-\chi_{V,s}\right)A^*_{V_s}+\wp\left(\chi_{T,m}+\chi^*_{V,s}-\omega\right)A_{V_s}\right]\right\}$$

$$\beta_{2,1} = \mathrm{Im}\left\{\frac{1}{2\pi \mathrm{i}}\left[\wp\left(\chi_{T,s}-\chi_{V,s}\right)B^*_{V_s}+\wp\left(\chi_{T,s}+\chi^*_{V,s}-\omega\right)B_{V_s}\right]\right\}$$

$$\beta_{2,2} = \mathrm{Im}\left\{\frac{1}{2\pi \mathrm{i}}\left[\wp\left(\chi_{T,s}-\chi_{V,s}\right)A^*_{V_s}+\wp\left(\chi_{T,s}+\chi^*_{V,s}-\omega\right)A_{V_s}\right]\right\}$$

$$\beta_{3,1} = \frac{2\eta'}{\pi \mathrm{i}}\mathrm{Re}\left(B^*_{V_s}\right)$$

$$\beta_{3,2} = \frac{2\eta'}{\pi \mathrm{i}}\mathrm{Re}\left(A^*_{V_s}\right)$$

If a new vortex whose the intensity is lower than the prescribed threshold is going to be generated, the vortex is not shed up to the next evaluation and the flow field is characterized by a single vortex with variable intensity. Therefore, the size of the problem A.3 is reduced to two unknowns, thus it forms a 2×2 linear system.

A.2.3 Sign of the penalization term

Let us consider the incompressible penalized Navier Stokes equation 3.44. In the solid bodies the penalization term is greater than the other members of the equation, such that it tends to enforce $\mathbf{u} = \bar{\mathbf{u}}$. It is important to notice that the penalization term cannot to be defined as $\lambda\chi_{S(t)}(\mathbf{u} - \bar{\mathbf{u}})$.

Since for $\lambda \gg 1$ within the solid region $S(t)$ the convective, diffusive and pressure terms are negligible, that is, the penalized Navier-Stokes equation becomes

$$\frac{\partial \mathbf{u}}{\partial t} = \lambda(\bar{\mathbf{u}} - \mathbf{u}). \tag{A.10}$$

For the sake of simplicity, this equation can be reduced in terms of a one-dimensional dynamical system

$$\ddot{x} = \lambda(\bar{u} - \dot{x}).$$

We replace $\dot{y} = \pm(\dot{x} - \bar{u})$ in order to study the sign of the right-hand side, and the equation becomes

$$\ddot{y} = \mp\lambda\dot{y}. \tag{A.11}$$

The general solution of equation A.11 is then $y = a_0 \mathrm{e}^{\mp\lambda t} + b_0$ where a_0, b_0 are the constants determined by the initial and boundary conditions. Therefore the solution is stable only for the replacement $\dot{y} = \dot{x} - \bar{u}$.

A.2.4 Mollified step function

The step characteristic function has to be defined such that the signed distance function $\phi < 0$ inside the solid body and $\phi > 0$ outside (see [47]). Being $\epsilon = \max(\Delta x, \Delta y)$, a smoothed step function can be defined as

$$H(\phi) = \begin{cases} 1 & \text{if } \phi < -\epsilon \\ \frac{1}{2} - \frac{\phi}{2\epsilon} - \frac{1}{2\pi}\sin\left(\frac{\pi\phi}{\epsilon}\right) & \text{if } -\epsilon \leq \phi \leq \epsilon \\ 0 & \text{if } \phi > \epsilon \end{cases}$$

and its analytic derivative yields the related smoothed delta function

$$\delta(\phi) = \begin{cases} 0 & \text{if } \phi < -\epsilon \\ -\frac{1}{2\epsilon} - \frac{1}{2\epsilon}\cos\left(\frac{\pi\phi}{\epsilon}\right) & \text{if } -\epsilon \leq \phi \leq \epsilon \\ 0 & \text{if } \phi > \epsilon \end{cases}$$

The parameter ϵ establishes the extent of the band where the step is smeared.

A.2.5 Impulse and force exerted on a vortex immersed in a stream

With the aim of applying the hydrodynamic impulse theory to compute the forces and the moments of a vortex system, a more than trivial example is illustrated here.

Let us consider a 2D incompressible inviscid and irrotational flow. The flow field is described on the complex plane $z = x + \mathrm{i}y$ by means of the potential flow model with vortex singularities immersed within. A vortex singularity with strength γ_v and location z_v is placed in a free constant stream q_∞. The complex potential w is

$$w = q_\infty z + \frac{\gamma_v}{2\pi\mathrm{i}}\log(z - z_v)$$

and the conjugate vortex velocity is determined by the complex velocity without the self-induction part, namely

$$\dot{z}_v^* = \left(\frac{\mathrm{d}w}{\mathrm{d}z}\right) - \frac{\gamma}{2\pi\mathrm{i}}\frac{1}{z - z_v} = q_\infty$$

where $(\cdot)^*$ indicates the complex conjugate. The result is trivial, that is the point vortex is transported by the free stream and moves with q_∞.

Following Saffman (1992) [62], the 2D linear hydrodynamic impulse is defined by $\mathbf{I} = \int \omega\ \mathbf{x} \wedge \mathbf{k}\ \mathrm{d}S$, and for a vortex singularity it becomes $\mathbf{I} = \gamma\ \mathbf{x} \wedge \mathbf{k}$. Since the impulse is an invariant of the flow only if the velocity, the vorticity and the external forces vanish at infinity, we apply a Galileian transformation and the frame of reference is transported downstream with q_∞, so that the infinity is at rest. In

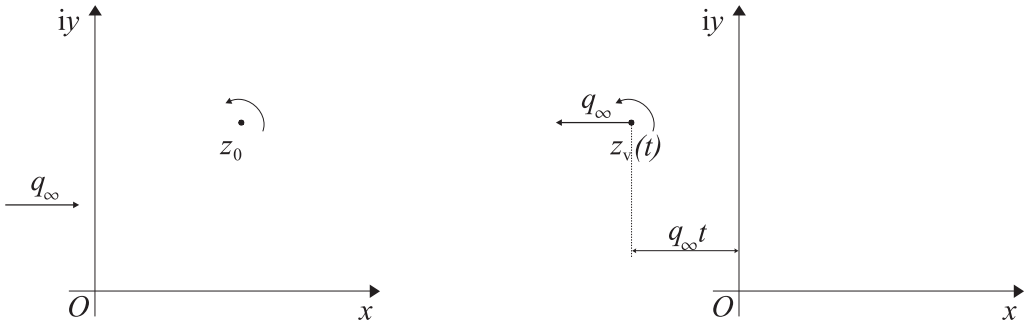

Figure A.8. Galileian transformation to define the impulse. The point vortex immersed in the free stream q_∞ (left) is equivalent to the point vortex that moves backward with velocity $-q_\infty$ (right).

this new frame of reference the point vortex does not move, its linear impulse does not vary in time, therefore no forces are exerted on the vortex.

Now let us take in consideration a 'whisk', that is a point vortex γ_v embedded in the location z_v, immersed in the free stream q_∞. Another Galileian transformation is applied such that in the new frame of reference the velocity at infinity is null and the linear impulse represents an invariant of the flow (see figure A.8). If $z_v(t) = x_v(t) + \mathrm{i}y_v(t)$ and $z_v(0) = x_0 + \mathrm{i}y_0$, the Galileian transformation is

$$x_v(t) = x_0 - q_\infty t, \quad y_v(t) = y_0$$

and describes the motion of the constrained vortex with a constant velocity $-q_\infty$. Therefore the linear impulse is

$$I_x = \gamma_v \; y_0, \quad I_y = -\gamma_v \; (x_0 - q_\infty t)$$

and the force on the 'whisk' is obtained by $\mathbf{F} = -\mathrm{d}\mathbf{I}/\mathrm{d}t$

$$F_x = 0, \quad F_y = -\gamma_v \; q_\infty$$

that corresponds with the well-known *Magnus' effect*.

A.2.6 Forces and torque exerted by the fluid on a rotating and translating ellipse

The impulse theory is applied here to evaluate the forces and the torque exerted by the fluid on a moving ellipse with a constant rigid rotation and translation.

This application is meaningful because it represents an analytical validation of the procedure discussed in section 3.1.6. Such a kind of rigid motion is the same as the one described in section 3.1.2 for the single blade.

Let us consider an ellipse rotating with constant angular velocity Ω and immersed in a free stream q_∞. The geometrical setting is illustrated in figure A.9. The flow field is studied by means of the potential flow theory and conformal mappings. Following the section 3.1.2, the complex potential of the flow field is defined on a frame of reference fixed on the body. In particular, the ellipse on the physical z_0-plane can be mapped onto a unit circle on the ζ-plane by the elementary mapping $z_0 = \zeta + \lambda/\zeta$ and, if a point on the circle is identified by $\zeta_B = \mathrm{e}^{\mathrm{i}\phi}$, the corresponding point on the ellipse is $z_{0,B} = (\lambda + 1)\cos\phi + \mathrm{i}(1 - \lambda)\sin\phi$. The complex potential $w = w[z_0(\zeta)]$ is

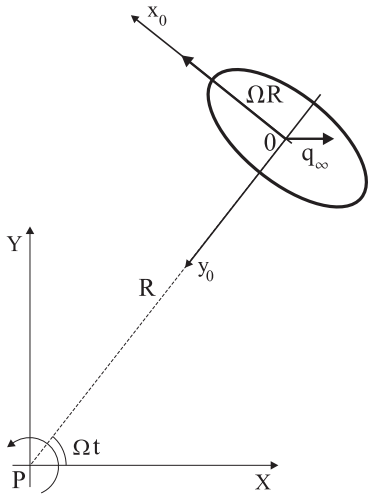

Figure A.9. Sketch of the geometrical setup.

defined on the mapped plane and has to take into account the permeability condition for moving bodies expressed by the equation 3.2. The variable streamfunction on the ellipse contour is given by

$$\psi_B(\phi) = (1 - \lambda)\Omega R \sin\phi - \Omega\lambda\cos^2\phi + \Omega\lambda\sin^2\phi + \psi_{B,0} \tag{A.12}$$

where $\psi_{B,0}$ is a constant that can be taken off. Since $\lim_{\zeta\to\infty}\left|\frac{\mathrm{d}z_0}{\mathrm{d}\zeta}\right| = 1$, the velocities at infinity on the mapped and in the physical planes are equivalent. The complex potential is determined by the equation 3.3 with the conditions that no vortex is generated and that there are no free vortices in the flow. The complex potential is written as

$$w(\zeta) = q_\infty \mathrm{e}^{-\mathrm{i}\beta}\zeta + q_\infty \mathrm{e}^{\mathrm{i}\beta}\frac{1}{\zeta} + \sum_{n=1}^{\infty}(a_n + \mathrm{i}b_n)\,\zeta^{-(n-1)}, \tag{A.13}$$

where $\beta = -(\frac{\pi}{2} + \Omega t)$. By imposing the boundary condition $\mathrm{Im}[w(\mathrm{e}^{\mathrm{i}\phi})] = \psi_B(\phi)$,

the series coefficients are easily determined. All the coefficients are null except

$$a_2 = -(1-\lambda)\Omega R, \qquad b_3 = -\Omega\lambda.$$

Finally the complex potential reads

$$w(\zeta) = \mathrm{i}q_\infty \mathrm{e}^{\mathrm{i}\Omega t}\zeta - \left[\mathrm{i}q_\infty \mathrm{e}^{-\mathrm{i}\Omega t} + (1-\lambda)\Omega R\right]\frac{1}{\zeta} - \mathrm{i}\Omega\lambda\frac{1}{\zeta^2}. \tag{A.14}$$

The dynamical action on the body is only due to the bound vorticity, hence the linear and angular impulses are determinated by means of the relations 3.41. Such equations are valid if the frame of reference is at rest with respect to the infinity, a Galileian transformation has to be introduced. The transformation of coordinates is given by the complex equation

$$z_B = R\mathrm{e}^{\mathrm{i}\Omega t} + z_{0,B}\mathrm{e}^{\mathrm{i}\Omega t + \frac{\pi}{2}} - q_\infty t \tag{A.15}$$

In figure A.10, the trajectory of the ellipse described in the absolute frame of reference z-plane centred in O is illustrated. Following 3.41 the components of the

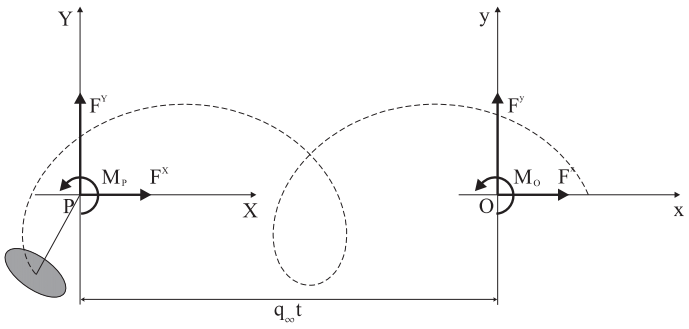

Figure A.10. Galileian transformation.

hydrodynamical impulse become

$$\begin{aligned}
I^x &= -\int_0^{2\pi} \mathrm{Im}\left[\left(\frac{\mathrm{d}w}{\mathrm{d}\zeta} - q_\infty \mathrm{e}^{-\mathrm{i}\alpha}\frac{\mathrm{d}z_0}{\mathrm{d}\zeta}\right)\mathrm{e}^{\mathrm{i}\phi}\right]\; y_B(\phi)\;\mathrm{d}\phi \\
I^y &= \int_0^{2\pi} \mathrm{Im}\left[\left(\frac{\mathrm{d}w}{\mathrm{d}\zeta} - q_\infty \mathrm{e}^{-\mathrm{i}\alpha}\frac{\mathrm{d}z_0}{\mathrm{d}\zeta}\right)\mathrm{e}^{\mathrm{i}\phi}\right]\; x_B(\phi)\;\mathrm{d}\phi \\
A &= \frac{1}{2}\int_0^{2\pi} \mathrm{Im}\left[\left(\frac{\mathrm{d}w}{\mathrm{d}\zeta} - q_\infty \mathrm{e}^{-\mathrm{i}\alpha}\frac{\mathrm{d}z_0}{\mathrm{d}\zeta}\right)\mathrm{e}^{\mathrm{i}\phi}\right]\; (x_B(\phi)^2 + y_B(\phi)^2)\;\mathrm{d}\phi
\end{aligned}$$

and, by integrating on the unit circle contour, finally we have

$$\begin{aligned} I^x =& -\pi\left[(1+\lambda)^2 q_\infty \cos^2\Omega t + (1-\lambda)^2 q_\infty \sin^2\Omega t + (1-\lambda)^2 \Omega R \sin\Omega t\right] \\ I^y =& -\pi\left[(1+\lambda)^2 q_\infty \cos\Omega t \sin\Omega t - (1-\lambda)^2 q_\infty \sin\Omega t \cos\Omega t - (1-\lambda)^2 \Omega R \cos\Omega t\right] \\ A =& \pi\left[2\lambda q_\infty t \sin 2\Omega t - (1-\lambda)^2 q_\infty R(\Omega t \cos\Omega t - \sin\Omega t) + 2\Omega\lambda^2 + 2(1-\lambda)^2 \Omega R^2\right] \end{aligned}$$

Being $\mathbf{F} = -\mathrm{d}\mathbf{I}/\mathrm{d}t$ and $\mathbf{M}_O = -\mathrm{d}\mathbf{A}/\mathrm{d}t$, the forces and the moment with respect to the origin O are

$$\begin{aligned} F^x =& -\pi\left[4\lambda q_\infty \Omega \sin 2\Omega t - (1-\lambda)^2 \Omega^2 R \cos\Omega t\right] \\ F^y =& \quad \pi\left[4\lambda q_\infty \Omega \cos 2\Omega t + (1-\lambda)^2 \Omega^2 R \sin\Omega t\right] \\ M_O =& -\pi q_\infty \left[2\lambda q_\infty \sin 2\Omega t + 4\lambda q_\infty t\Omega \cos 2\Omega t + (1-\lambda)^2 \Omega^2 t R \sin\Omega t\right]. \end{aligned}$$

Since the moment of the force is known on the point O, it can be transferred onto the point P where the centre of the rotation is located. The moment in P is trivially obtained by

$$M_P = M_O + F^y q_\infty t = -2\pi\lambda q_\infty^2 \sin 2\Omega t,$$

while the forces are unvaried, thus $F^X = F^x$, $F^Y = F^y$.

By supposing that the ellipse is a blade section of a vertical axis turbine operating in a potential irrotational flow, the power Π received on the shaft is provided by the scalar products $\Pi = \mathbf{F}\cdot\mathbf{u}_P + \mathbf{M}_P\cdot\boldsymbol{\Omega}_P$, where $\mathbf{u}_P$ and $\boldsymbol{\Omega}_P$ are the linear and angular velocity of the point P where the forces and moment are applied. Therefore, the power extracted from the flow field is

$$\Pi = M_P\Omega - F^X q_\infty = \pi\left[2\lambda q_\infty^2 \Omega \sin\Omega t - \pi(1-\lambda)^2\Omega^2 R q_\infty \cos\Omega t\right] \tag{A.16}$$

It is remarkable that for $\lambda = 0$, the ellipse reduces to a unit circle on the physical z-plane. In this case $M_P = 0$ and the forces applied on the shaft become $F^X = \pi\Omega^2 R\cos\Omega t$, $F^Y = \pi\Omega^2 R\sin\Omega t$, which correspond to the forces expressed by the 'added mass' of a circle multiplied by the centrifugal acceleration (see for instance [41]).

By means of the first law of thermodynamics applied to this model, we verified that the mechanical power exerted on the system $-\Pi$ has to be equivalent to the kinetic power of the fluid Π_f^k. Following [41], the kinetic energy of the fluid, when the stream at infinity is at rest, can be expressed by the relation

$$T_f = -\frac{\mathrm{i}}{4}\int_B w\ \mathrm{d}w^*. \tag{A.17}$$

Let us consider the complex potential A.14. By subtracting the contribution of the undisturbed stream $\mathrm{i}q_\infty \mathrm{e}^{\mathrm{i}\Omega t}\zeta$, the complex potential is defined on a moving galileian

frame of reference so that the infinity is at rest. This new complex potential is integrated along the unit circle contour in the equation A.17, that is

$$T_f = -\frac{1}{4}\int_0^{2\pi} w(\phi)\left(\frac{\mathrm{d}w}{\mathrm{d}\zeta}\right)^* \mathrm{e}^{-\mathrm{i}\phi}\mathrm{d}\phi \tag{A.18}$$

Finally the kinetic power of the fluid is given by

$$\Pi_f^k = \frac{\mathrm{d}T_f}{\mathrm{d}t} = \pi\left[-2\lambda q_\infty^2\omega\sin 2\Omega t + (1-\lambda)^2\Omega^2 R q_\infty \cos\Omega t\right], \tag{A.19}$$

that is equivalent to $-\Pi$.

A.2.7 The 'momentum equation' applied to the 2D circular cylinder benchmark

The 'momentum equation' 3.29 is the tool adopted in order to validate the level set vortex method on the 2D flow past the circular cylinder test case. The aim of this validation is to compute the time history of the aerodynamic coefficients C_D and C_L by varying the Reynolds number.

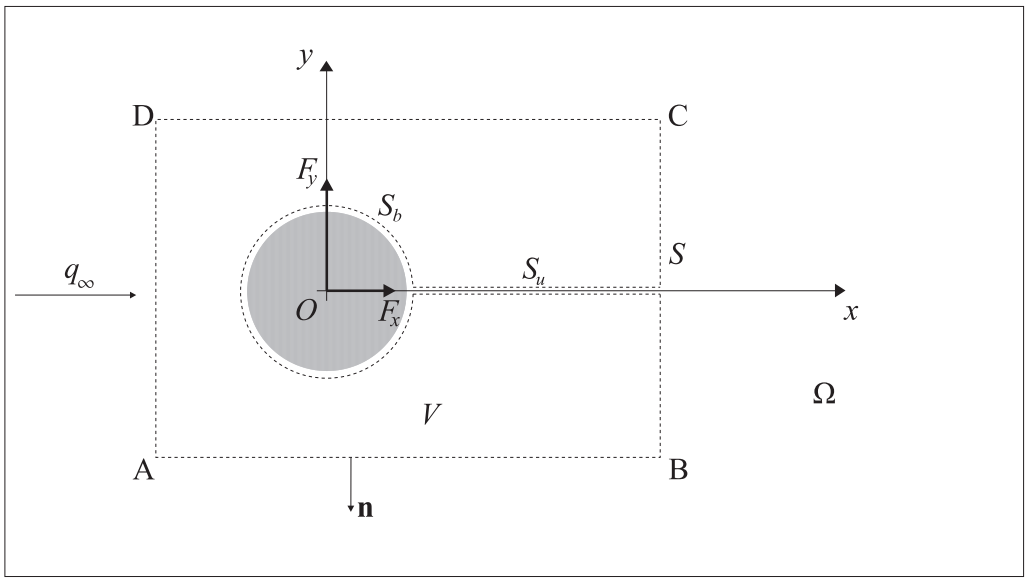

Figure A.11. Computational domain Ω and control volume V. ABCD is the fluid region that is integrated.

The figure A.11 shows the test case setup, the control volume and surfaces considered. Let F_x, F_y and u, v be the Cartesian components of the force **F** and of the

velocity $\mathbf{u}$, respectively. If d is the cylinder diameter and q_∞ is the free stream velocity, we establish d as reference length and q_∞ as reference velocity. The Reynolds number is then determined by $\mathrm{Re} = q_\infty d/\nu$. With this reference quantities and by taking into account the fact that the cylinder does not move and the control volume is fixed, i.e. $\mathbf{u}_S = 0$, $V(t) = V$, $S(t) = S$ and $S_b(t) = S_b$, the 2D non-dimensional 'momentum equation' reads

$$\mathbf{F} = -\frac{\mathrm{d}}{\mathrm{d}t}\int_V \mathbf{u}\ \mathrm{d}V + \oint_S \mathbf{n}\cdot\boldsymbol{\gamma}_{mom}\mathrm{d}S - \oint_{S_b} \mathbf{n}\cdot\mathbf{u}\mathbf{u}\ \mathrm{d}S, \tag{A.20}$$

where

$$\boldsymbol{\gamma}_{mom} = \frac{1}{2}u^2\mathbf{I} - \mathbf{u}\mathbf{u} - \mathbf{u}(\mathbf{x}\wedge\omega\,\boldsymbol{k}) - \left[\left(\mathbf{x}\cdot\frac{\partial\mathbf{u}}{\partial t}\right)\mathbf{I} - \mathbf{x}\frac{\partial\mathbf{u}}{\partial t}\right] + \left[\mathbf{x}\cdot(\nabla\cdot\mathbf{T})\mathbf{I} - \mathbf{x}(\nabla\cdot\mathbf{T}) + \mathbf{T}\right],$$

with

$$\mathbf{T} = \frac{1}{\mathrm{Re}}\left(\nabla\mathbf{u} + \nabla\mathbf{u}^T\right).$$

The non-dimensional force $\mathbf{F}$ scales as $\sim \rho q_\infty^2 d$, thus the aerodynamic coefficients becomes $C_D = 2F_x$ and $C_L = 2F_y$.

Since on the solid wall the no-slip condition is enforced, the line integral along S_b is negligible due to order of accuracy of the scheme, thus the components of the force exerted on the cylinder are

$$\begin{aligned}
F_x = &-\frac{\mathrm{d}}{\mathrm{d}t}\int_{ABCD} u(1-H(\phi))\ \mathrm{d}x\mathrm{d}y + \\
&\int_A^B \left[uv + v\omega y - y\frac{\partial u}{\partial t} + \frac{1}{\mathrm{Re}}\left(2\frac{\partial^2 u}{\partial x^2} + \frac{\partial^2 u}{\partial y^2} + \frac{\partial^2 v}{\partial x\partial y}\right)y - \frac{1}{Re}\left(\frac{\partial u}{\partial y} + \frac{\partial v}{\partial x}\right)\right]\mathrm{d}x + \\
&\int_B^C \left[\frac{1}{2}(v^2-u^2) - u\omega y - y\frac{\partial v}{\partial t} + \frac{1}{\mathrm{Re}}\left(2\frac{\partial^2 v}{\partial y^2} + \frac{\partial^2 v}{\partial x^2} + \frac{\partial^2 u}{\partial x\partial y}\right)y + \frac{2}{Re}\left(\frac{\partial u}{\partial x}\right)\right]\mathrm{d}y + \\
&\int_C^D \left[-uv - v\omega y + y\frac{\partial u}{\partial t} - \frac{1}{\mathrm{Re}}\left(2\frac{\partial^2 u}{\partial x^2} + \frac{\partial^2 u}{\partial y^2} + \frac{\partial^2 v}{\partial x\partial y}\right)y + \frac{1}{Re}\left(\frac{\partial u}{\partial y} + \frac{\partial v}{\partial x}\right)\right]\mathrm{d}x + \\
&\int_D^A \left[-\frac{1}{2}(v^2-u^2) + u\omega y + y\frac{\partial v}{\partial t} - \frac{1}{\mathrm{Re}}\left(2\frac{\partial^2 v}{\partial y^2} + \frac{\partial^2 v}{\partial x^2} + \frac{\partial^2 u}{\partial x\partial y}\right)y - \frac{2}{Re}\left(\frac{\partial u}{\partial x}\right)\right]\mathrm{d}y
\end{aligned}$$

$$
\begin{aligned}
F_y = &- \frac{\mathrm{d}}{\mathrm{d}t} \int_{ABCD} v(1 - H(\phi))\ \mathrm{d}x\mathrm{d}y + \\
&\int_A^B \left[\frac{1}{2}(v^2 - u^2) - v\omega x + x\frac{\partial u}{\partial t} - \frac{1}{\mathrm{Re}} \left(2\frac{\partial^2 u}{\partial x^2} + \frac{\partial^2 u}{\partial y^2} + \frac{\partial^2 v}{\partial x \partial y} \right) x - \frac{2}{Re} \left(\frac{\partial v}{\partial y} \right) \right] \mathrm{d}x + \\
&\int_B^C \left[-uv + u\omega x + x\frac{\partial v}{\partial t} - \frac{1}{\mathrm{Re}} \left(2\frac{\partial^2 v}{\partial y^2} + \frac{\partial^2 v}{\partial x^2} + \frac{\partial^2 u}{\partial x \partial y} \right) x + \frac{1}{Re} \left(\frac{\partial v}{\partial x} + \frac{\partial u}{\partial y} \right) \right] \mathrm{d}y + \\
&\int_C^D \left[-\frac{1}{2}(v^2 - u^2) + v\omega x - x\frac{\partial u}{\partial t} + \frac{1}{\mathrm{Re}} \left(2\frac{\partial^2 u}{\partial x^2} + \frac{\partial^2 u}{\partial y^2} + \frac{\partial^2 v}{\partial x \partial y} \right) x + \frac{2}{Re} \left(\frac{\partial v}{\partial y} \right) \right] \mathrm{d}x + \\
&\int_D^A \left[uv - u\omega x - x\frac{\partial v}{\partial t} + \frac{1}{\mathrm{Re}} \left(2\frac{\partial^2 v}{\partial y^2} + \frac{\partial^2 v}{\partial x^2} + \frac{\partial^2 u}{\partial x \partial y} \right) x - \frac{1}{Re} \left(\frac{\partial v}{\partial x} + \frac{\partial u}{\partial y} \right) \right] \mathrm{d}y
\end{aligned}
$$

Bibliography

[1] VortexCell2050 - Fundamentals of actively controlled flows with trapped vortices. `http://www.vortexcell2050.org`.

[2] J. C. Adams. Mudpack: Multigrid Software for Elliptic Partial Differential Equations. `http://www.cisl.ucar.edu/css/software/mudpack/`.

[3] J. C. Adams, P. Swartztrauber, and R. Sweet. Fishpack90 - fortran library. `http://www.cisl.ucar.edu/css/software/fishpack90/`.

[4] P. Angot, C. H. Bruneau, and P. Fabrie. A penalization method to take into account obstacles in incompressible viscous flows. *Numer. Math.*, 81:497–520, 1999.

[5] A. Armando. Flusso alla Prandtl-Batchelor su corpo tozzo in un canale. Master's thesis, Dissert. Tesi di Laurea Ing. Aerosp., Politecnico di Torino, Turin, Italy, 2005.

[6] G. K. Batchelor. On steady laminar flow with closed streamlines at large Reynolds number. *J. Fluid Mech.*, 1:177–190, 1956.

[7] G. K. Batchelor. A proposal concerning laminar wakes behind bluff bodies at large Reynolds number. *J. Fluid Mech.*, 1(1):388–398, 1956.

[8] C. E. Brown and W. H. Michael. Effect of leading-edge separation on the lift of a delta wing. *J. Aero. Sci.*, 21:690–694, 1954.

[9] C. H. Bruneau and I. Mortazavi. Passive control of the flow around a square cylinder using porous media. *Int. J. Num. Fluids*, 46:415–433, 2004.

[10] I. P. Castro. Weakly stratified laminar flow past normal flat plates. *J. Fluid Mech.*, 454:21–46, 2002.

[11] S. I. Chernyshenko. Stratified Sadovskii flow in a channel. *J. Fluid Mech.*, 250:423–431, 1993.

[12] S. I. Chernyshenko and I. P. Castro. High-Reynolds-number asymptotics of the steady flow through row of bluff bodies. *J. Fluid Mech.*, 257:421–449, 1993.

[13] R. R. Clements. An inviscid model of two-dimensional vortex shedding. *J. Fluid Mech.*, 57(2):321–336, 1973.

[14] M. Coquerelle, J. Allard, G. H. Cottet, and M. P. Cani. A Vortex Method for Bi-phasic Fluids Interacting with Rigid Bodies. *Arxiv preprint math, LMC-IMAG*, page na/0607597, 2006.

[15] M. Coquerelle and G. H. Cottet. A vortex level set method for the two-way coupling of an incompressible fluid with colliding rigid bodies. *J. Comput. Phys.*, 227:9121–9137, 2008.

[16] L. Cortelezzi. Nonlinear feedback control of the wake past a plate with suction point on the downstream wall. *J. Fluid Mech.*, 327:303–324, 1996.

[17] G. H. Cottet and P. D. Koumoutsakos. *Vortex Methods - Theory and Practice*. Cambridge University Press, 2000.

[18] G. H. Cottet and L. Weynans. Particle methods revisited: a class of high-order finite-difference schemes. *C. R. Acad. Sci. Paris*, 343:51–56, 2006.

[19] D. Crowdy and J. Marshall. Growing vortex patches. *Phys. Fluids*, 16:3122–3129, 2004.

[20] D. G. Crowdy and J. S. Marshall. The motion of a point vortex around multiple circular islands. *Phys. Fluids*, 17:56602–56613, 2005.

[21] G. S. Deem and N. J. Zabusky. Vortex Waves: Stationary 'V-states', Interactions, Recurrence and Breaking. *Phys. Rev. Lett.*, 40(1):859–862, 1978.

[22] A. R. Elcrat, B. Fornberg, M. Horn, and K. Miller. Some steady vortex flows past a circular cylinder. *J. Fluid Mech.*, 409:13–27, 2000.

[23] C. Ferrari. Sulla trasformazione conforme di due cerchi in due profili alari. *Mem. R. Acc. Sci. Torino*, 68:1–15, 1930.

[24] L. Föppl. Wirbebewegung hinter einem kreiszylinder. *Sitzb. d. k. Baeyr., Akad. d. Wiss., Math-Physi. Klasse, München*, 1(1):1–17, 1913.

[25] B. Fornberg. Steady incompressible flow past a row of circular cylinders. *J. Fluid Mech.*, 225:655–671, 1991.

[26] F. Gallizio. Modello di Prandtl-Batchelor per il flusso normale ad una placca piana posta all'interno di un canale: studio numerico dell'esistenza e unicitá della soluzione. Master's thesis, Dissert. Tesi di Laurea Ing. Aerosp., Politecnico di Torino, Turin, Italy, 2004.

[27] F. Gallizio, B. Galletti, A. Iollo, and L. Zannetti. Inviscid detached channel flows past wall-mounted plates. Fourth conference on Bluff Body Wakes and Vortex-Induced-Vibrations, Santorini, Greece, 2005.

[28] F. Gallizio, A. Iollo, B. Protas, and L. Zannetti. On continuation of inviscid vortex patches. *Physica D - (under review)*, 2009.

[29] F. Gallizio, L. Zannetti, and A. Iollo. Prandtl-Batchelor channel flows past plates at normal incidence. The Sixth Euromech Fluid Mechanics Conference, Stockholm, Sweden, 2006.

[30] L. Gasinski and N. S. Papageorgiou. *Nonlinear Analysis*. Chapman & Hall, 2006.

[31] G. Graziani and P. Bassanini. Unsteady viscous flows about bodies: vorticity release and forces. *Meccanica*, 37:283–303, 2002.

[32] M. S. Howe. Emendation of the Brown & Michael equation, with application to

sound generation by vortex motion near a half-plane. *J. Fluid Mech.*, 329:89–101, 1996.

[33] D. C. Ives. A modern look at conformal mapping, including multiply connected regions. *AIAA J.*, 14:1006–1011, 1976.

[34] E. R. Johnson and N. R. McDonald. The motion of a vortex near two circular cylinders. *Proc. R. Soc. Lond A*, 460:939–954, 2004.

[35] E. R. Johnson and N. R. McDonald. Vortices near barriers with multiple gaps. *J. Fluid Mech.*, 531:335–358, 2005.

[36] M. Kiya and M. Arie. A contribution to an inviscid vortex-shedding model for an inclined flat plate in uniform flow. *J. Fluid Mech.*, 82(2):223–240, 1977.

[37] P. Koumoustakos and A. Leonard. High-resolution simulations of the flow around an impulsively started cylinder using vortex methods. *J. Fluid Mech.*, 296:1–38, 1995.

[38] K. Kuwahara. Numerical study of flow past an inclined flat plate by an inviscid model. *J. Phys. Soc. Japan*, 35:1545–1551, 1973.

[39] B. Lucquin and O. Pironneau. *Introduction au calcul scientifique*. Masson, 1996.

[40] A. Masotti. Sulla funzione preliminare di Green per un'area piana. In *Atti del seminario matematico e fisico di Milano*, volume 6, pages 3–53, 1932.

[41] L. M. Milne-Thomson. *Theoretical Hydrodynamics*. Dover 1996, 1968.

[42] R. Mittal and G. Iaccarino. Immersed boundary methods. *Annu. Rev. Fluid. Mech.*, 37:239–261, 2005.

[43] G. Moretti. *Function of Complex Variable*. Prentice-Hall, Englewood Cliffs, N.J., 1964.

[44] I. Mortazavi. *Methode Hybride Vortex-Elements Finis: Etude de la Convergence Numerique, Caracterisation et Analyse d'un Ecoulement Complexe*. PhD thesis, University of Lille 1, 1997.

[45] I. Mortazavi and A. Giovannini. The simulation of vortex dynamics downstream of a plate separator using a vortex-finite element method. *Int. J. Fluid Dyn.*, 5:31–48, 2001.

[46] F. Noca, D. Shiels, and D. Jeon. A comparison of methods for evaluating time-dependent fluid dynamic forces on bodies, using only velocity fields and their derivatives. *J. Fluids Struct.*, 13:551–578, 1999.

[47] S. Osher and R. Fedkiw. *Level Set Methods and Dynamic Implicit Surfaces*. Springer, 2003.

[48] G. M. Ottino. *Two approaches to the Study of Detached Flows*. PhD thesis, DIASP, Politecnico di Torino - IMB, Université de Bordeaux 1, 2009.

[49] L. S. Pan and Y. T. Chew. A general formula for calculating forces on a 2-d arbitrary body in incompressible flow. *J. Fluids Struct.*, 16(1):71–82, 2002.

[50] M. C. A. M. Peters. *Aeroacoustic sources in internal flows*. PhD thesis, Technische Universiteit Eindhoven, 1993.

[51] R. T. Pierrehumbert. A family of steady, translating vortex pairs with distributed vorticity. *J. Fluid Mech.*, 99:129–144, 1980.

[52] O. Pironneau and F. Hecht. FreeFem++. `http://www.freefem.org`.

[53] P. Ploumhans and G. S. Winckelmans. Vortex methods for high-resolution simulations of viscous flow past bluff bodies of general geometry. *J. Comput. Phys.*, 165:354–406, 2000.

[54] B. Protas. Vortex dynamics models in flow control problems. *Nonlinearity*, 21:203–250, 2008. doi: 10.1088/0951-7715/21/9/R01.

[55] P. Protas. On an attempt to simplify the Quartapelle-Napolitano approach to computation of hydrodynamic forces in open flows. *J. Fluids Struct.*, 23:1207–1214, 2007.

[56] L. Quartapelle and M. Napolitano. Force and moment in incompressible flows. *AIAA J.*, 21:911–913, 1982.

[57] A. Quarteroni and A. Valli. *Domain decomposition methods for partial differential equations*. Oxford University Press, 1999.

[58] F. O. Ringleb. *Boundary Layer and Flow Control*, chapter Separation control by trapped vortices. Pergamon Press, 1961.

[59] D. Russell and Z. J. Wang. A cartesian grid method for modeling multiple moving objects in 2D incompressible viscous flow. *J. Comput. Phys.*, 191:177–205, 2003.

[60] Y. Saad. *Iterative Methods for Sparse Linear Systems, Second Edition*. SIAM, 2003.

[61] V. S. Sadovskii. Vortex regions in a potential stream with a jump of Bernoulli's constant at the boundary. *Appl. Math. Mech.*, 325:729–735, 1971.

[62] P. G. Saffman. *Vortex Dynamics*. Cambridge University Press, 1992.

[63] P. G. Saffman and R. Szeto. Equilibrium shapes of a pair of equal uniform vortices. *Phys. Fluids*, 23(12):2339–2342, 1980.

[64] P. G. Saffman and S. Tanveer. Prandtl-Batchelor flow past a flat plate with a forward-facing flap. *J. Fluid Mech.*, 143:351–365, 1984.

[65] T. Sarpkaya. An inviscid model of two-dimensional vortex shedding for transient and asymptotically steady separated flow over an inclined plate. *J. Fluid Mech.*, 68:109–128, 1975.

[66] J. A. Sethian. *Level Set Methods and Fast Marching Methods: Evolving Interfaces in Computational Geometry, Fluid mechanics, Computer Vision, and Material Science*. Cambridge University Press, 1996.

[67] J. H. B. Smith and R. W. Clark. Non existence of stationary vortices behind a two-dimensional normal plate. *AIAA J.*, 13(8):1114–1115, 1986.

[68] L. Sowerby. *Vector field theory with applications*. Longman, 1974.

[69] M. Tabor. *Chaos and integrability in nonlinear dynamics: an introduction*. New York - Wiley, 1989.

[70] F. Tricomi. *Funzioni Ellittiche*. Zanichelli, Bologna, 1951.

[71] C. Turfus. Prandtl-Batchelor flow past a flat plate at normal incidence in a channel - inviscid analysis. *J. Fluid Mech.*, 249:59–72, 1993.

[72] C. Turfus and I. P. Castro. A Prandtl-Batchelor model of flow in the wake of a cascade of normal flat plates. *Fluid Dyn. Res.*, 26(3):181–202, 2000.

[73] M. van Dyke. *An album of fluid motion.* Stanford: The Parabolic Press, 1982.

[74] Von Karman institute for fluid dynamics - lecture series. *Wind turbine aerodynamics: a state-of-the-art*, 2007.

[75] J. C. Wells. Calculating the impulse and angular impulse of image vorticity by integrals over free vorticity. *Proc. R. Soc. Lond. A*, 454:2791–2809, 1998.

[76] C. H. K. Williamson. Vortex dynamics in the cylinder wake. *Annu. Rev. Fluid. Mech.*, 28:477–539, 1996.

[77] L. Zannetti. Vortex equilibrium in the flow past bluff bodies. *J. Fluid Mech.*, 562:151–171, 2006.

[78] L. Zannetti and S. Chernyshenko. Vortex pair and chaplygin cusps. *Eur. J. Mech. B/Fluids*, 24:328–337, 2005.

[79] L. Zannetti and P. Franzese. The non-integrability of the restricted problem of two vortices in closed domains. *Physica D*, 76:99–109, 1994.

[80] L. Zannetti, F. Gallizio, and A. Iollo. About finite area wakes past bluff bodies and growing vortex patches. IUTAM symposium - 150 Years of Vortex Dynamics, Lyngby - Copenhagen, Denmark, 2008.

[81] L. Zannetti, F. Gallizio, and G. M. Ottino. Vortex capturing vertical axis wind turbine. *J. of Physics: Conference Series*, 75:1–10, 2007. doi:10.1088/1742-6596/75/1/012029.

[82] L. Zannetti, F. Gallizio, and G. M. Ottino. Vortex motion in doubly connected domains. *J. Fluid Mech.*, 612:143–152, 2008.

[83] L. Zannetti and A. Iollo. Passive control of the vortex wake past a flat plate at incidence. *Theoretical Comput. Fluid Dyn.*, 16:211–230, 1986.